Inaugural Dissertation zur Erlangung des Doktorgrades der
Naturwissenschaften im Fachbereich Mathematik und Informatik,
Physik, Geographie der Justus-Liebig-Universität Gießen

Nanoparticle Friction and Contact Ageing

vorgelegt von

Michael Feldmann

Betreuer

Prof. Dr. André Schirmeisen

Institut für Angewandte Physik
Justus-Liebig-Universität Gießen

Oktober 2013

For my parents

Abstract

The phenomenon of friction permeates the vast majority of mechanical systems, but despite its ubiquity, the basic mechanisms leading to friction are currently not very well understood. Instead, the characterization of friction is mostly limited to phenomenological descriptions.

A promising way to improve on the comprehension of friction on a fundamental level is guided by the fact that macroscopic contacts in general can be broken down into many smaller sub-contacts. It thus is imperative to investigate friction of these smallest units, the so-called single asperity nanoscale contacts, to gain insight into the basic principles governing friction. An essential issue in this context is the emergence of contact ageing, which i.a. is the cause for static friction. Contact ageing is observed in macroscopic friction experiments on a regular basis, but its existence in nanoscale contacts could only recently be demonstrated for the first time.

Nanoparticles manipulated under vacuum conditions using friction force microscopes represent an excellent experimental model system in this endeavor to study frictional properties of single asperity contacts. In this work, experimental methods to manipulate nanoparticles and to study their frictional characteristics were developed and implemented. This framework allowed to conduct fundamental experiments regarding the friction kinetics of antimony nanoparticles on graphite substrates with respect to their velocity- and temperature-dependence.

By carrying out Monte Carlo simulations of a newly devised nanoscale friction model, two competing processes were identified as having a major impact on the friction kinetics, namely thermal activation as well as ageing of the contacts. The observation of stick-slip-type friction in consecutive experiments allowed to directly quantify contact ageing in nanoparticle friction, exposing an ageing law with logarithmic dependence on stationary hold times.

Complementary measurements revealed two qualitatively different contact ageing phenomena for point-like contacts at varied temperatures. In silica-gold contacts, ageing during lateral movement due to gold neck shearing could be registered, while silica-silica contacts exhibited ageing of stationary contacts, comparable to the contact ageing found for antimony nanoparticles.

All findings highlight the fundamental significance of contact ageing in nanoscale friction, especially for the case of nanoparticle kinetics.

Contents

List of Abbreviations

Notation	Description
AFM	atomic force microscope
CT	contact [mode of AFM operation]
DSM	dynamic surface modification [mode]
FFM	friction force microscope
HOPG	highly orientated pyrolytic graphite
MD	molecular dynamics [simulation]
MEMS	micro electro-mechanical system
MK	mechano-kinetic [model]
NC	non-contact [mode of AFM operation]
NP	nanoparticle
PID	proportional-integral-derivative [controller]
PLL	phase-locked loop
PSD	position-sensitive detector
PT	Prandtl-Tomlinson [model]
RT	room temperature
Sb	[chemical element] antimony
SEM	scanning electron microscope
SFA	surface force apparatus
SHS	slide-hold-slide [experiment]
SPM	scanning probe microscopy
STM	scanning tunneling microscope
TA-CA	thermally activated contact ageing [model]
TA-PT	thermally activated Prandtl-Tomlinson [model]
TOS	tip-on-side [manipulation mode]
TOT	tip-on-top [manipulation mode]
UHV	ultra high vacuum
VT	variable temperature

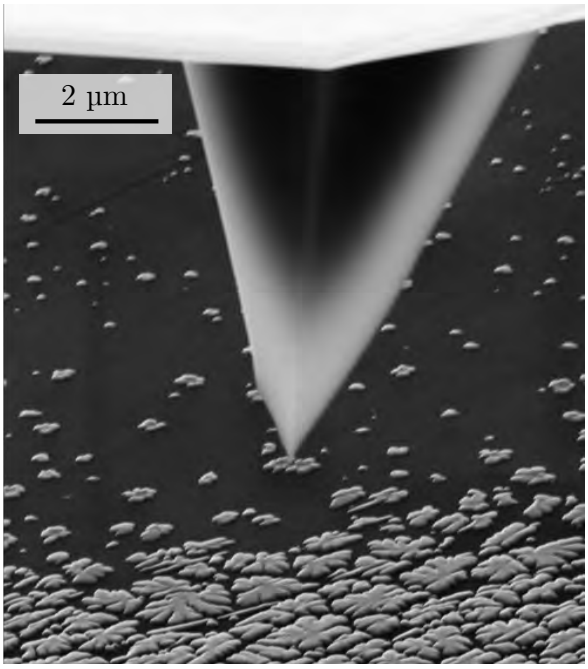

Figure 0.1: AFM tip in front of a graphite sample covered with antimony nanoparticles. Imaged using an SEM.

It is quite difficult to do accurate quantitative experiments in friction, and the laws of friction are still not analyzed very well, in spite of the enormous engineering value of an accurate analysis. Although the law $F = \mu N$ is fairly accurate once the surfaces are standardized, the reason for this form of the law is not really understood. [...] At any rate, this friction law is another of those semiempirical laws that are not thoroughly understood, and in view of all the work that has been done it is surprising that more understanding of this phenomenon has not come about.

—Richard P. Feynman (1971)

1 Introduction

Friction is a phenomenon which pervades everyday life. For a broad variety of physical systems and technological achievements, friction is of fundamental importance, spanning diverse topics such as the operation of car engines and tyres or the workings of human joints and muscles.

Considering the impact of friction, the insight into the origins of friction is comparatively sparse. Although the field of research regarding friction, called *tribology*, was established centuries ago by early scientists such as Leonardo da Vinci (1459–1519) (Dowson, 1997), the obtained knowledge was for a long time limited to approximative, phenomenological descriptions. This was due to the fact that macroscopic interfaces consist of many individual nanoscale junctions, and thus only averages over these junctions can be observed macroscopically. The invention of the friction force microscope (FFM) by Mate et al. (1987) marked the advent of true nanoscale friction experiments at single interface junctions. Since then, the field of nanotribological research has emerged, which aims to explain the foundations of friction with respect to contacts of atomic length scales.

One central problem in nanoscale friction experimentation is to obtain well-defined interfaces, since friction in general is very sensitive to changes in interface composition and geometry. Because contamination and wear can rapidly alter these conditions, the use of sample systems specifically crafted for this task becomes imperative. In this work the use of nanoparticles as a very well-suited model system in tribological experimentation is explored. In particular, frictional properties of antimony particles prepared onto highly orientated pyrolytic graphite (HOPG) substrates were probed. All experiments were carried out under ultra high vacuum (UHV) conditions to minimize interface contamination. Since nanoparticle (NP) manipulation for friction measurement constitutes a very novel technique, manipulation protocols and implementations had to be developed in order to allow for highly controlled and reproducible manipulation experiments.

Many contacts exhibit a phenomenon called *contact ageing*: the force needed to initiate relative motion depends on the length of time during which the interfaces were kept in stationary contact. For long hold times this effect leads

to the emergence of *static friction*, which is usually larger than the *kinetic friction* of interfaces in relative motion. While macroscopic contact ageing was first described by Charles-Augustin de Coulomb (1736–1806) hundreds of years ago (Dowson, 1997), the existence of contact ageing for nanoscale systems could only recently be demonstrated (Li et al., 2011). In this work, experiments regarding contact ageing of nanoparticles are presented, which expose the significance of contact ageing in the sliding dynamics of nanoparticles.

Another very important factor in friction experimentation is the size of the contact area. The contact size in conventional FFM experiments is usually not very well defined. But by using nanoparticles for friction experimentation the investigation of the contact area dependence of nanoscale friction becomes feasible; contact area ranges unaccessible by conventional FFM measurements can be probed, and the scaling of friction with contact area can be investigated, which carries information regarding the composition of the sliding interface.

Two parameters of significant influence on sliding friction are the temperature and the relative velocity of the sliding contact. In previous works, the influence of these parameters on friction was examined for direct FFM tip-sample contacts (Schirmeisen et al., 2006; Barel et al., 2011). While a rich interdependence was observed, the interface temperature was not very well-defined due to the construction of the utilized FFM. In experiments using NPs, the interface temperature is much more well-defined due to the enhanced thermal coupling between particle and substrate at increased contact areas. The measured velocity- and temperature-dependence of NP friction are compared to simulations of a newly devised friction model which incorporates contact ageing effects.

Additional experiments were conducted to probe the temperature dependence of stationary contact ageing in point-like silica-on-silica contacts. A fundamentally different form of *kinetic* contact ageing could be demonstrated in further experiments using gold surfaces, which originates from plastic deformation of nanoscale junctions and thermally activated regeneration of gold-silica interfaces.

The remaining body of this work is organized as follows: Chapter 2 provides an overview of the relevant nanotribological models and concepts. In Chapter 3 the working principle of the atomic force microscope (AFM) is presented, including it's application to nanotribological issues. Calibration procedures necessary to arrive at quantitative results are discussed. Chapter 4 lays out in detail the employed NP manipulation framework and introduces the experimental model system of antimony NPs on graphite. Experimental findings using NP manipulation and accompanying Monte Carlo simulations

are presented in Chapter 5. In Chapter 6 contact ageing results regarding direct AFM tip-sample contacts are shown. Finally, Chapter 7 provides a summary of the central findings presented in this work.

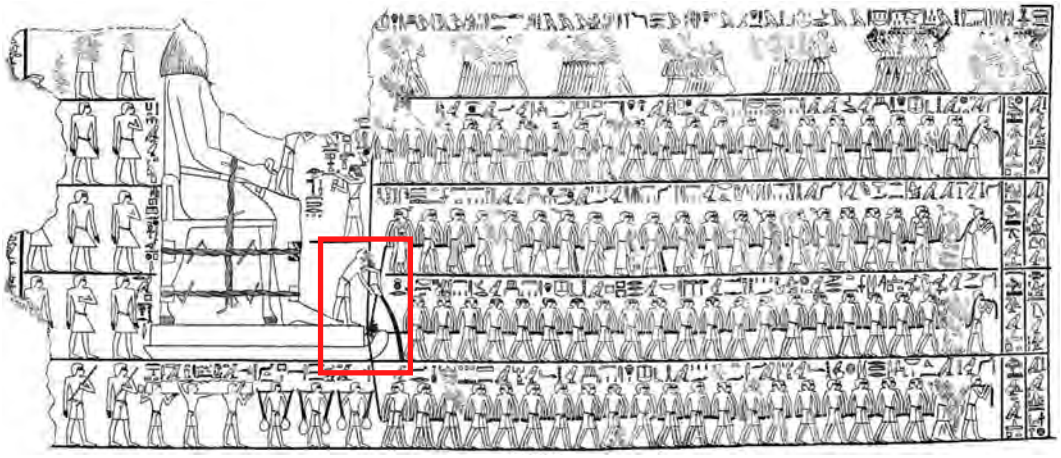

Figure 2.1: Egyptian workers dragging a sled with a colossus, dated from ∼1880 B.C. (Dowson, 1997). One Egyptian is depicted as pouring lubricant on the ground in front of the sled (red rectangle). Photograph of a painting at the tomb of Tehuti-Hetep, El-Bershed, one of the earliest testimonials of friction engineering. Image from (Newberry et al., 1894).

2 Nanotribology: Concepts and Models

Tribology is 'the science and technology of interacting surfaces in relative motion' (Persson, 1998). The term *tribology*, as coined by one of the pioneers of this field, David Tabor (Field, 2008), originates from the Greek verb $\tau\rho\iota\beta\omega\sigma$, which can be translated as *rubbing* (Persson, 1998). The most prominent phenomenon in the area of tribological research is the occurrence of friction, which can be characterized as a force resisting the relative lateral motion of two contacting bodies. Other topics of interest in tribology include the evaluation of lubricants and investigation of wear effects.

Friction has been subjected to studies for a very long time, appropriate to the overall impact of the phenomenon. First considerations of frictional processes are documented in the form of hieroglyph paintings concerning the

construction of Egyptian pyramids nearly four millennia ago, as depicted in Fig. 2.1. Systematic studies of friction conducted many centuries ago are documented in the literature (Dowson, 1997). The discoveries of three phenomenological friction laws have been of particular historic importance (Persson, 1998):

1. Friction is proportional to the applied normal load.
2. Friction does not depend on the apparent contact area.
3. Kinetic friction does not depend on the relative velocity.

The first law was discovered by Leonardo da Vinci (1452–1519), and later, independently, by Guillaume Amontons (1699). It is known today as *Amontons' Law*, while the second and third law are attributed to Charles-Augustin de Coulomb (1785). Frictional processes obeying these three laws can be characterized by the proportionality factor μ between normal load F_N and friction force F_F:

$$F_F = \mu \cdot F_N \tag{2.1}$$

The parameter μ herein is named *coefficient of friction* and is specific to the materials and geometries of the particular sliding bodies. It has to be noted that the original formulation of Amontons did not contain the notion of a friction *force*, since the concept of forces was only introduced 200 years later by Isaac Newton (Persson, 1998). These three classical friction laws and Eq. (2.1) hold for a range of macroscopic contact geometries and material combinations and have proven their validity for numerous engineering problems, but they do not explain the origin of frictional processes.

The aim of research into friction changed from a purely phenomenological description towards investigations of its fundamental processes, when Bowden and Tabor developed the idea that each macroscopic contact is made up of a multitude of microscopic contacts, so-called asperities. Bowden described the contact of macroscopic bodies 'like turning Switzerland upside down and standing it on Austria—the area of intimate contact will be rather small'. (Field, 2008)

The notion of a hierarchical structure in macroscopic contacts, with a much smaller *real* contact area than what is apparent on macroscopic scales, is depicted in Fig. 2.2. Even seemingly flat interfaces usually consist of many single asperity junctions, which in turn, at the smallest length scales, may consist of single atomic bonds (Mo et al., 2009). For many contacts found in nature, such as surfaces generated by fracture, or biological surfaces such

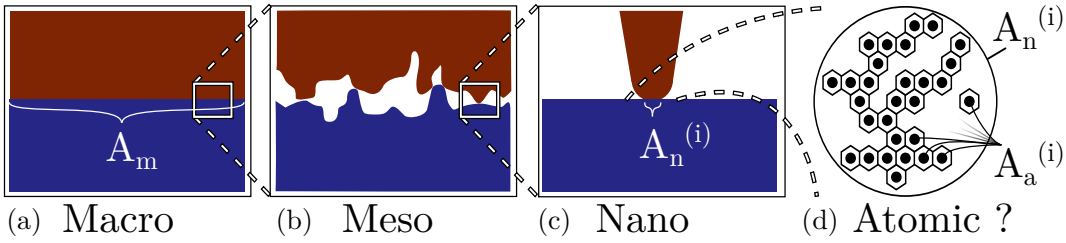

Figure 2.2: Illustration of surface roughness at different length scales. (a) Macroscopically smooth interfaces with an apparent contact area A_m. (b) Macroscopic interfaces actually consist of many nanoscopic sub-contacts i=1...M, called (c) single asperities. The nanoscopic contact area A_n is made up of the real contact areas of the individual single asperities: $A_n = \Sigma_{i=1}^{M} A_n^{(i)}$ with $A_n \ll A_m$. (d) The single asperity contacts can consist of individual atomic bonds, of which only a fraction may be bound at an instant in time (Mo et al., 2009). With each of the N bound atoms (black circles) representing a contact of size A_0 (hexagons), the atomic contact area of the i-th asperity becomes $A_a^{(i)} = N \cdot A_0$, and generally $A_a^{(i)} < A_n^{(i)}$. Adatoms in the interface can lead to similar configurations. For atomic-scale contacts a thorough definition of what the term 'real contact area' actually means is intricate, especially for van-der-Waals interfaces without individual chemical bonds.

as gecko feet, this breakdown of larger contacts into sub-contacts is repeated on many length scales. These types of contacts are well-described as 'fractal surfaces' (Persson et al., 2003).

From this insight into the hierarchical structure of contacts a new approach to study the fundamentals of friction was conceived: scientists have turned towards the analysis of contacts consisting of only very few asperities, or even of just a single asperity. Averaging effects over many asperities are considerably reduced in these simpler systems, to the means of allowing to observe the basic principles governing friction. The field of research concerned with these nanoscale physical systems and their tribological characteristics is aptly named *nanotribology*. Even initial measurements of the force needed to move just a single molecule (Langewisch et al., 2013) or atom (Ternes et al., 2008) now have been performed.

First successful experiments regarding friction on microscopic length scales were enabled by the invention of the surface force apparatus (SFA) (Israelachvili et al., 1973). A series of further leaps in surface characterization instrumentation led to the invention of the friction force microscope (FFM) by Mate et al. (1987), which has facilitated the systematic study of true single asperity nanoscale friction. The associated experimental techniques will be discussed in detail in

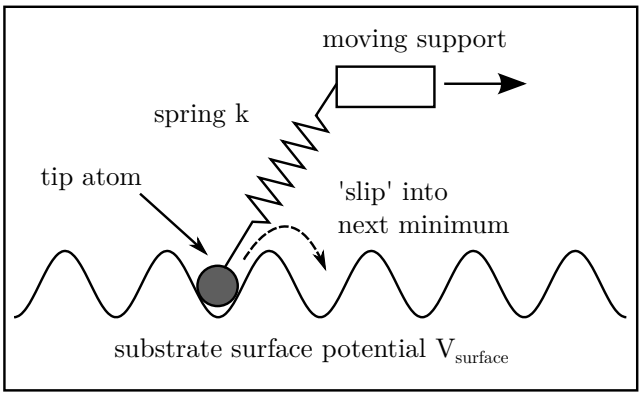

Figure 2.3: Prandtl-Tomlinson model. A tip is dragged over a surface with a periodic surface potential corrugation, and is connected to a moving support with a spring. The tip is stuck in a local minimum until the spring force increases sufficiently to induce a jump to the next potential energy minimum.

Chapter 3.

In the remainder of this chapter a number of nanoscale friction phenomena relevant to this work, as well as associated friction models, will be introduced. The Prandtl-Tomlinson (PT) model conveys an understanding of basic kinetics in atomic-scale friction, while the thermally activated Prandtl-Tomlinson (TA-PT) model together with the mechano-kinetic (MK) model yields insights into the velocity- and temperature-dependence of friction. Contact area dependence and contact ageing are of fundamental significance for friction in general, and have been studied in this work for the case of nanoscale contacts. Finally, the motivation for using nanoparticles as an experimental model system in nanotribology and the numerous advantages over simple FFM tip-sample contact experimentation are laid out.

2.1 Prandtl-Tomlinson Model

The Prandtl-Tomlinson (PT) model defines a simplified single asperity contact, in which friction can arise. It was introduced by Ludwig Prandtl (1928) (and, contrary to its name and widespread belief, not by Tomlinson (Popov et al., 2012; Tomlinson, 1929); however, the name was kept for historical reasons).

The mathematical description of the PT model (cf. Fig. 2.3) consists of a sinusoidal periodic surface potential V_{surface} with the corrugation amplitude V_0 and a tip at position x. The tip is connected by a spring with the elastic

potential V_{spring} to a support, which moves with the relative velocity v, and which in turn drags the tip across the periodic surface potential (Socoliuc et al., 2004). A combined PT model potential V_{PT} is obtained according to

$$V_{\text{PT}} = V_{\text{surface}} + V_{\text{spring}} \tag{2.2}$$

$$= \frac{V_0}{2}\sin(2\pi x/a) + \frac{1}{2}k(x - vt)^2. \tag{2.3}$$

The corresponding equation of motion can be given as

$$M\ddot{x} = -\eta\dot{x} - \frac{\partial V_{\text{PT}}}{\partial x} \tag{2.4}$$

$$= -\eta\dot{x} - \frac{V_0\pi}{a}\cos(2\pi x/a) - k(x - vt) \tag{2.5}$$

where M is the tip mass and η is the viscous damping constant. While the tip is located for most of the time in one of the local potential minima, for finite v every minima disappears eventually. The position x^* of the tip at which the local minimum vanishes is determined by the equation

$$\frac{\partial^2}{\partial x^2}V_{\text{PT}} = 0. \tag{2.6}$$

with the solution (Gnecco et al., 2001)

$$x^* = \frac{a}{2\pi}\arccos\left(-\frac{1}{\xi}\right) \tag{2.7}$$

where the parameter

$$\xi = \frac{2\pi^2 V_0}{ka^2}. \tag{2.8}$$

depends on the ratio of surface potential corrugation and spring stiffness.

For $\xi < 1$ the tip follows a continuous trajectory, since, in this case, only one local minimum exists at all times. For $\xi > 1$ multiple minima can coexist. Accordingly, the tip then performs a discontinuous *stick-slip* motion of alternating between being stuck in a local minimum, and, when the current minimum vanishes, jumping to the next minimum. A visualization of the tip dynamics exposed in the stick-slip effect is presented in Fig. 2.4. This discontinuous stick-slip process gives rise to the dissipative nature of friction in this model: Energy is dissipated due to the viscous damping term during the high-velocity slip phase. The phenomenon of stick-slip motion in friction, which

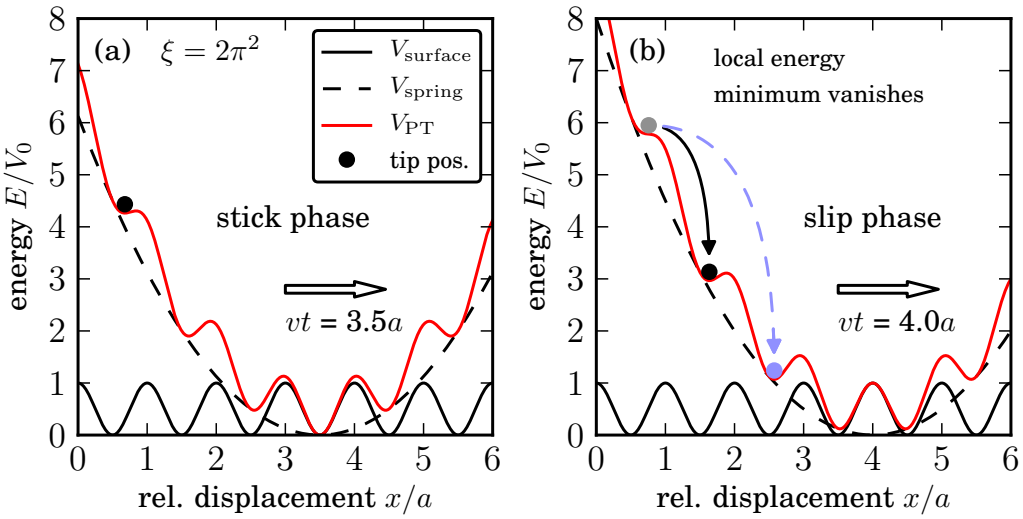

Figure 2.4: Stick-Slip in the Prandtl-Tomlinson (PT) model. (a) The tip (black circle) is trapped in a local energy maximum of the combined potential V_{PT} during the *stick* phase. (b) As the support moves forward the current state eventually becomes unstable, because its local energy minimum vanishes. The tip then jumps to the adjacent energy minimum during the *slip* phase. Depending on the damping strength, jumps across multiple minima are possible (blue marker).

was first described by Bowden et al. (1938), occurs across many length scales, governing the dynamics of phenomena as diverse as atomic friction, violin play, or earthquakes (Mate et al., 1987; Scholz, 1998).

It has to be noted that jumps over multiple minima can also be possible, depending on ξ and η, and have been observed in experiment (Roth et al., 2010).

In the PT model concept, the channels for energy dissipation are not explicitly specified, and simply modeled as viscous dashpot-like dissipation. Plausible candidates for the actual physical energy loss of the system are phononic and electronic dissipation channels (Persson, 1998).

2.2 Thermally Activated PT Model

The simple PT model considers only basic mechanical properties and does not account for thermal effects. An extension of the PT model was introduced by Gnecco et al. (2000); Sang et al. (2001) in order to describe friction for

finite temperatures with $T > 0$: In the so-called thermally activated Prandtl-Tomlinson (TA-PT) model, the tip is exposed to thermal activation in the form of an elevated energy state. The temporal evolution of the probability $p(t)$ for the tip to stay in its current minimum at time t is then determined by a master equation based on fundamental reaction rate theory (Gnecco et al., 2000)

$$\frac{\mathrm{d}p(t)}{\mathrm{d}t} = -f_0 \exp\left(-\frac{\Delta E_{\mathrm{off}}(t)}{\mathrm{k_B}T}\right) p(t), \tag{2.9}$$

in which f_0 is the attempt frequency of the system, and $\Delta E_{\mathrm{off}}(t)$ represents the jump-prohibiting energy barrier at time t. This ansatz can be solved by substituting the dependence on t by a lateral force dependence, assuming a linear reduction of ΔE_{off} with F_L, and evaluating the condition for maximum jump probability. It leads to an increase of the lateral force F_L with the logarithm of the velocity v, for constant, finite temperatures T, as given in

$$F_L = F_{L,0} + A \cdot T \cdot \ln\left(\frac{v}{v_0}\right). \tag{2.10}$$

The model parameters $F_{L,0}$, A and v_0 are constant in v and T in first approximation. More involved calculations using a nonlinear dependence of ΔE_{off} on F_L arrive at very similar, though slightly more complex formulations (Sang et al., 2001). This solution for the TA-PT model is valid for small velocities of $v < v_0$, and thus predicts a decrease of the lateral force with increasing temperature for constant velocities. A detailed overview of reaction rate theory and Arrhenius-type thermal activation can be found in (Pollak et al., 2005).

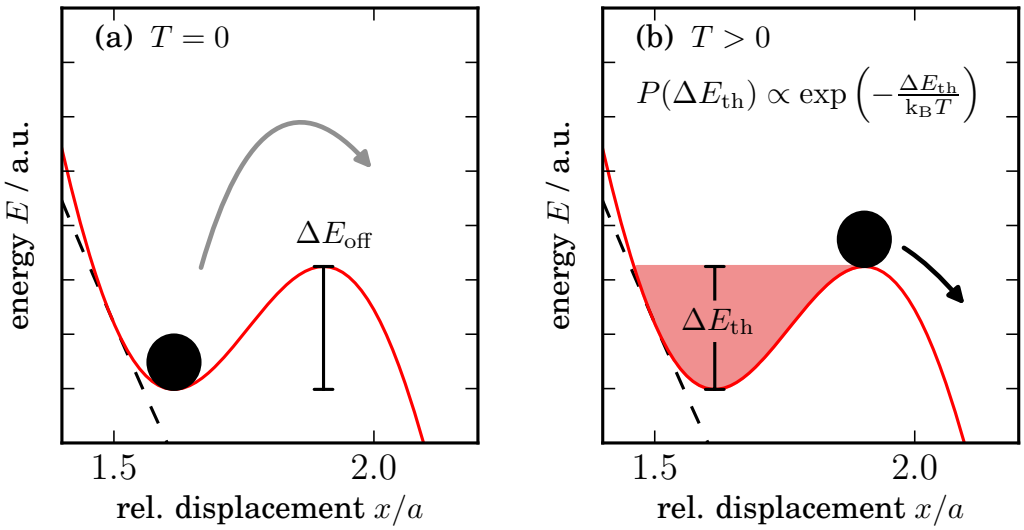

Figure 2.5: Thermally activated Prandtl-Tomlinson model. The tip is activated with the thermal energy ΔE_{th}, whereas the amount of thermal activation is determined stochastically by the Boltzmann factor $\exp(-\Delta E_{\mathrm{th}}/\mathrm{k_B}T)$. This thermal activation can enable the tip to jump to the next minimum before the energy barrier ΔE_{off} has fully vanished.

2.3 Mechano-Kinetic Model

While the TA-PT model can be used to describe scenarios, in which the friction force increases with velocity (*velocity strengthening*) and decreases with temperature, it cannot explain a decrease of friction with velocity (*velocity weakening*), or non-monotonicity in the temperature dependence. Recently, a number of experiments uncovered velocity weakening at specific temperatures T, as well as non-monotonic variations of friction with temperature in nanoscale friction (Schirmeisen et al., 2006; Jansen, 2009; Barel et al., 2010a; Barel et al., 2010b).

The mechano-kinetic (MK) model, which was introduced by Filippov et al. (2004), and which is based on previous models (Persson, 1995), aims to explain these experimental findings. Whereas in the TA-PT model the tip needs to overcome an energy barrier ΔE_{off} between two adjacent minima, the MK model considers a similar process, in which a local bond is broken by surmounting an analogous barrier. In addition, the MK model introduces a second energy barrier ΔE_{on} which needs to be overcome in order to form new bonds. This

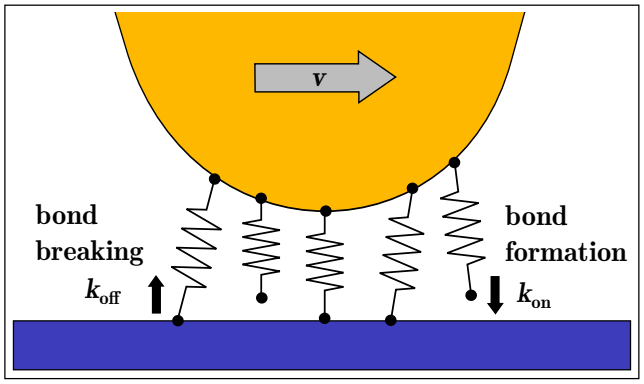

Figure 2.6: Illustration of the MK model. The frictional contact is made up of N individual bonds, realized as springs which are permanently connected to a moving support (yellow). Detachment and reattachment of the bonds to the substrate (blue) is thermally activated, with the respective rates k_{off} and k_{on}.

stands in contrast to the TA-PT model, which assumes rapid relaxation into a local energy minimum and includes a finite bonding energy barrier at all times. Furthermore, since even single asperity contacts are usually made up of many atomic bonds (compare Fig. 2.2d), the MK model considers a multitude of N individual bonds. Each bond is modeled as a spring, and all of these spring are connected in parallel to a common moving support (cf. Fig. 2.6).

The detachment rate k_{off} and reattachment rate k_{on} for the individual contacts are devised as Arrhenius-type processes (Barel et al., 2010a):

$$k_{\mathrm{off}} = \Omega_{\mathrm{off}} \exp\left(-\Delta E_{\mathrm{off}}(1 - f_i/f_c)^{3/2}/\mathrm{k_B}T\right) \tag{2.11}$$

$$k_{\mathrm{on}} = \Omega_{\mathrm{on}} \exp\left(-\Delta E_{\mathrm{on}}/\mathrm{k_B}T\right) \tag{2.12}$$

with the attempt rates Ω_{off} and Ω_{on}, and the energy barriers ΔE_{off} and ΔE_{on} for detachment and reattachment, respectively. The term $(1 - f_i/f_c)^{3/2}$ describes the vanishing of the energy barrier, as the current elastic force f_i of the i-th contact approaches the critical rupture force f_c (Filippov et al., 2004; Sang et al., 2001).

Fig. 2.7 depicts results of simulations performed with the MK model in direct comparison with results obtained from FFM experiments, as found by (Barel et al., 2010a). It can be noted that the MK model is able to reproduce both velocity weakening and velocity strengthening at different, constant temperatures, and that the temperature dependence of friction exhibits local maxima. Although the simulations are qualitatively in good agreement with the experiments, the quantitative description of the data is less than optimal. Especially the very steep drop of the simulated friction forces down to nearly zero for low temperatures in Fig. 2.7a, as well as vanishing friction for low velocities above T=200 K do not correspond well to the experimental findings. Thus, the validity

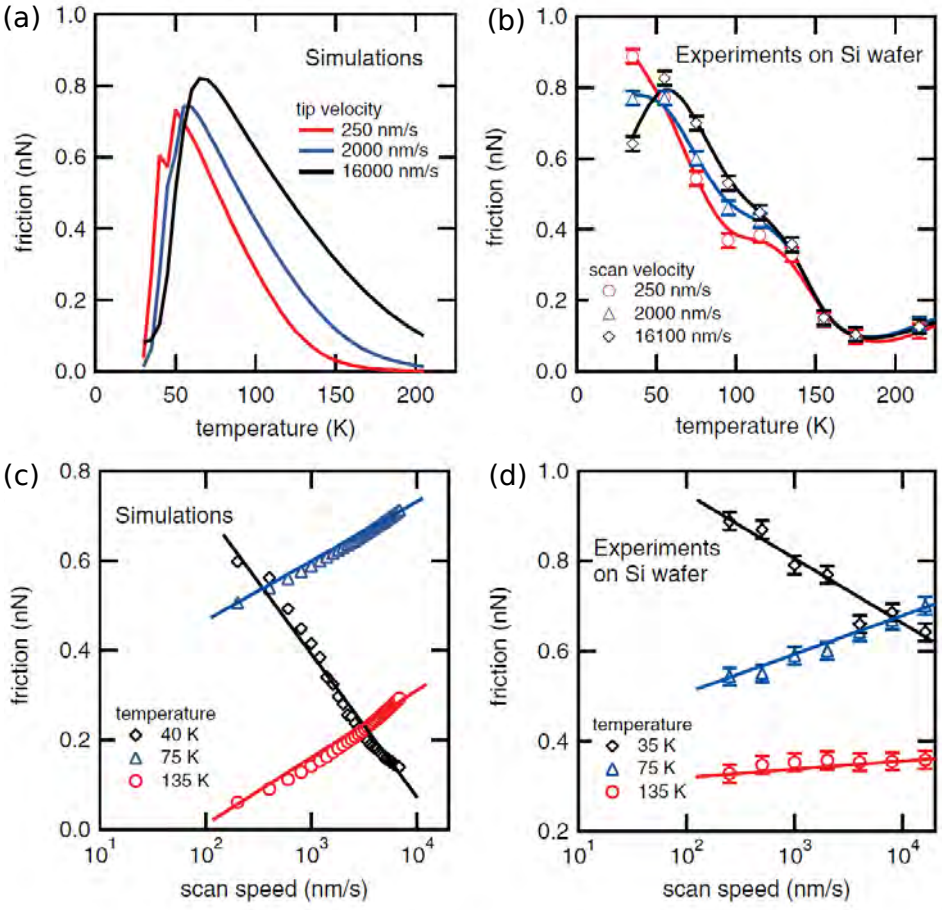

Figure 2.7: Friction versus temperature (a,b) and scan speed (c,d) for a Si tip on a Si wafer. Simulations (a,c) and experimental results (b,c) show overall good qualitative agreement. From (Barel et al., 2010a)[1].

of this particular model appears to be limited to a rather narrow range around the peak in the temperature dependence.

An extension of the mechano-kinetic model ('capillary MK model') includes a distribution of rebinding energy barriers instead of a single energy barrier ΔE_{on}. This feature was introduced to describe capillary condensation in nanoscale contacts, leading to less steep slopes in the temperature dependence of friction

[1]Reprinted Fig. 2.7 with permission from (Barel et al., 2010a) as follows: I. Barel et al. (2010a): *Multibond Dynamics of Nanoscale Friction : The Role of Temperature*. Physical Review Letters, **104**:6, 066104. DOI: 10.1103/PhysRevLett.104.066104. Copyright (2010) by the American Physical Society.

(Barel et al., 2012).

The premise of the model, which is to have individual chemical bonds that can be broken and reformed individually, appears reasonable for sample systems with strong short-ranged chemical bonds. An example of such a system is given by silica-on-silica friction, as presented later in Section 6.1. For long-range van-der-Waals-bound interfaces, however, other formulations seem more appropriate, as will be discussed in detail in Section 5.2.3.

2.4 Contact Area Dependence of Friction

While Amontons law states that macroscopic friction does not depend on the area of contact, but that it depends in a linear fashion on the normal load, the corresponding picture for nanoscale friction is very different.

Friction of hard nanoscale contacts has been found to mostly scale linearly with the nanoscopic contact area A_n, as first unveiled by Bowden et al. (1950). A_n reflects atomically smooth contacts, which are formed by the asperities of an interface, and its amount is usually a small fraction of the apparent macroscopic contact area A_m due to surface roughness, as illustrated in Fig. 2.2.

Recently it has been proposed that even A_n does not reflect the 'true' contact size. Instead, only a fraction of its constituting atoms form bonds between the surfaces (Mo et al., 2009; Mo et al., 2010; Liu et al., 2012; Gotsmann et al., 2013), and contribute to the local surface interaction (cf. Fig. 2.2d). The comprehension of this atomic scale surface contact segmentation is just beginning to emerge. For van-der-Waals-bound interfaces without individual covalent bonds, the precise definition of a contact size becomes equally complicated.

It has been shown, both experimentally and by theoretical considerations, that the nanoscopic contact area A_n of rough macroscopic interfaces scales linearly with the normal load F_N (Baumberger et al., 2006). In order to arrive at this conclusion, the Greenwood-Williamson model can be employed (Greenwood et al., 1966). In this model, a multi-asperity contact is considered, with one rough surface pressing onto a flat surface. Its individual elastic asperity caps are of equal curvature, but expose a Gaussian height distribution. The asperity contact mechanics are tractable by applying elastic contact mechanics, as devised by Heinrich Hertz (*Hertzian contact*, cf. (Popov, 2010)).

Specifically, these contacts resemble an elastic sphere in contact with an elastic half space, which, for a single contact and by neglecting adhesion effects, yields the relation $A_{\mathrm{n}}^{(i)} \propto {F_N}^{2/3}$. The uneven distribution of normal loads onto the different asperities leads in good approximation to a linear relation

$A_n \propto F_N$ for the whole contact (Popov, 2010).

The contact between an AFM tip and a flat substrate can in first approximation also be modeled as a single Hertzian contact. Although its contact area $A_n^{(i)}$ is not linear in F_N, it can be shown that the friction force F_F is proportional to F_N for amorphous tip materials (Ritter et al., 2005).

Moreover, Mo et al. (2009) presented MD simulations of an amorphous carbon tip on a diamond sample, demonstrating that even the atomic contact area A_a, representing the number of atomic bonds in the interface, can scale linearly with the applied load. This prediction is supported by measurements of quantized heat transport in AFM tips (Gotsmann et al., 2013).

Variations of the normal load onto nanoscale contacts with approximately constant contact area A_n on the other hand seem to have negligible influence on friction forces, at least if the external normal force is small compared to the adhesion. Dietzel et al. (2009) presented corresponding findings for the case of flat, van-der-Waals-bound nanoparticles.

As a first approximation, frictional forces of extended contacts emerge as the linear superposition of the lateral force contributions from individual atoms. This can be derived from a multi-contact extension of the PT model, in which no coupling between individual contacts is considered, and full relaxation into the individual energy minima is assumed. Since for macroscopic contacts the atomic contact area scales linearly with the normal load, this leads to an initial comprehension of the macroscopic first law of Amontons.

A more sophisticated setting arises when interactions between adjacent bonds have to be considered. This is the case e.g. for nanoparticle friction and other extended nanocontacts. In such systems, friction phenomena can rather be governed by the geometric arrangement of the surface atoms than by the apparent contact area (Shinjo et al., 1993): the friction between two surfaces with matching atomic lattice geometries will be comparatively high, since each atom contributes to the enhancement of friction, leading to linear scaling of friction with contact area. But in the case of a mismatch of lattice geometries, e.g. due to different lattice constants, different lattice structures, rotational mismatch or amorphicity, the individual contributions of the atoms to the lateral force will partially cancel each other out, resulting in a reduction of friction compared to the fully matching geometry (cf. Fig. 2.8). This effect is called *structural lubricity* or *superlubricity*. Müser et al. (2001) have conducted MD simulations in this matter and found a power law for the dependence of static friction F_S on the number of atoms N of the general form

$$F_S = F_0 \cdot N^{\gamma}, \tag{2.13}$$

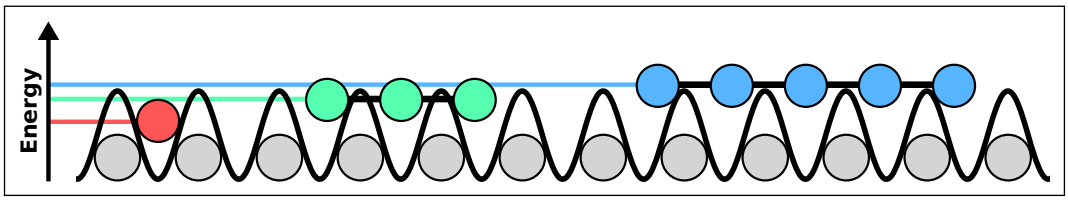

Figure 2.8: Basic concept of structural lubricity. Due to structural mismatch and strong intra-surface interaction of the surface atoms the interface does not fully relax into the energy minima of the interaction potential. If the contact area is increased (here: one atom (red), and up to five atoms (blue)) the energy barrier of each individual atom decreases.

where F_0 is the friction of a single atom, and γ determines the scaling. For commensurate interfaces, the scaling is linear (γ=1), while for amorphous interfaces a sub-linear increase is expected (γ=0.5). In addition, the case of mobile adsorbates (i.e. atoms or molecules) located in the interface can be considered (He et al., 1999). These adsorbates can act as intermediaries which can relax into energy minima, leading to a linear dependence of friction on the number of surface atoms.

The emergence of the superlubricity effect depends on the stiffness of the constituent interfaces. Since the interaction between atoms of a single surface needs to be strong compared to the inter-contact interaction, it is mostly limited to van-der-Waals-bonded interfaces. Kim et al. (2009) have demonstrated by means of MD simulations and qualitatively, using a multi-bond variant of the PT model with local bond interaction (the so-called Frenkel-Kontorova-Tomlinson model), that superlubricity can degenerate into regular linear friction scaling if the interface atoms of incommensurate surfaces are allowed to relax to a sufficient extent. The atoms thereby form quasi-commensurate contacts, which possess metastable intermediate states exhibiting slip discontinuities, leading to enhanced dissipation when compared to strongly interacting bonds.

2.5 Contact Ageing and Static Friction

The concept of static friction describes the following often observed phenomenon: if a contact is kept stationary for some extent of time, then the force F_S required to initiate sliding is usually larger than the kinetic friction force F_F acting between the surfaces in relative motion. On large to intermediate spacial scales, static friction is observed on a regular basis (Persson, 1998), and is believed to

be of fundamental importance in the dynamics of earthquakes (Scholz, 1998).

In general, the transition from sliding to static friction is not of a sudden, binary character. Instead, it arises from a gradual process, which is termed *contact ageing*. This process can be quantified, when a previously sliding body is kept in stationary contact with the supporting counter-body for a certain hold time t_{ht}, after which the static friction F_S is measured through initiation of sliding. This experiment can then be repeated over a range of hold times to measure $F_S(t_{\mathrm{ht}})$. The earliest records of contact ageing investigations are attributed to Charles-Augustin de Coulomb (1736–1806). For friction between two oak plates lubricated with tallow he found a power law (Persson, 1998)

$$F_S(t_{\mathrm{ht}}) = K_1 + K_2 \cdot {t_{\mathrm{ht}}}^{0.2} \tag{2.14}$$

and explained his findings with the gradual interlocking of wood fibers.

The frictional contact ageing effect has furthermore been observed in rock friction (Ruina, 1983; Scholz, 1998), where it is usually described in terms of phenomenological rate-and-state theories (Dieterich, 1978; Rice et al., 1983). An exemplary formulation of a rate-and-state theory can be given as (Baumberger et al., 1999)

$$\mu(v, \phi) = \mu_0 + B \ln\left(\frac{\phi}{\phi_0}\right) + A \ln\left(\frac{v}{v_0}\right). \tag{2.15}$$

In this formula, $\mu = F_F/F_{\mathrm{N}}$ is the friction coefficient, v is the relative velocity representing the rate, and ϕ is a state variable, which can be interpreted as the age of the contact since its formation after the previous slip. A, B and μ_0 are phenomenological fit parameters, and ϕ_0 and v_0 are reference constants. For the special case of $v = 0$, rate-and-state theory predicts a logarithmic increase of the static friction with hold time, which even fits to the measurement data found by Coulomb. For frictional systems exhibiting stick-slip type kinetic friction, contact ageing during the stick phase can have significant influence on the overall friction (Persson, 1998). Yang et al. (2008) have extended this idea by introducing a second state variable θ, which describes the evolution of the contact during the slip phase. They report experimental findings of initial relative motion of macroscopic contacts across microscopic distances, which they are able to fit with their extended rate-and-state model. This observation is explained as a build-up of an ensemble of interface asperities during the onset of relative motion.

A commonly found formulation for contact ageing with respect to the contact area can be derived in the context of rough multi-contact interfaces exhibiting thermally activated plastic flow or viscoelastic compliance (Baumberger et al.,

2006):

$$A_n(t) = A_{n,0}\left(1 + m \cdot \ln\left(\frac{t}{\tau} + 1\right) + \mathcal{O}(\ln^2)\right). \tag{2.16}$$

Here, the nanoscopic contact area A_n depends on an initial contact area $A_{n,0}$ at $t = 0$, a characteristic crossover time τ, and a measure m for the contact increase per logarithmic time. Since for microscopic contacts the friction force is in first approximation proportional to the real contact area (except if structural lubricity is involved), this so-called geometric contact ageing effect can explain frictional ageing as well. Equation (2.16) is devised in the context of multi-contact interfaces, using the Greenwood-Williamson model in combination with plastic flow of the individual sub-contacts (Berthoud et al., 1999). The experiments presented in this work offer premises, which differ fundamentally from the assumptions used in this model: all experimentally realized contacts in this work represent single asperity contacts, but the general concept of logarithmic ageing will still be of use. Jagla (2010) presents additional theoretical considerations regarding creep of interfaces, were a contact increase between a plasto-elastic, atomically flat surface and an atomically rough, rigid surface is found, similar to Eq. (2.16).

The mere existence of distinctive static friction with $F_S \gneqq F_F$ and the associated contact ageing in single asperity contacts was only very recently demonstrated by Li et al. (2011). It was found that the static friction increases with the logarithm of the hold time t_{ht}, similar to the findings for contacts at larger length scales.

As already noted in the context of Section 2.4, Mo et al. (2010) have demonstrated that the model view of only a fraction of the apparent interface being in actual contact can be extended from the multi-asperity domain down to single asperities (see Fig. 2.2d and Section 2.4). This leads to one conceivable mechanism, from which the previously discussed contact ageing in single asperity contacts can arise, namely the delayed formation of atomic bonds in the interface. Further indication for the formation of individual bonds at interfaces is given by experimental findings by Gotsmann et al. (2013) through studies of quantized thermal conductance channels. Liu et al. (2012) presented MD simulations which elucidate the temporal retardation of chemical bond formation. They found that it is due to the dependence of binding energy barriers on the binding state of neighboring binding sites, and results in a logarithmic increase of A_a with t_{ht}.

The mechano-kinetic (MK) model (see Section 2.3) can be interpreted as an attempt to formalize the concept of contact ageing with individual atomic

bonds. It predicts contact ageing according to (Barel et al., 2012)

$$N(t) = N_{\max}(1 - \exp(-t/\tau)) \tag{2.17}$$

where $N(t)$ and $N_{\max}$ are the number of bonds at time t and the maximum number of bonds, respectively. This type of function is quite similar in shape to the ageing law found in Eq. (2.16), except that here an upper limit exists.

For the capillary MK model, which comprises a distribution instead of a single value for ΔE_{on}, one arrives at the expression

$$N(t) = N_0 \times \begin{cases} t/\tau & \text{for } t < \tau \\ \ln(t/\tau) + \gamma & \text{for } t > \tau, \end{cases} \tag{2.18}$$

in which N_0 is the number of bonds at $t \approx \tau$, and γ is a matching constant. This formula is very similar to Eq. (2.16) for $t > \tau$. Here, a linear relation at smaller t is exposed, while for Eq. (2.16) the contact area is approximately constant in this regime.

Another conceivable source of contact ageing is described by Persson (1993a); Persson (1993b): In boundary-lubricated solids, where a layer of adatoms is confined between two sliding bodies, the lubrication layer can exist in a solid-like or in a liquid-like phase. The solid phase results in considerably higher friction between the two bodies as compared to the liquid phase, and the transition between both phases includes a hysteresis in the stress-velocity dependence. The transition from the fluid-like to the solid-like phase is assumed to be governed by nucleation processes, similar to nucleation in crystal growth, leading to a time-dependence of solidification. Typical time scales found relevant for these phase transitions of exemplary simulations using this model, as reported by Persson (1998), lie in the 100 ns regime. Thus, contact ageing, with friction increasing in some instances over hundreds of seconds, cannot be satisfactorily explained by this mechanism alone. Separate dissipation studies with a SFA by Granick (1991) show that, if liquids are closely confined between flat solids, their viscosity can be enhanced by 8 orders of magnitude, with associated relaxation times in the 0.1 s regime.

A variant of a multi-contact model was introduced by Persson (1995), which is based on boundary lubrication and, again, exhibits contact ageing. In this model, one surface is made up of individual elastic blocks, which are connected to a moving support and to neighboring blocks by individual springs. The interaction of the blocks with the rigid counter-body in this model is governed by an adsorbate layer. This layer can exist either in a pinning state, or in an

unpinned state, similar to the mechanism described in the previous paragraph. Furthermore, a critical surface stress σ_a is postulated, which each block needs to overcome, in order to melt the adsorbate layer and switch from the pinned state to a sliding state. The reverse state change is assumed to happen when the relative velocity is again reduced to zero. The mechanism leading to decreasing velocity is modeled by a viscous damping term. When an Arrhenius-type thermal activation for the individual blocks is introduced, the author finds a rich dependence of friction on velocity, as well as contact ageing characteristics, in which the static friction increases with the logarithm of the hold time.

Most contact strengthening processes of frictional contacts are believed to be thermally activated (Jagla, 2010; Barel et al., 2012; Evstigneev et al., 2008; Persson, 1998). In the context of the MK model, this activation manifests itself as an Arrhenius law with the time scale $\tau = 1/k_{\mathrm{on}}$ (Barel et al., 2012) (cf. Eq. (2.11)), while the mechanism responsible for plastic deformation in metals, i.e. the migration of dislocations, is as well Arrhenius-activated.

The actual physical nature of contact ageing in nanoscale friction remains to be uncovered. A clear attribution of the phenomena, as observed in lateral force traces, to a specific physical effect is challenging, because most theories describing those effects predict very similar ageing laws, with approximately logarithmic dependence on hold times and Arrhenius-type thermal activation.

2.6 Nanoparticle Translation: Friction of Extended Asperities

In the undertaking to study the friction of nanoscale contacts experimentally, the actual physical realization of the contact is of crucial importance. Two properties have to be highlighted in this context: First, the contact has to provide well-defined conditions in order to allow reproducibility and to relate the experimental findings to features of the contact. Furthermore, a means is required to accurately and repeatedly quantify the friction of the contact.

Since its invention, the friction force microscope (FFM) (Mate et al., 1987) has been the tool of choice for nanoscale friction experiments (Szlufarska et al., 2008), because it allows to measure friction of smallest contacts down to interfaces consisting of just a few atoms, and because it delivers accuracies in force measurements down into the piconewton range. The contacts realized with an FFM tip, on the other hand, are not as well-defined in respect to its contact area as it could be desired, since no direct observation channel for this

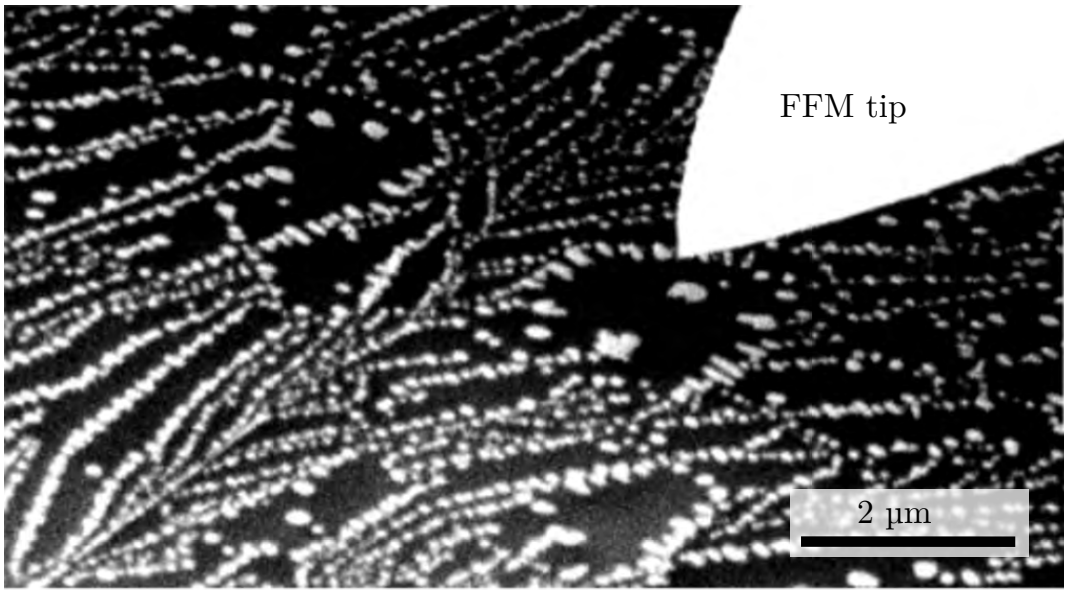

Figure 2.9: SEM micrograph of an FFM tip in contact with a surface covered with nanoparticles (bright spots), grown predominantly along step edges of the substrate.

property is available. While the contact area can be estimated from models regarding elastic contact mechanics through the use of idealized tip geometries in combination with *ex situ* SEM measurements, or by measuring associated properties such as adhesion, a large margin of error usually remains (Schwarz et al., 1997). Changes in the contact area due to wear can amplify this difficulty.

The issue becomes more complicated if one is interested in the friction of extended nanocontacts. While it is possible to increase the tip-sample contact area by wearing and thus flattening the tip, this method is prone to errors, because of the intricacy to align the surface of a flat tip with the substrate surface. Schwarz et al. (1997) described a method to fabricate large spherical tips and use them for nanoscale friction measurements, thus avoiding this alignment issue. However, the method of relying on idealized geometries for contact size estimation diminishes its utility.

Another well-established system (Carpick, 1997) to probe microscopic frictional qualities of two solids in contact is the surface force apparatus (SFA), as introduced by Israelachvili et al. (1973). The SFA consists of two atomically smooth substrates, e.g. mica sheets glued onto two cylindrical mounts, which are arranged in a crossed, perpendicular orientation. These mounts are pressed together to form the frictional contact. The setup features actuators used

to translate the sheets relative to one another, as well as sensors to measure the separation, normal force, lateral force and the contact area. A limiting factor for experiments using the SFA is the restriction to use atomically smooth substrates, resulting in the almost exclusive choice of mica for the contacting bodies. Furthermore, the typical contact areas realized in an SFA of $\sim 700\,\mu m^2$ are orders of magnitude larger than the typical contact areas achieved in FFM experiments, which range from $1\,nm^2$ to $10\,nm^2$ (Persson, 1998). As a result, a large gap of contact sizes inaccessible by those two methods exists. In addition, the typical SFA implementation operates in ambient or liquid environments, employing hydrophilic mica surfaces. This setup thus thwarts experiments regarding dry friction.

A quite novel but very potent technique to probe the frictional properties of extended nanocontacts is the method of nanoparticle manipulation (Lüthi et al., 1994; Sheehan et al., 1996; Ritter et al., 2005; Dietzel et al., 2007; Schirmeisen et al., 2009; Rovatti et al., 2010; Ritter et al., 2013). To investigate frictional properties using this technique, a nanoparticle (NP) is pushed or dragged over a substrate by an AFM tip. During the translation, the lateral force needed to move the particle can be recorded, yielding the friction force between particle and substrate. The AFM can furthermore be used to image the surface, including the nanoparticles. For this work, NP manipulation was implemented at three different AFM setups.

The method of friction measurements using nanoparticle manipulation offers a number of key advantages over the more established methods, such as direct tip-sample contact measurements in FFM or SFA experiments. First, it enables the investigation of nanoscopically smooth extended contacts, e.g. when the particles are prepared onto the substrate by thermal evaporation, eliminating tilt effects arising from worn AFM tips. Furthermore, it reduces uneven pressure distributions in the contact, which result from utilizing curved surfaces, as found in SFA or for AFM tips with large tip radii. The availability of many particles with different sizes and geometries within a single scan-frame on a substrate allows to probe many contact configurations in short succession with a single sensor. An introduction of additional uncertainty through calibration errors into comparative analysis can thus be averted.

In nanoparticle manipulation, the contact between substrate and NP is usually much larger than the contact between AFM tip and particle. This allows for better heat flow between particle and substrate compared to the flow between tip and particle, since heat flow increases approximately linear with contact area (Gotsmann et al., 2013). If an AFM with sample-only heating or cooling is employed, as it is described in Section 3.5.4, this leads to a much

better defined contact temperature.

Finally, FFM measurements with direct tip-sample contacts are severely restrictive in the choice of the materials which form the frictional contact. In particular, the class of materials from which FFM tips can be mass-produced today is rather limited. SFA measurements are for the most part constrained to probe mica-on-mica interaction, augmented by functionalization of the surfaces or by inclusion of confined liquids. Nanoparticle manipulation, on the other hand, can be performed with a variety of combinations of substrates and nanoparticle materials.

Details of the nanoparticle manipulation technique and the manipulation protocol employed in this work are described in Chapter 4.

3 Atomic Force Microscope

The invention of the scanning tunneling microscope (STM) by Binnig et al. (1982) and the subsequent introduction of the atomic force microscope (AFM) by Binnig et al. (1986) have laid the foundation for a whole new field of research in surface science, due to the ability of these techniques to image surfaces with extremely high resolution in all three spacial dimensions, even down to atomic length scales. Beyond probing the topography, these scanning probe microscopy (SPM) methods have evolved to aid in the investigation of numerous physical surface properties, such as forces, energy dissipation mechanisms, or the electronic density of states. The advancement from AFM towards the friction force microscope (FFM) by Mate et al. (1987) and the combined AFM-FFM by Marti et al. (1990) have extended the available capabilities profoundly by enabling friction force measurements at nanometer scales.

After introducing the general working principle of an AFM in Section 3.1, the details of force measurements normal and lateral to the sample surfaces, as well as the corresponding force calibrations, are presented in Sections 3.2 to 3.4. Finally, the particular instrumentation used in this work is introduced in Section 3.5, with a special emphasis on the three different utilized AFM systems in Sections 3.5.3 to 3.5.5.

3.1 Basic Principles of AFM Operation

In an AFM or FFM, a probe is positioned in close proximity to the sample surface of interest (see Fig. 3.1) in order to assess its qualities. This probe consists of a very sharp tip (typical cap radius $\sim 5\,\mathrm{nm}$), which is mounted at the end of a flexible cantilever beam. A typical example of such a sensor made from silicon is depicted in Fig. 3.3.

Tip and sample can be moved relative to one another in all three spatial dimensions, with precisions as low as fractions of an angstrom ($1\,\text{Å}=10^{-10}\,\mathrm{m}$). This is usually achieved by fixating the cantilever support, and attaching the sample to a piezo tube. The piezo tube converts an applied voltage into a small spacial displacement due to the inverse piezo-electric effect.

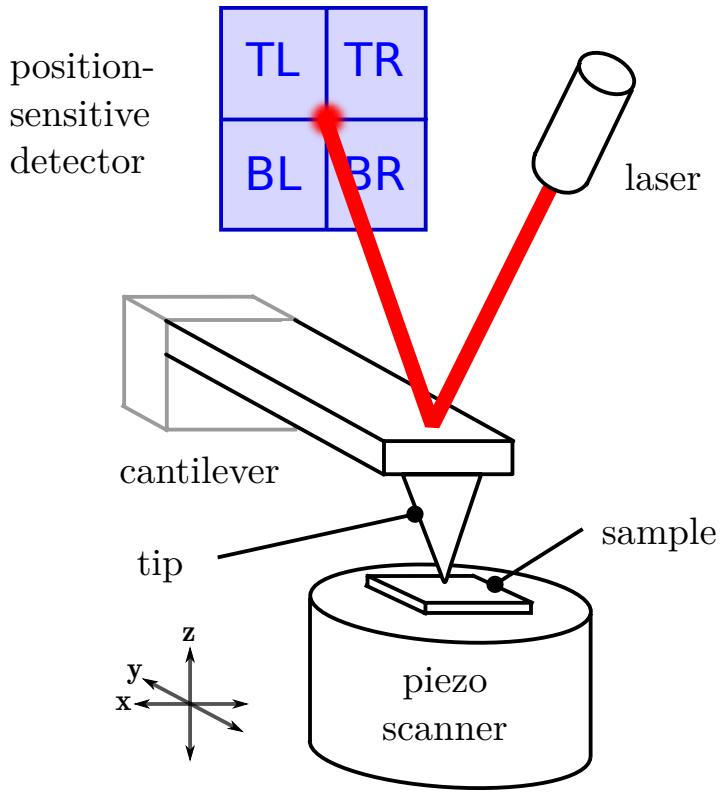

Figure 3.1: General working principle of the AFM and FFM. The sample is attached to a piezo tube which acts as an actuator. The probe consists of a sharp tip, which is attached to a cantilever extending from a fixed support. Forces acting on the tip induce elastic responses in the cantilever, namely bending and twisting, which can be measured with high precision by directing a laser beam onto the back side of the cantilever and detecting the reflection angle with a position-sensitive detector (PSD). In this example, the PSD is implemented as a four-quadrant photodiode. The tip is scanned in a grid pattern over the substrate to produce discretized height- and force-maps of the sample surface.

If the sample exerts a force onto the tip, the cantilever will bend and twist in response. This displacement can be recorded, e.g. by pointing a laser beam onto the cantilever and detecting the angle of reflection using a position-sensitive detector (PSD), realized here as a four-quadrant photodiode. A device equipped with this detection technique allows to measure both normal and lateral forces, thus placing it in the category of a combined AFM-FFM. Other viable methods used to detect the normal cantilever deflection include optical interferometry, or the fabrication of sensors from piezo-electric materials, which allow the extraction of forces from the resulting piezo-electric voltages. With a four-quadrant-diode, the normal force F_N and the lateral force F_L, which are applied to the tip, can be measured by exploiting their linear relation with the corresponding displacement signals U_{T-B} and U_{L-R} for low displacement amplitudes. The signals U_{T-B} and U_{L-R} are easily derived from the voltage signals of the four sensor quadrants (cf. Fig. 3.1) according to

$$U_{T-B} = (U_{TL} + U_{TR}) - (U_{BL} + U_{BR}) \tag{3.1}$$

$$U_{L-R} = (U_{TL} + U_{BL}) - (U_{TR} + U_{BR}), \tag{3.2}$$

and are a measure of the normal and torsional bending, as depicted in Fig. 3.2. The corresponding linear relation to the actual force values can then be given as (Bhushan, 2004)

$$F_N = \theta_z \cdot U_{T-B} - F_{N,\mathrm{ref}} \tag{3.3}$$

$$F_L = \theta_x \cdot U_{L-R} - F_{L,\mathrm{ref}}. \tag{3.4}$$

The calibration factors θ_z and θ_x have to be determined by appropriating a calibration procedure for each individual sensor (see Section 3.4). For actual experiments, the force offsets $F_{N,\mathrm{ref}}$ and $F_{L,\mathrm{ref}}$ are typically adjusted to zero for the disengaged sensor by repositioning the laser spot on the PSD.

The AFM is usually operated in a feedback loop, which acts to keep the tip-sample separation constant. This is accomplished by comparing the normal force signal with a predefined set point F_N^{SP} and by subsequently adjusting the displacement of the piezo tube in normal direction (referred to as the z-axis) accordingly, through a proportional-integral-derivative controller. The axis parallel to the long cantilever axis is called the y-axis, and the remaining direction, perpendicular to the long cantilever axis and parallel to the surface, is called the x-axis.

In order to characterize the surface topography, the tip is scanned over the substrate in a grid pattern along the x- and y-axis, while the z-displacement as

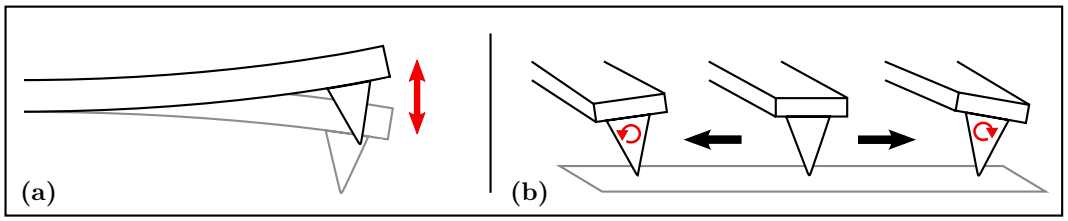

Figure 3.2: Bending modes of an AFM cantilever: (a) normal and (b) torsional deflection. The normal bending mode is excited to oscillations in NC mode. When operated in CT mode, the normal deflection corresponds to the normal force F_N, while the torsional deflection is proportional to the lateral force F_L.

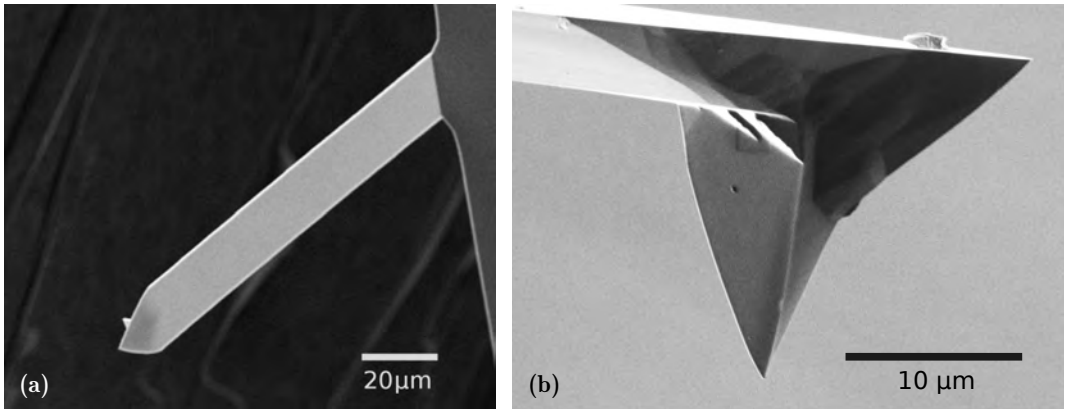

Figure 3.3: SEM micrographs of an AFM sensor. (a) View onto the back side of the cantilever. The cantilever is attached to a carrier chip at the right edge of the image. On the left side the end of the tip is visible as a small, bright triangle. (b) Close-up view of a sensor tip from the side, provided by Johannes Sondhauß.

well as the PSD-readouts are recorded. Combining the recorded z-coordinates with the emitted x- and y-coordinates then allows for the reconstruction of a plane of constant normal force $F_N = F_N^{\mathrm{SP}}$. This plane can be interpreted in good approximation as the surface of the sample. Lateral force measurements and calibrations are generally carried out along the x-axis, since in that direction the lateral force sensitivity is at its maximum. The generation of the scan voltages, the recording and display of the measurement signals, and the feedback operation are handled by a computer-operated real-time digital signal processing system.

3.2 Normal Force Measurement

A multitude of forces can act between an AFM tip and a sample, such as Pauli repulsion, van-der-Waals-, friction-, elastic, electrostatic or magnetic forces (cf. (Bhushan, 2004)). Nonetheless, many tip-sample interactions are dominated by only very few of these forces. The following conceptual considerations regarding normal forces in AFM measurements will be constrained to interactions with a Lennard-Jones-type potential V_{LJ}:

$$V_{\mathrm{LJ}}(z_{\mathrm{tip}}) = \epsilon \left[\left(\frac{z_0}{z_{\mathrm{tip}}} \right)^{12} - 2 \left(\frac{z_0}{z_{\mathrm{tip}}} \right)^{6} \right]. \tag{3.5}$$

In this equation, $-\epsilon$ signifies the minimum value of V_{LJ}, located at the tip position $z_{\mathrm{tip}} = z_0$. The first summand describes short-range chemical forces such as Pauli repulsion, while the second summand originates from long-range van-der-Waals forces and permanent dipole-dipole interactions. The cantilever spring induces a potential

$$V_{\mathrm{Cant}}(z_{\mathrm{tip}}) = \frac{1}{2} k_z (z_{\mathrm{tip}} - z)^2 \tag{3.6}$$

which describes the interaction between the cantilever support at position z and the tip at z_{tip} through the cantilever of stiffness k_z, according to Hooke's law. During AFM operation the tip experiences a superposition of these two potentials. The following conventions will be used hereafter: F_N shall be defined as positive if the cantilever bends away from the sample, and as zero for no bending. The z coordinate shall be defined as increasing with the tip-sample separation.

For typical topography imaging applications of the AFM, the tip-sample interaction in normal direction is kept constant and the topography of the sample is traced by the tip. The feedback loop controlling the tip-sample separation of the AFM can be operated with different process variables, corresponding to different ways of measuring the normal force. Two operational modes which were used in this work, namely *contact mode* and *non-contact mode*, will be discussed below.

3.2.1 Contact Mode

The most straightforward form of normal force measurement and tip-sample distance control utilizes the already introduced linear relation between the measurement signal U_{T-B} and the normal force F_N, as given in Eq. (3.3).

The correlation between normal deflection of the cantilever and the measurement signal U_{T-B} can be probed by performing a so-called force-distance measurement, which is sketched in Fig. 3.4a. For this procedure, the tip starts at a position away from the surface (1). The tip-sample distance is then incrementally reduced, while U_{T-B} and the z coordinate are recorded. Eventually, the tip snaps into contact with the surface (2). The z-coordinate is further reduced over a short distance, increasing the repulsive tip-sample force to higher values in the linear interaction regime (3). Consecutively, the direction of motion is reversed, resulting at first in decreasing the tip-sample force. Finally, when the restoring force is equal to the adhesion force, the tip snaps off from the surface (4). The snap-off force thus is a measure for the adhesion, and the slope of the force curve in the range between (2) and (3) allows to map the measured signal U_{T-B} to a specific cantilever deflection.

Fig. 3.4a shows that U_{T-B} and z_{tip} exhibit a hysteresis at the position marked as (*), when the support is approached and retracted consecutively. In Fig. 3.4b, the reason for this bifurcation is outlined. The combined potential $V_{\mathrm{Total}} = V_{\mathrm{LJ}} + V_{\mathrm{Cant}}$ exhibits two distinct minima in the hysteresis region of z. Which minimum is occupied by the tip at any time depends on the movement history (approach or retract movement). For a sufficiently large or small separation one minimum vanishes, thus inducing a jump of the tip. The general mechanism is very similar to the multi-well system of the PT model for lateral forces (cf. Section 2.1).

In the region of this hysteresis, the contact is unstable during scanning, since sudden changes in V_{LJ} can induce a tip jump. This makes it unfeasible to use a value in the corresponding F_N-range as the normal force set point F_N^{SP}. As a consequence, the normal tip-sample force cannot be set to an arbitrarily small value when using the contact mode. Typically, in contact mode F_N^{SP} is set to positive values, which corresponds to repulsive tip-surface interaction.

Even comparatively small tip-sample interaction forces can be sufficient to induce unwanted surface modifications, such as manipulating nanoparticles when only topographic imaging is pursued. Two schemes are commonly deployed to avoid the snap-in instability issue and allow for lower tip-sample interactions. One method is to select a sensor with sufficiently high normal cantilever spring constant k_z, so that there will always be just one minimum (cf. Section 2.1). The main disadvantage of this approach is that the force sensitivity in CT mode will decrease with increasing k_z. Since the lateral spring constant k_x is coupled to k_z by material elasticity and cantilever geometry (see Section 3.4), conventional high-k_z cantilever are also very limited in lateral force sensitivity. Because a high lateral force resolution is essential for nanotribological measurements,

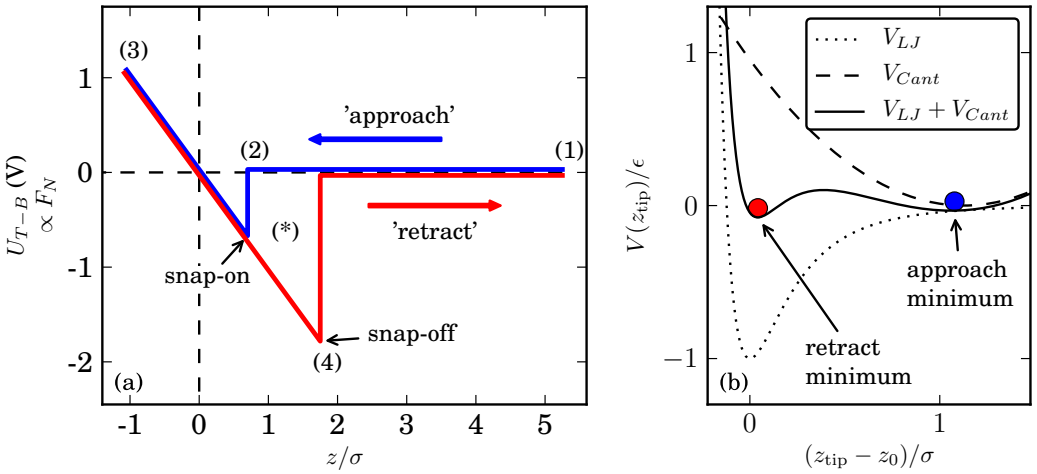

Figure 3.4: AFM force-distance hysteresis. (a) shows the sketch of a typical force-distance curve, where the deflection signal U_{T-B} is plotted against the support position z. The measurement begins with the tip separated from the surface (1). U_{T-B} is set to zero by adjusting the PSD. Subsequently, the tip is approached towards the surface, and, eventually, the tip performs a snap-on towards the surface (2). Further reduction of z leads to a linear increase of the deflection signal, until at (3) the direction is reversed. When the pulling force exceeds the adhesion force the tip executes a snap-off from the surface (4). The z-coordinate of the support, at which the tip is in contact and $U_{T-B} = F_N = 0$ is satisfied is defined as $z = 0$, which identifies the actual surface. (b) shows the normal interaction potential V for a tip-sample separation corresponding to position (*) in (a). Two potential minima coexist within this region, and the tip is located in either one of them, depending on the movement history (*approach* or *retract*). When the currently occupied minimum vanishes, the tip jumps to the remaining minimum. In this particular example, k_z was set to $1.5\epsilon/\sigma^2$.

this approach is usually not viable. A second route corresponds to exciting soft cantilevers to perform oscillations in normal direction, as described in the following section.

3.2.2 Non-Contact Mode

In CT mode, the static deflection of the cantilever is used as a measure for the normal forces. Alternatively, an AFM can be operated in dynamic modes, in which the cantilever is excited to perform oscillations.

A number of different dynamic AFM modes exist, which can be classified

according to their force detection methods and cantilever excitation techniques (Bhushan, 2004). For this work the method of frequency-modulated dynamic AFM was used (Albrecht et al., 1991), which will be referred to as non-contact (NC) mode. In this mode the cantilever is self-oscillated at the current resonance frequency f. This is implemented by measurement of the normal deflection signal U_{T-B}, consecutive amplification, and, after adding a frequency shift of $\pi/2$, applying this signal to a piezo shaker. The piezo shaker is located near the cantilever, and is used drive the cantilever oscillation. The amplification stage consists of an automatic gain control feedback unit, which continuously adjusts the amplification gain, so that the oscillation amplitude is kept constant.

To measure the oscillation frequency f, a phase-locked loop (PLL) detector is utilized, allowing for frequency detection with very high precision. If the tip is fully retracted from the surface, f is equal to the free resonant frequency f_0 of the sensor, since it only sees the harmonic spring potential of the cantilever V_{Cant} (cf. Fig. 3.4b). But when the separation between cantilever support and surface, z, is gradually reduced, the tip will eventually start to see a deformation of the total potential due to the normal surface potential, as approximated by a Lennard-Jones potential V_{LJ}. This deformation of the potential leads to a characteristic shift Δf in the resonance frequency (Giessibl, 2001). Δf is then used as the process variable for the feedback circuit which regulates the tip-sample distance. This method allows to acquire images with very low tip-sample interaction, thus enabling the recording of topography images of NP-based sample systems without modification of the sample. The hysteresis observed in CT mode is suppressed, since the cantilever is preloaded at the onset of tip-sample interaction. The cantilever stiffness is 'virtually' increased. Furthermore, lateral forces are greatly reduced, since the contact is completely broken in each oscillation cycle. Thus, this method allows to image NP-decorated sample surfaces without significant modification.

While all NC mode measurements in this work were performed in the low repulsive force regime, very sharp tips allow for measurements in which the tip remains exclusively within the attractive force regime. This property lend the *non-contact* mode its name.

3.3 Lateral Force Measurement

Shortly after its introduction by Binnig et al. (1986), the concept of the AFM has been modified by Mate et al. (1987) to allow for the measurement of lateral forces F_L parallel to the surface. This type of microscope was called *friction*

force microscope (FFM).

The commonly implemented layout of an FFM is an extension of the AFM design. While the original AFM featured only a normal force detection facility, in the FFM a lateral force detection channel was added. The layout of an AFM as depicted in Fig. 3.1 already includes a four-quadrant PSD. It thus enables the detection of lateral forces F_L through a quantity U_{L-R} proportional to the torsion of the cantilever beam (see Fig. 3.2b).

The zero-force reference $F_{L,\mathrm{ref}}$ of the lateral force signal is usually not constant when piezo displacement or normal force are varied. This is due to the short cantilever axis in general not being parallel to the substrate. Hence, the normal force contributes a component to the cantilever torque, which results in a F_N-dependent value of $F_{L,\mathrm{ref}}$. Since the lateral displacement of a typical piezo tube follows the shape of a spherical shell, the tilt effects vary with the x- and y-coordinate.

This issue of a mutable lateral reference $F_{L,\mathrm{ref}}$ is commonly addressed by recording lateral forces in both directions along the x-axis, resulting in a so-called *friction loop*. By assuming that the absolute values of the lateral forces are isotropic in the direction of the x-axis, the value of $F_{L,\mathrm{ref}}$ can be determined as the mean $\langle\cdot\rangle$ of the signal vectors measured in both directions, $U^{\rightarrow}_{L-R}$ and $U^{\leftarrow}_{L-R}$:

$$F_{L,\mathrm{ref}}/\theta_x = \langle U^{\rightarrow}_{L-R}, U^{\leftarrow}_{L-R}\rangle, \tag{3.7}$$

yielding the rectified forces as $F^{\leftrightarrows}_L = U^{\leftrightarrows}_{L-R}\theta_x - F_{L,\mathrm{ref}}$. The calibration factor θ_x needs to be determined in a separate calibration step, as described in Section 3.4. A typical example of a friction loop is presented in Fig. 3.5. The linear ramp at the beginning of each trace corresponds to the torsional turnaround of the sensor, where the tip is in stationary contact with the surface, and has to be discarded for the friction calculation. After correcting the zero point by subtracting $F_{L,\mathrm{ref}}$, the mean kinetic friction F_F can be calculated as the mean of the absolute lateral force values:

$$F_F = \langle |F^{\rightarrow}_L|, |F^{\leftarrow}_L|\rangle. \tag{3.8}$$

The total dissipated energy E_{diss} is equal to the area enclosed between the forward scan trace $F_{L,\rightarrow}$ and the backward scan trace $F_{L,\leftarrow}$:

$$E_{\mathrm{diss}} = \left| \int F^{\rightarrow}_L(x) - F^{\leftarrow}_L(x)\mathrm{d}x \right|. \tag{3.9}$$

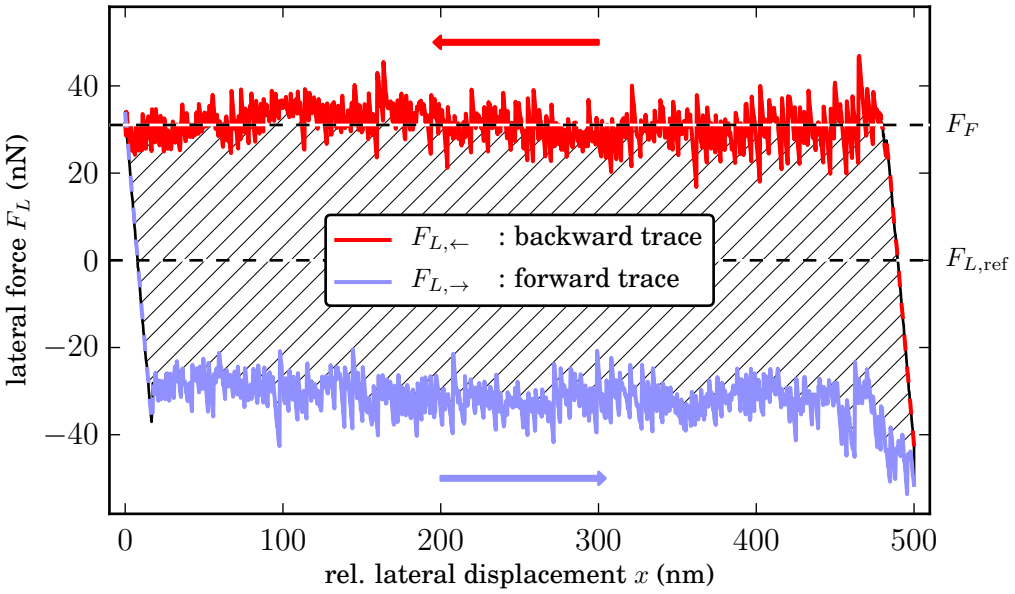

Figure 3.5: Exemplary friction loop of an FFM measurement. Forward trace (blue) and backward trace (red) are recorded in opposite directions along the x-axis, yielding a characteristic lateral force hysteresis curve. The regions of linear increasing force at the beginning of each trace are discarded from subsequent force calculations (black-dashed lines). In this plot F_L has already been corrected by subtracting the mean of both traces, $F_{L,\mathrm{ref}}$. The hatched area corresponds to the dissipated energy E_{diss}; the value of the kinetic friction F_F can be determined by computing the mean of $|F_L|$. The polarity of the F_L signals here is arbitrarily defined to be positive for the backward trace.

3.4 Force Calibration Methods

Recording the voltage signals U_{T-B} and U_{L-R} from the PSD allows for topography scans at constant loads and for the relative comparison of forces measured with the same sensor. But for absolute, quantitative measurements these signals have to be mapped to the actual normal and lateral forces F_N and F_L, respectively. This is achieved in a separate calibration step, in which the normal and lateral calibration constants θ_z and θ_x, as introduced in Eq. (3.3) and Eq. (3.4), have to be determined. These calibration constants can be separated into contributions of the cantilever stiffness k and the detection

sensitivity β in both measurement dimensions (Bhushan, 2004):

$$\theta_z = k_z \cdot \beta_z \tag{3.10}$$

$$\theta_x = k_x \cdot \beta_x. \tag{3.11}$$

The force constants k have to be determined for each sensor individually, while the sensitivities β have to be measured every time a sensor is replaced or the detection optics are readjusted.

3.4.1 Calculation of the Sensor Stiffness

The force constants k_x and k_z of the cantilever can be calculated from the sensor geometry. A formula to calculate the normal spring constant k_z is given by (Bhushan, 2004)

$$k_z = \frac{Ewd^3}{4L^3} \tag{3.12}$$

with the cantilever width w, length L, thickness d, and the Young's modulus E. Similarly, the formula to calculate the lateral spring constant k_x can be expressed as

$$k_x = \frac{Gwd^3}{3Lh_{\text{tip}}^2} = k_z \cdot 2\left(\frac{L}{h_{\text{tip}}}\right)^2 \tag{3.13}$$

where G is the shear modulus and h_{tip} is the tip height (Bhushan, 2004). Both formulae can be obtained from application of the so-called Euler-Bernoulli elastic beam theory and are valid only for small displacements, which are usually not exceeded in FFM measurements.

For the studies presented in this work, silicon cantilevers of the type 'PPP-LFMR' (*NanoWorld AG, Neuchâtel, Switzerland*) were used, except where explicitly noted otherwise. These sensors are designed for especially high lateral force sensitivity by means of a particularly small thickness d, and thus expose a low lateral force constant. Typical dimensions of this cantilever type are given in Table 3.1.

Since the cantilever thickness d has a very high relative variance, and since k_z depends strongly on d, it is necessary to determine the thickness for every sensor separately. This can be achieved by measuring the free resonance frequency f_0 of the sensor in vacuum and calculating the thickness d according to (Nonnenmacher et al., 1991)

$$d = \frac{2\sqrt{12}\pi}{1.875^2}\sqrt{\frac{\rho}{E}}f_0 L^2 \tag{3.14}$$

with the Young's modulus E and the density of mass ρ. The accuracy of the values for width w and length L may be improved by measuring these dimensions with an SEM, but since their fabrication tolerances are much smaller than the tolerance of d it is sufficient to use the nominal values. Applying the cantilever thickness d obtained from Eq. (3.14) together with the supplied nominal values of w and L to Eq. (3.12) yields the normal force constant k_z.

The elastic modulus of crystalline silicon depends on the crystal orientation (Wortman et al., 1965; Hopcroft et al., 2010). In the PPP-LFMR cantilevers, the long cantilever axis is parallel to the <110>-direction of the silicon, according to the manufacturer. Correspondingly, a value of $E = 161\,\mathrm{GPa}$ was used for calculation of the sensor stiffness. The mass density of silicon is given as $\rho = 2330\,\mathrm{kg/m^3}$ (Hopcroft et al., 2010).

All cantilevers used for this work are coated with a 30 nm layer of aluminium at their back side for enhanced reflectivity. The small influence of this aluminium layer on the calibration was neglected.

The total stiffness of the system k_{total} is a series connection of the stiffness of the cantilever k, the tip stiffness k_{tip}, the substrate stiffness $k_{\mathrm{substrate}}$ and the contact stiffness k_{contact}, for both lateral and normal directions (subscript x and z):

$$\frac{1}{k_{\mathrm{total}}} = \frac{1}{k} + \frac{1}{k_{\mathrm{tip}}} + \frac{1}{k_{\mathrm{substrate}}} + \frac{1}{k_{\mathrm{contact}}}. \tag{3.15}$$

Here, k_{tip} and $k_{\mathrm{substrate}}$ represent the volume elasticity of tip and substrate, respectively. The contact stiffness k_{contact} is determined by the interaction potential, e.g. V_{surface} in Eq. (2.2) for lateral stiffness or V_{LJ} in Eq. (3.5) for normal stiffness. For conventional geometries and material combinations, such

Table 3.1: Typical parameters for AFM sensors 'PPP-LFMR' (*NanoWorld AG, Neuchâtel, Switzerland*)

parameter	typical value	range
width w (µm)	48	40-55
length L (µm)	225	215-235
thickness d (µm)	1	0.1-2.0
frequency f_0 (Hz)	23	1-57
normal stiffness k_z (N/m)*	0.2	0.11-0.24
lateral stiffness k_x (N/m)*	15	8-31

* for the particular sensors used in this work

as the Si cantilevers on HOPG or Si substrates used in this work, the tip and the substrate stiffness is usually much higher than the cantilever stiffness k, and thus can be safely neglected.

3.4.2 Normal Force Calibration

The normal stiffness of tip and sample in contact is usually much higher than the cantilever stiffness, $k_{\text{contact}} \gg k$, due to Pauli repulsion. In this case, Eq. (3.15) becomes $k_{z,\text{total}} \approx k_z$.

The normal sensitivity β_z can be determined from the linear slopes of force-distance curves (cf. Fig. 3.4a, in the region of $z < 0$):

$$\beta_z = \frac{\mathrm{d}z}{\mathrm{d}U_{T-B}}. \tag{3.16}$$

With the normal sensitivity β_z, and the previously calculated normal stiffness k_z, it is then possible to ascertain the absolute normal forces F_N from the measurement signal U_{T-B} according to Eq. (3.10) and Eq. (3.3).

3.4.3 Lateral Force Calibration: Enhanced Wedge Method

The simplification of Eq. (3.15), as used for the normal calibration, cannot in general be made for the lateral stiffness, since the contact stiffness of a tip on a flat substrate $k_{x,\text{contact}}$ can be of the order of the cantilever stiffness k_x. This becomes evident by the observation of atomic stick-slip movement with tip displacements of approximately one lattice constant as well as jump widths of about one lattice constant of silica tips on HOPG (Schirmeisen et al., 2005), which corresponds to the existence of only very few potential minima in the PT model (cf. Eq. (2.8) with $\xi > 1$, where ξ is of order 1).

To calibrate the lateral force signals without having to neglect $k_{x,\text{contact}}$, the method described by Varenberg et al. (2003) was used in this work. It represents an improved variant of the wedge calibration technique by Ogletree et al. (1996). The general idea is to push a sensor with a known force applied in normal direction onto a tilted surface with a well defined slope, resulting in easily computable force components normal and lateral to the tilted surface.

The calibration procedure, which also accounts for relative tilt between cantilever axis, scan axis and surface axis as well as undesired friction forces is performed by measuring force-distance curves and friction traces on the calibration grating 'TGF11' by *Mikromasch, NanoAndMore GmbH, Wetzlar, Germany*. This measurement is made along a path according to Fig. 3.6. The

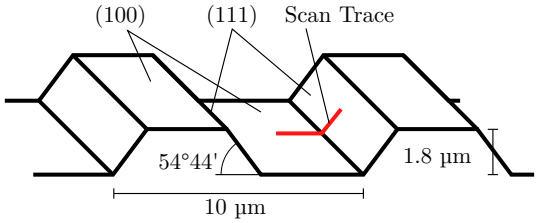

Figure 3.6: Topography of the lateral force calibration grating 'TGF11'. The defined slope of 54°44' allows for precise calculation of lateral forces resulting from the application of defined normal forces. For calibration measurements, the tip is scanned in both directions along the marked trace. Adapted from (Varenberg et al., 2003).

associated analysis procedure given in (Varenberg et al., 2003) directly yields θ_x, without the need to separately calculate k_x. Using this calibration method, absolute quantities of lateral and frictional forces can be determined. Varenberg et al. (2003) report typical uncertainties of 11 % for the value of θ_x.

3.4.4 Lateral Force Calibration: Static Friction Method

An alternative method for lateral force calibration was employed when no calibration sample was available. This method is based on exploiting static friction, and works in a similar way as the procedure used to calibrate the normal force (Sul et al., 2009; Munz, 2010). First, the contact stiffness $k_{x,\mathrm{contact}}$ can be significantly enhanced by placing the tip at the shoulder of a NP, thus allowing the simplification of Eq. (3.15) to $k_{x,\mathrm{total}} \approx k_x$. The remaining procedure then proceeds similar to the normal force calibration: The tip is pushed against the NP in x-direction, yielding a linear increase of force with

$$\beta_x = \frac{\mathrm{d}x}{\mathrm{d}U_{L-R}}. \tag{3.17}$$

This slope is marked by dashed lines in Fig. 3.5, at the beginning of each trace. Because the calculation of k_x depends quadratically on the tip height h_{tip} according to Eq. (3.13), this particular parameter was measured with a scanning electron microscope for each individual sensor that was calibrated using this static friction method.

A thorough overview over the numerous available lateral force calibration techniques is given by Munz (2010).

3.5 Instrumentation: AFM Systems

An AFM measurement system consists of a multitude of components. They can be grouped into three main subsystems, namely AFM head, housing, and controller system. The AFM head includes the sensor mechanics and force detection facilities. It is contained within a housing, which determines the surrounding conditions during the measurements, and usually includes sample preparation equipment. Additionally, a controller system is required to generate scan traces, record force signals, and to provide a feedback loop for the tip-sample distance regulation.

Three different AFM systems were employed for this work. The RT-UHV-AFM system (Section 3.5.3) allowed for the initial implementation of the NP manipulation procedure at room temperature. Measurements concerning the temperature dependence of nanoscale friction were performed with the VT-UHV-AFM system (Section 3.5.4). The combined UHV-AFM-SEM system (Section 3.5.5) was used for real-time visual feedback manipulation. All systems were operated under UHV conditions and each device was equipped with a force detection mechanism by means of the optical lever technique, as described in Section 3.1.

3.5.1 Ultra High Vacuum Setup

Since tribological experiments are very sensitive to interface contaminations, it is crucial to ensure very clean and well-defined environmental conditions during all experiments. The very cleanest conditions can be attained in ultra high vacuum (UHV) (pressure $p < 1 \times 10^{-7}$ mbar), which therefore was used for all experiments presented in this work.

The employed AFM heads were housed inside of evacuated stainless steel chambers, with base pressures of $p < 10^{-9}$ mbar. The vacuum was generated using a combination of different vacuum pumps: a turbo molecular pump in combination with a rotary vane pump was used to remove the bulk of atmospheric gas molecules from the chambers. Turbo molecular pumps operate by accelerating gas molecules towards the rotary pump, using a turbine made up of multiple stator and rotor stages, and produce pressures of below 10^{-8} mbar. Once this pressure is reached, other pumps with lower operating ranges in pressure and lower throughput can be activated. For this task, ion getter pumps were used in this work. These types of pumps operate by ionizing residual gas atoms, accelerating the ions by means of an electric field, and burying the ions into titan cathodes. Ion getter pumps were supplemented by titan sublimation

pumps, which sublimate titan into the chamber. The resulting titan surfaces at the chamber walls then can absorb residual gas atoms.

Pressure in the order of UHV can be measured using ionization gauges, in which a hot cathode filament emits electrons, which in turn ionize residual gas atoms. The number of ionized atoms is proportional to the gas density. Thus, the ion current can be measured to gauge the vacuum pressure (Chambers, 2005).

The UHV systems were periodically subjected to so-called *bake-out* procedures, in which the whole chamber assembly is heated above 120 °C for about 60 h using a heat tent, in order to desorb adsorbates from all surfaces of the system and thus regenerate the minimally attainable vacuum pressures.

3.5.2 AFM Controller System: GXSM

SPM experiments require a sophisticated real-time data processing system to generate the piezo voltages for scanning, to measure the force signals, and to regulate the tip-sample distance. The measurements presented in Sections 5.2 and 6.1 were performed using the GXSM scanning probe microscopy control system (Zahl et al., 2010). Apart from providing the experimentalist with a solid framework to perform standard measurement tasks, such as recording topography and friction maps or measuring normal force curves, the main advantage of using the GXSM control system for this work rested in the fact that it is licensed under an open source license (*GNU General Public License Version 3*), and thus grants the licensee access to the source code. In particular, the access to the source code allowed the author of this work to implement custom routines which aided in the automation of the NP manipulation process (Section 4.3) and the slide-hold-slide experiments (Section 6.1.1). These modifications allowed to streamline the manipulation process, enabling to gather a sufficient amount data for statistically significant evaluation within reasonable time frames.

In particular, the following modifications were implemented: An interactive tip placement mode was devised, allowing to gather topographic images, and subsequently place the AFM tip at a specific site by mouse click selection within the image, e.g. at the center of a nanoparticle. During the tip translation, all relevant measurement data were logged to a database. A specialized routine was implemented to automatically record arrays of friction loops, allowing reproducible tip translations along predefined pathways over a range of velocities (cf. Section 5.2.1). For the slide-hold-slide experiment, a custom routine was implemented, which allowed to select a range of hold times and velocities as

well as the number of repetitions to be performed. Hence, dozens of full SHS friction loops could be initiated with a single command.

3.5.3 RT-UHV-AFM System

Initial experiments were performed with an UHV-AFM system operated at room temperature (RT), located at the Physical Institute of the University of Münster, Germany. In Fig. 3.7 a photo of the setup is shown, whereas Fig. 3.8 provides an overview of the sample stage. The AFM head was supplied by *Omicron NanoTechnology GmbH, Taunusstein, Germany*. Since this system was available for exclusive use in NP manipulation experiments, it allowed to establish and refine the overall manipulation procedure without disruption by other experiments.

All force calibrations for this system were carried out according to the 'enhanced wedge calibration' method described in Section 3.4.3. The piezo displacement of the system was calibrated using HOPG.

3.5.4 VT-UHV-AFM System

Experiments regarding the temperature dependence of nanoscale friction were conducted using a variable temperature (VT) UHV-AFM at the *Center for Nanotechnology, CeNTech GmbH* in Münster, Germany. This microscope features a sample stage which can be cooled down to temperatures of T=30 K or heated to T=1000 K. The cooling is achieved by an integrated flow cryostat, in which liquid nitrogen or liquid helium is evaporated at the respective boiling temperatures of 77 K and 4 K. A counter heater connected to a temperature-controller in combination with thermocouple sensors allows to stabilize the temperature at any intermediate value.

The UHV housing of the system is depicted in Fig. 3.9. The preparation chamber was supplied by the manufacturer of the AFM head, *Omicron NanoTechnology GmbH, Taunusstein, Germany*, and is supplemented by a home-build analysis chamber. Both chambers can be separated by a valve to minimize contamination during preparatory work. The analysis chamber rests on a separate foundation of concrete, decoupled from the rest of the building. A detailed vacuum diagram of the microscope system can be found in (Weiner, 2007).

Fig. 3.10 shows a sketch of the VT head assembly. Samples are placed into the rigid sample stage with their surface facing down. The back side of the sample holder is then clamped onto a cooling block, which is connected to

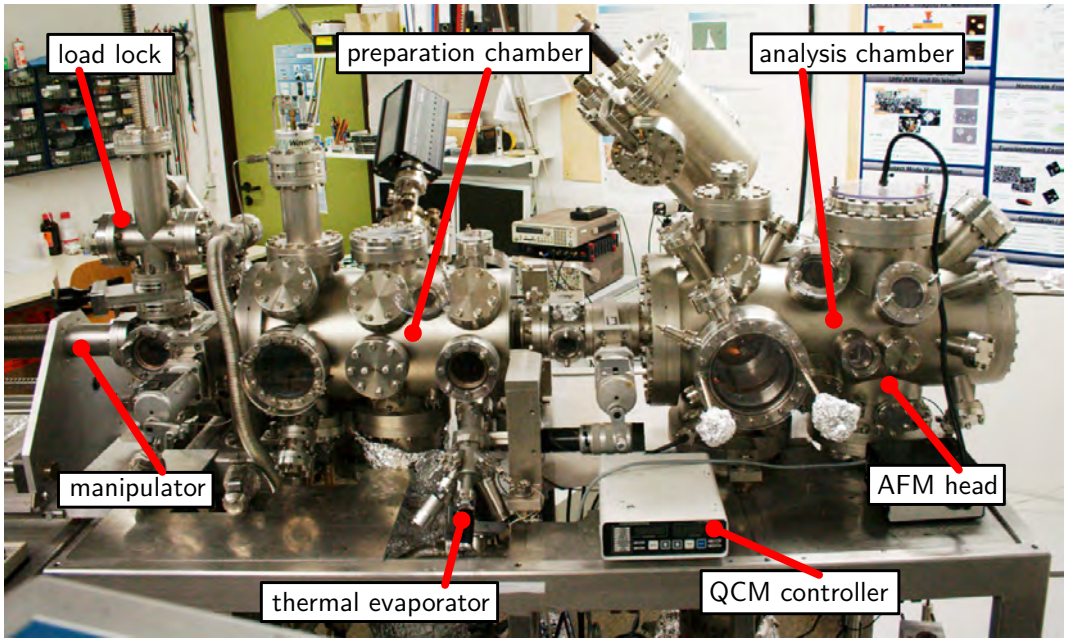

Figure 3.7: Photograph of the RT-UHV-AFM. The system includes a preparation chamber with a thermal evaporator and an analysis chamber, housing the AFM head.

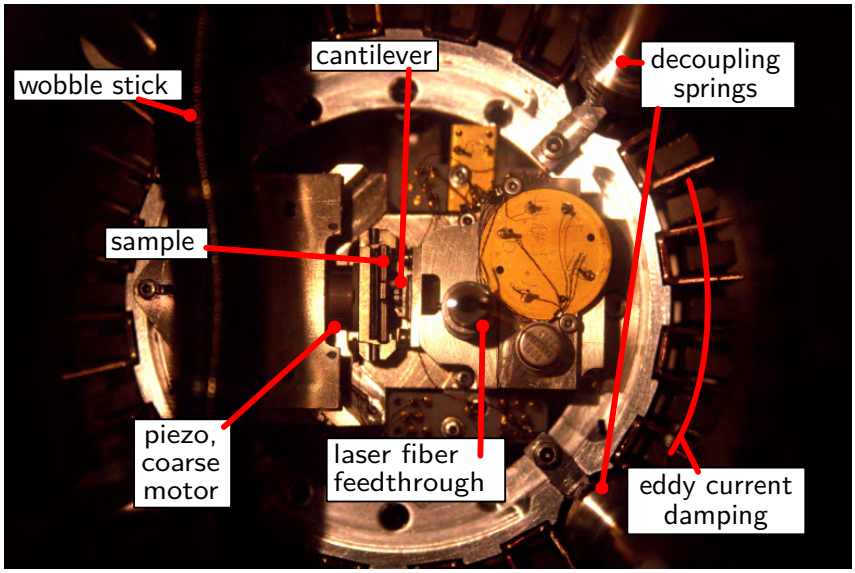

Figure 3.8: Photograph of the RT-UHV-AFM head, as seen from above. The head is decoupled from the surrounding by four soft springs, and damped by an eddy current damping system.

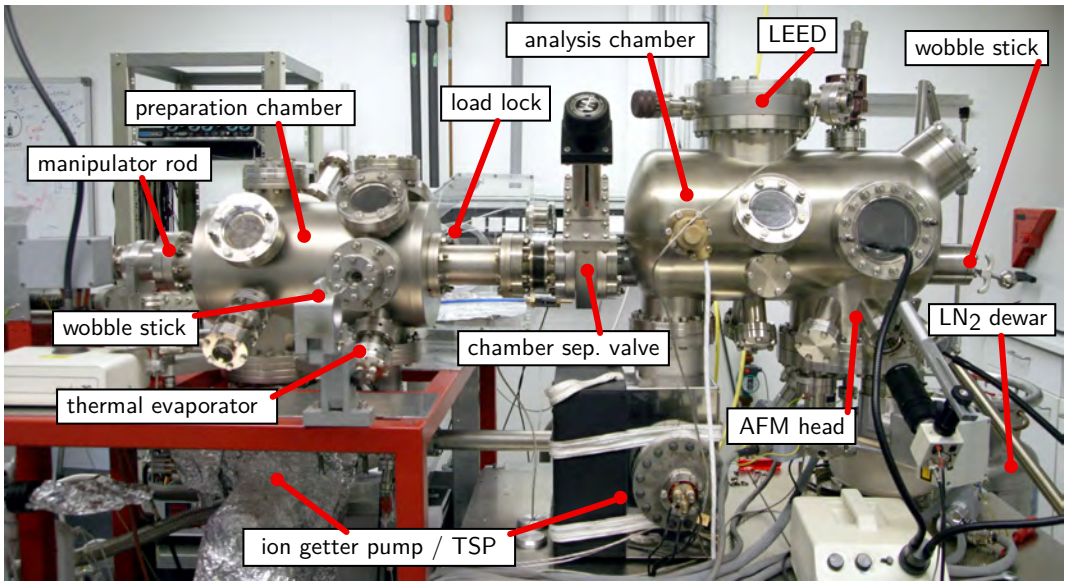

Figure 3.9: Photograph of the VT-UHV-AFM system. Antimony evaporation and sample heating was performed in the preparation chamber on the left, while all measurements were conducted inside the analysis chamber.

the flow cryostat through a copper braid. Sample heating can be achieved by passing a current through a heating filament in the sample holder, or by passing current directly through a conducting sample substrate. In addition, a heating element located at the flow cryostat serves as a counter-heating element. Both sample stage and the cooling point at the flow cryostat are equipped with thermocouples, whose reading is used as the process variable for a PID controller to stabilize the temperature at a previously chosen value. This is achieved with the counter-heater at the flow cryostat, and allows to set the temperature with an accuracy of 0.1 K at the thermocouples. The lowest attainable temperature at the sample is 30 K when using helium as the coolant, and 100 K when nitrogen is used.

Since with the VT-UHV-AFM it is not possible to readjust the PSD in lateral direction (cf. Fig. 3.10a), the cantilever had to be aligned very precisely during the sensor preparation in order to gain high lateral force sensitivity and stay within the linear range of the lateral force detection system. This process involved venting the analysis chamber and gluing the cantilever chips onto the tip holder, while the tip holder was placed *in situ* on top of the piezo scanner. The laser was subsequently adjusted onto the cantilever and the cantilever chip was pushed against a hollow sample holder by performing coarse steps with the

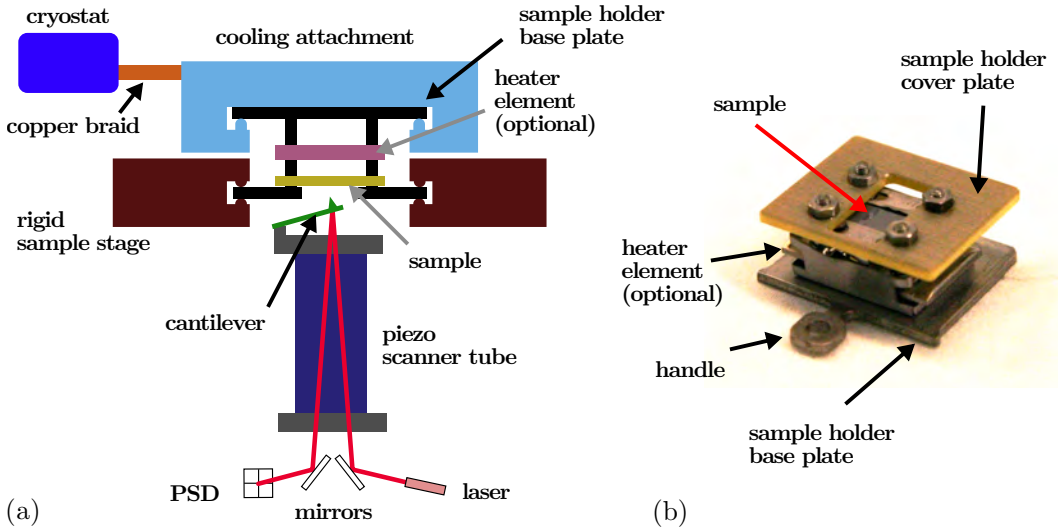

Figure 3.10: VT-UHV-AFM head. (a) Schematic of the AFM head assembly. The sample is inserted into the rigid sample stage, with the surface facing downwards. A cooling attachment gets subsequently clamped onto the back side of the sample holder, which is connected by a copper braid to the flow cryostat. The piezo tube with the sensor and optical lever force detection system can then be approached from below towards the sample. The mirrors can only be rotated in the image plane. Figure adapted from information provided by *Omicron NanoTechnology GmbH, Taunusstein, Germany*. (b) Annotated photograph of the sample holder assembly. The sample is mounted between the cover plate and steel sheet springs. The sample holder is inserted into the AFM head with the sample facing down towards the sensor.

piezo scanner. This procedure allowed to precisely alter the cantilever angle until the lateral force signal was adjusted to zero.

The spacial calibration of this microscope was attained by recording HOPG friction force maps with atomic resolution as show in Fig. 4.10c.

3.5.5 Combined AFM-SEM System

To execute NP manipulations with real-time feedback regarding the relative positioning of sensor and NP, a microscopy system with capabilities for simultaneous AFM and scanning electron microscope (SEM) measurements was used.

The basic rationale of SEM operation can be given as follows (Lüth, 2010): An electron beam is generated inside an electron column by using a cathode

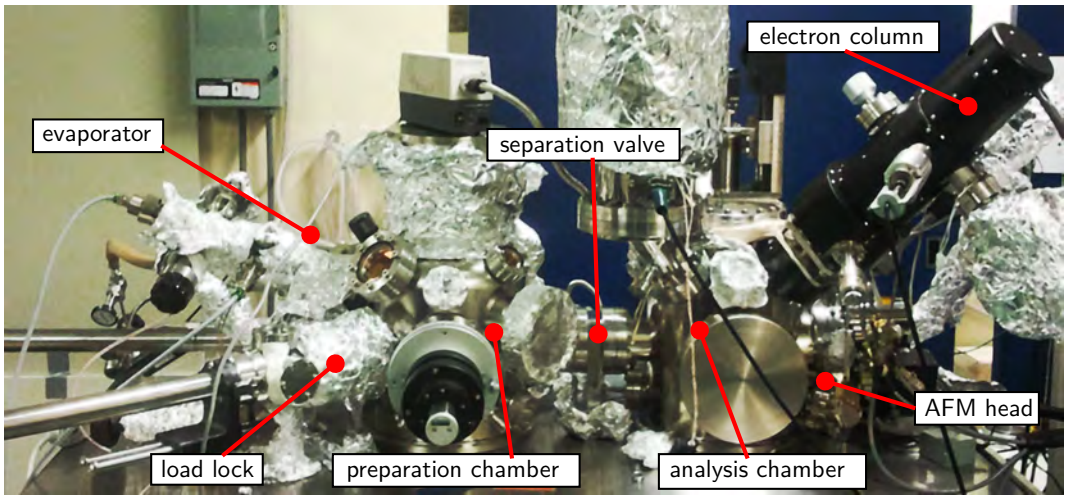

Figure 3.11: Photograph of the UHV-AFM-SEM system. The electron column is focused on the AFM sample stage, at 45° inclination.

to emit electrons, along with electron lenses and electric acceleration fields to focus the beam. This beam is directed at a target sample inside a vacuum chamber, and scanned along grid coordinates across the region of interest. Primary electrons are scattered by the sample, resulting in the emission of secondary electrons. The latter can be extracted using an electric field, and are measured using an electron detector. Primary back-scatter electrons can also provide a viable observation channel, although in that case a different detector is required. An image contrast is generated by the distinct secondary electron yield of different materials, such as antimony and graphite, and by shading effects. Due to the short wavelength of the electrons compared to photons of visible light, an SEM allows to image samples with resolutions well below the diffraction limit of optical microscopes. A more thorough description can be found in the literature, e.g. in (Lüth, 2010).

The JEOL JSPM-4500A AFM system (*JEOL Ltd., Akishima, Japan*), located at the McGill University in Montreal, Canada, features an AFM stage in combination with a SEM electron column and secondary electron detector. The components are arranged within an UHV analysis chamber so that AFM and SEM measurements can be performed simultaneously. The angle between electron column and sample amounts to 45°, thus allowing the monitoring of both the sample and the AFM tip. Live SEM images could be recorded with a frequency of up to 15 Hz. Figure 3.12 shows a sensor within this system in front of a Sb/HOPG sample, at increasing levels of magnification. The system

was operated at room temperature during all measurements.

In addition, the system comprises an UHV preparation chamber with both electron-beam and thermal evaporators, a quartz crystal microbalance and a pyrometer, which enabled the preparation of nanoparticle samples and a transfer to the AFM stage without exposure to ambient conditions (cf. Fig. 3.11).

To facilitate nanoparticle manipulation experiments, a custom LabVIEW instrument (*National Instruments Corp., Austin, TX, USA* , NI PCI-6036E board) was designed to generate the necessary translation vectors for the piezo drives as well as to record the corresponding force signals with high temporal resolution, at a sampling frequency of $f_{\text{sampling}} = 10\,\text{kHz}$. Furthermore, free movement of the AFM tip in x and y direction using the mouse was made available.

The spacial calibration of the AFM instrument was adapted from earlier experiments (Tekiel et al., 2012), while the calibration of the SEM was inferred from the AFM calibration. The lateral force calibration at this system was carried out using the 'static friction calibration' method introduced in Section 3.4.4. To calculate the spring constants with high accuracy, the sensor geometry was determined through SEM imaging.

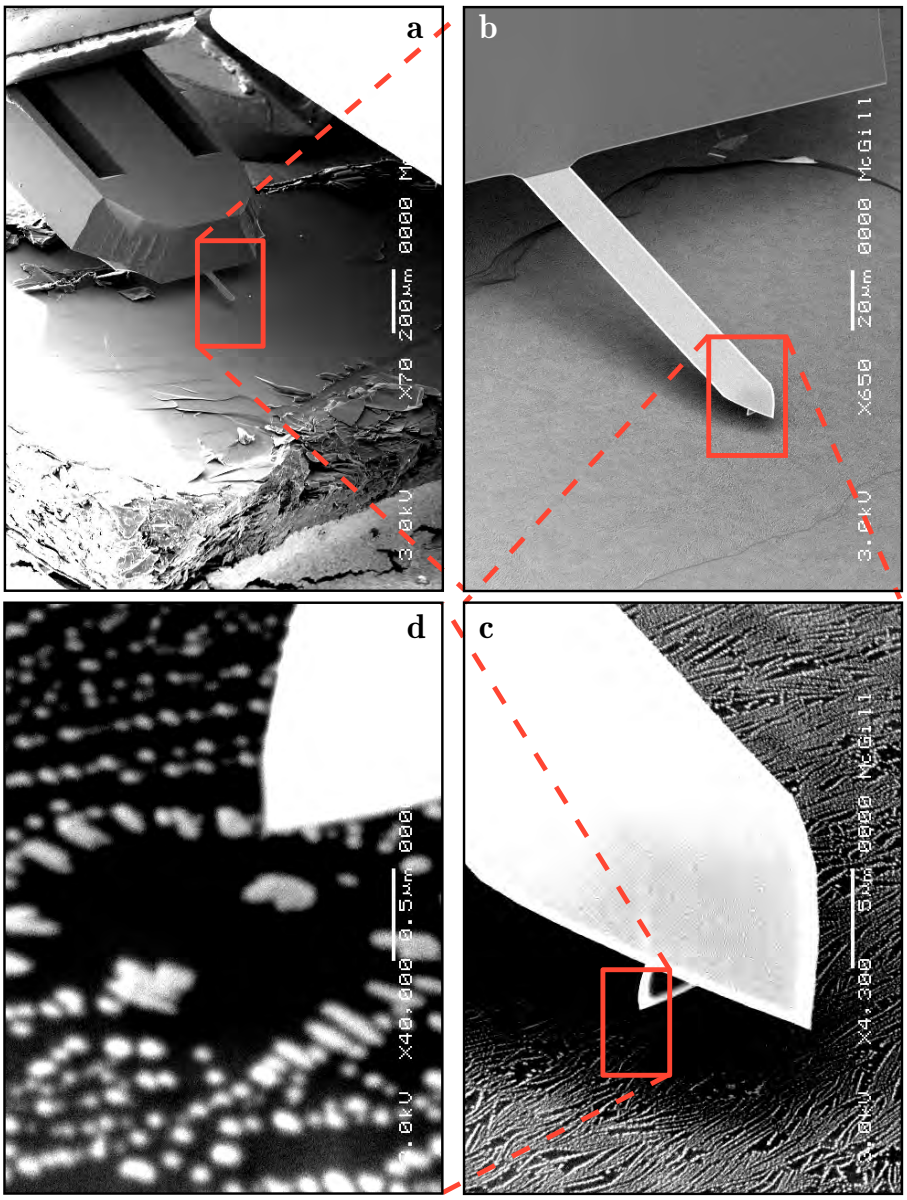

Figure 3.12: Combined AFM-SEM: AFM cantilever over an Sb/HOPG sample as recorded by the SEM at increasing magnification. (a) At minimal magnification of ×70 the cantilever chip (upper left) with the attached cantilever (center) can be recognized. In the lower right, a cut edge of the HOPG substrate with flake-like detachments can be seen. (b) With a magnification of ×650 the cantilever can be imaged. Large defects on the substrate are visible. (c) At ×4,300 magnification elongated structures on the substrate are revealed, corresponding to Sb-decorated step edges. (d) The maximum magnification of ×40,000 allows to identify single nanoparticles near the apex of the AFM tip.

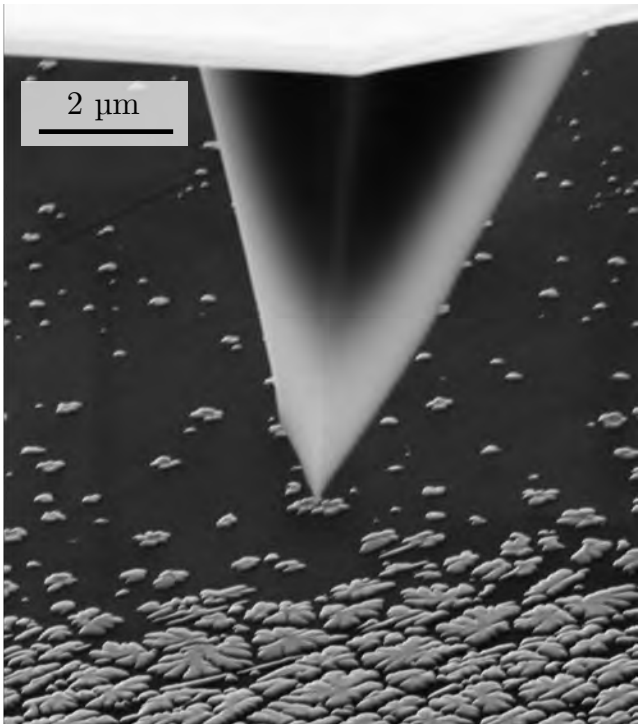

Figure 4.1: SEM micrograph of an AFM tip above a sample consisting of antimony particles on a HOPG substrate.

4 Nanoparticle Manipulation

The application of nanoparticle (NP) manipulation in friction experiments provides a unique technique to probe frictional qualities of extended single asperity contacts. In this chapter, the general principle of NP manipulation using an FFM is introduced, and different methods capable of extracting quantitative information from these measurements are detailed.

In general, all NP manipulation experiments consisted of a three-fold sequence: First, the sample topography containing the particle was imaged without manipulating the sample. In a second step, the particle was translated while the friction was recorded. In a final step the success of the manipulation was assessed by again recording the topography.

Topographic imaging of the samples was conducted in NC mode, as laid out in Section 4.1. The individual particle manipulations were performed either using the tip-on-side (TOS) mode or in the tip-on-top (TOT) mode, which are

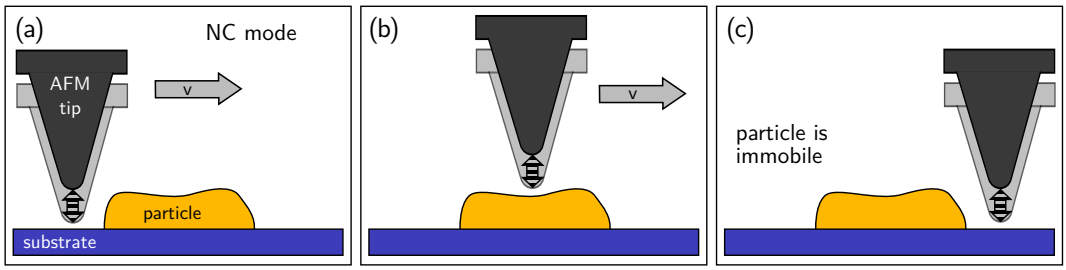

Figure 4.2: Schematic of a topography scan in NC mode. The tip traces the surface topography while exerting low interaction forces below the manipulation threshold of the particle. By recording multiple traces, which are offset in normal direction to the image plane shown here, a full topography scan can be acquired.

described in detail in Sections 4.2 and 4.3. The NP model system used in this work consisted of Sb particles on HOPG substrates. Selected properties of this sample system, as well as its preparation, are introduced in Section 4.6.

Before performing any measurements, a new cantilever was first inserted into the AFM, and the laser beam path was adjusted to pass the back side of the cantilever directly above the tip, and end at the center of the PSD. The normal resonant frequency f_0 was measured and NC mode operation using the PLL detector was initialized. Afterwards, samples were prepared as described in Section 4.6.4, and subsequently placed into the sample stage of the AFM. Finally, the tip was approached to the surface to begin with the sample characterization.

4.1 Topography Scan of NP-decorated Samples

The first step in characterizing the sample is to acquire topography scans of the sample surface. Since the NPs are only weakly bound to the substrate, special care has to be taken in order to probe the surface without modification. This was achieved by reducing the lateral forces acting on particles.

An initial approach to minimize lateral forces is to scan the surface in contact (CT) mode with the minimal stable normal force set point F_N^{SP}. For particles with high static friction it is preferable to perform topography scans in CT mode, due to the low complexity of this method, as demonstrated by Dietzel et al. (2007). But if the particles exhibit very low static friction, the use of CT mode for imaging becomes completely unfeasible due to inadvertent NP manipulation.

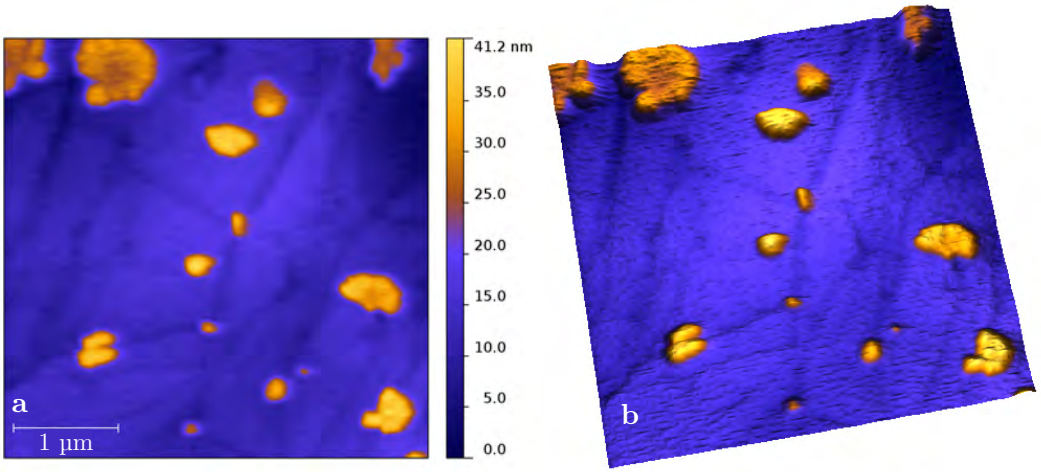

Figure 4.3: Typical topography scan of a Sb/HOPG sample surface in NC mode. Visualization as a (a) 2D and (b) 3D rendering. In the latter, the z-scaling is enhanced by a factor of 10, and the image slightly tilted. The Sb NPs are clearly identifiable as protrusions colored in yellow. The HOPG substrate, colored in blue, is intersected by dark-colored line segments, which correspond to step edges of atomic layers.

A more delicate method to produce topography scans was implemented by employing NC mode. As described in Section 3.2.2, snap-on hysteresis effects can be avoided in NC mode through oscillations of the cantilever. The normal tip-sample interaction in this mode can be significantly reduced in comparison to what is attainable in CT mode scans. Additionally, virtually no friction between tip and particle arises in this mode, since the contact is completely detached at each oscillation cycle. Figure 4.2 shows the outline of the acquisition of a topography scan line in NC mode. By acquiring a number of these scan lines with a small parallel displacement, it is possible to generate a 2D representation of the surface topography. Figure 4.3 represents an example of a typical sample topography.

For topography measurements the frequency shift Δf is chosen near the lower detection limit, in the order of 10 Hz. Higher values of Δf can lead to tip-sample interaction, which is sufficiently high to induce surface modifications even in NC mode (Vlassov et al., 2011). But the extraction of lateral forces from measurements in dynamic AFM modes is rather intricate, in particular for kinetic friction (cf. Section 4.4). Different methods used to manipulate NPs with an AFM in CT mode, which are more suitable for quantitative force measurements, will be described hereafter.

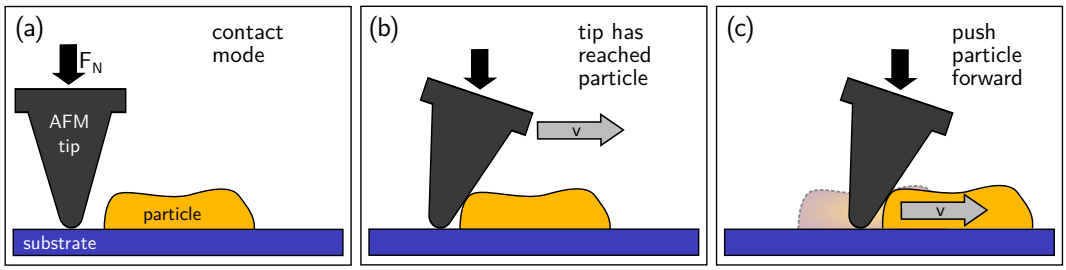

Figure 4.4: Sketch of the tip-on-side (TOS) manipulation mode. (a) After the particle is located, the tip is placed besides the particle in contact mode. (b) The tip is approached towards the particle, while the particle is still fixed. The torsion of the cantilever gradually increases, until the static friction is overcome. (c) Particle manipulation is achieved. The cantilever torsion is proportional to the kinetic friction.

4.2 Tip-On-Side Mode of NP Manipulation

The tip of an AFM can be used to exert forces onto the surface which are sufficient to induce surface modifications. In particular, the tip can be utilized to push NPs across a flat substrate, while at the same time the acting forces can be measured. The tip-on-side (TOS) mode of NP manipulation is the most basic and intuitive manipulation mode, as described in the following.

First, the tip is placed besides a particle and brought in contact with the substrate by switching to CT mode. Subsequently, the tip is approached towards the NP (see Fig. 4.4), where it comes into contact with the NP. Opposing lateral forces act on tip and NP, which increase linearly as the cantilever support is moved further. If the static friction threshold is sufficiently low, the lateral force exerted by the tip will eventually overcome the static friction of the particle, and the particle will start to move in union with the tip. Figure 4.5 shows an example of a particle manipulation carried out in TOS mode. Increasing the normal force set point F_N^{SP} in general also increases the maximally exertable lateral force onto the particles, because normal and lateral force are coupled through the sloped contact of tip and particle (cf. Fig. 4.8b).

Since the tip trajectory often does not intersect with the center of mass of the particle, pushing particles in TOS mode can be unstable: As demonstrated by Dietzel et al. (2010b), NPs are prone to move to either side of the tip trajectory, and can even loose contact with the tip. In practice, this instability is often limited, if the adhesion between tip and NP ensures a sufficiently stiff contact. Even pulling of a particle is feasible if the particle friction is low compared to the tip-particle adhesion.

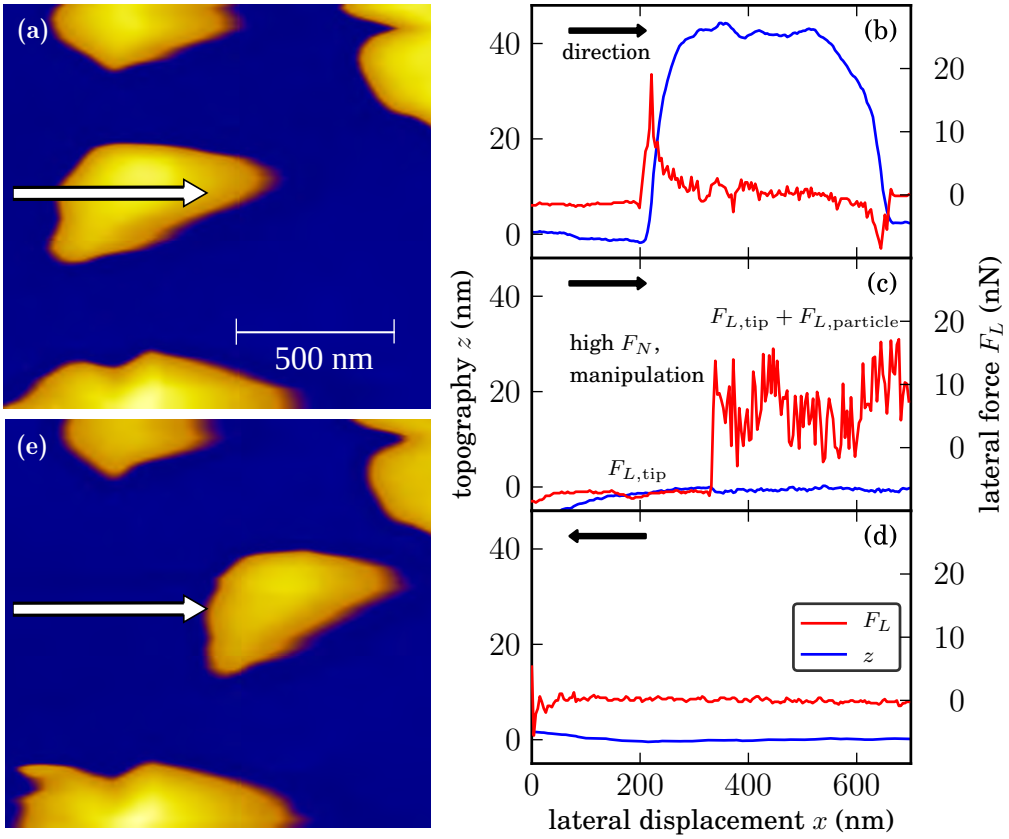

Figure 4.5: Example of a tip-on-side (TOS) NP manipulation in contact mode. The CT mode topography scans in (a) and (e) show the particle before and after successful manipulation, respectively, while (b-d) depict topography and lateral force traces along the vector marked with a white arrow in (a) and (e). (b) shows a line trace recorded at low normal force. The particle topography is observed. In (c), the normal force F_N was increased and the tip was translated from $x = 0\,\mathrm{nm}$ in $+x$ direction. During the whole trace the topography signal is approximately constant, while the lateral force signal increases significantly, which indicates a successful manipulation of the particle. The edge of the particle is slightly displaced when compared to (b) due to increased sensor tilt at higher normal load, and due to piezo hysteresis and creep. It has to be pointed out that the value of $F_{L,\mathrm{tip}}$ on the substrate has changed due to increased F_N, which needs to be corrected in the analysis. For the trace shown in (d) the tip was moved back in $-x$ direction without the particle.

While the TOS mode already enables fully operational NP manipulation with simultaneous lateral force detection, it allows only one particle translation at a time, which caps the usefulness of this mode considerably. The tip has to be manually repositioned in order to push the particle back to its original position; a rather tedious procedure, especially if a whole range of parameters is to be probed, e.g. the velocity dependence of friction. The TOT mode, described in Section 4.3, improves significantly in this respect by enabling many successive manipulations of a single particle without manual intervention. The TOS mode, on the other hand, can be useful if many particles are to be manipulated only once: It can be used in a stochastic variant, where full image scan frames are recorded in TOS mode. The normal force set point F_N^{SP} is set to a value slightly above the manipulation threshold, allowing to manipulate many particles within a single scan frame with stochastic manipulation probability, and without manual intervention (Dietzel et al., 2007). Controlled and repeated manipulations of a single particle are not possible with this technique, and thus this stochastic manipulation mode was not used in this work.

In TOS mode, the measured lateral force at the tip F_L includes contributions from both the lateral force of the nanoparticle $F_{L,\mathrm{particle}}$ and from the tip $F_{L,\mathrm{tip}}$ as given in

$$F_L = F_{L,\mathrm{tip}} + F_{L,\mathrm{particle}}. \tag{4.1}$$

Hence, reference measurements of $F_{L,\mathrm{tip}}$ have do be carried out in order to separate these two quantities.

When using the TOS mode, the lateral force of the particle $F_{L,\mathrm{particle}}$ can be determined in two ways: First, by recording friction loops (cf. Section 3.3) with and without the particle, and then applying Eq. (4.1), or, second, by recording friction traces containing both F_L (with particle) and $F_{L,\mathrm{tip}}$ (without particle). In the latter case, Eq. (4.1) allows to directly calculate $F_{L,\mathrm{particle}}$ without having to record a full friction loop. An example of a TOS manipulation using this type of referencing is displayed in Fig. 4.5.

The employment of the general imaging-manipulation-imaging sequence required a facility to switch arbitrarily between CT mode and NC mode operation. In this work, the switching was implemented as a mechanical dual-switch. This switch allowed to either route the normal deflection signal U_{T-B} or the frequency shift Δf to the feedback signal input of the tip-sample distance regulator, and it enabled to make or break the connection from the oscillation excitation circuitry to the shaker piezo. This setup enabled the microscope operator to change between CT mode and NC mode simply by operating the switch.

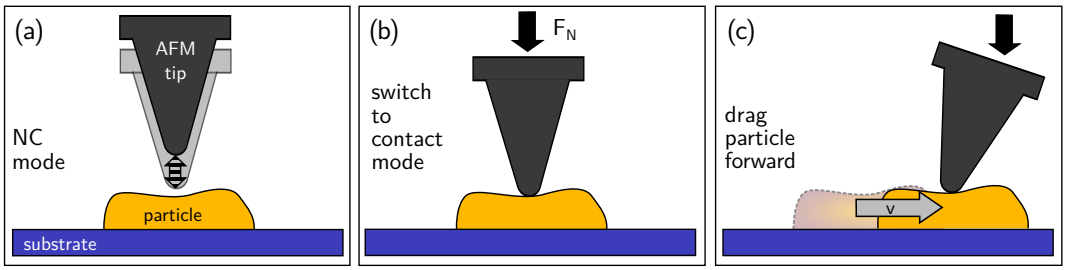

Figure 4.6: Schematic of the tip-on-top (TOT) manipulation mode. (a) The tip scans the topography to locate the particle and is then placed on top of the particle. (b) The tip-particle interaction is enhanced by switching to high-F_N contact mode operation. (c) The particle is manipulated through dragging with the tip.

4.3 Tip-On-Top Mode of NP Manipulation

In contrast to the TOS mode, the tip-on-top (TOT) manipulation mode allows to perform many consecutive manipulations without having to tediously readjust the tip. This property made the TOT mode to the method of choice for repeated friction measurements of individual particles. Furthermore, it served as the basis for more complex measurement protocols, as presented in Sections 5.1 and 5.2.

In TOT mode, the AFM tip is first placed on top of the particle near its center, as sketched in Fig. 4.6. The positioning of the tip above the particle (Fig. 4.6a) is performed in NC mode (or in CT mode at low normal force F_N) as to not prematurely push the nanoparticle away. The feedback switch is then set to operate in CT mode, and a comparatively high normal force set point F_N^{SP} is selected (typically $F_N^{\mathrm{SP}} \approx 30\,\mathrm{nN}$ for the employed Sb/HOPG sample system). If the static friction between tip and particle exceeds the static friction threshold between sample and substrate,

$$F_S^{(\mathrm{tip,particle})} > F_S^{(\mathrm{particle,substrate})}, \tag{4.2}$$

then the tip is able to initiate sliding of the particle (Fig. 4.6c).

An important factor contributing to the feasibility of the TOT mode is the different contact geometry of the two involved contacts. The contact between particle and substrate is extremely flat, and the associated friction does not change significantly when the load is increased (Dietzel et al., 2009). The contact between tip and particle, on the other hand, can be approximated as a contact between an elastic sphere and a flat surface (Bhushan, 2004). According to Hertzian contact mechanics, the contact area $A^{(\mathrm{tip,particle})}$ increases with the

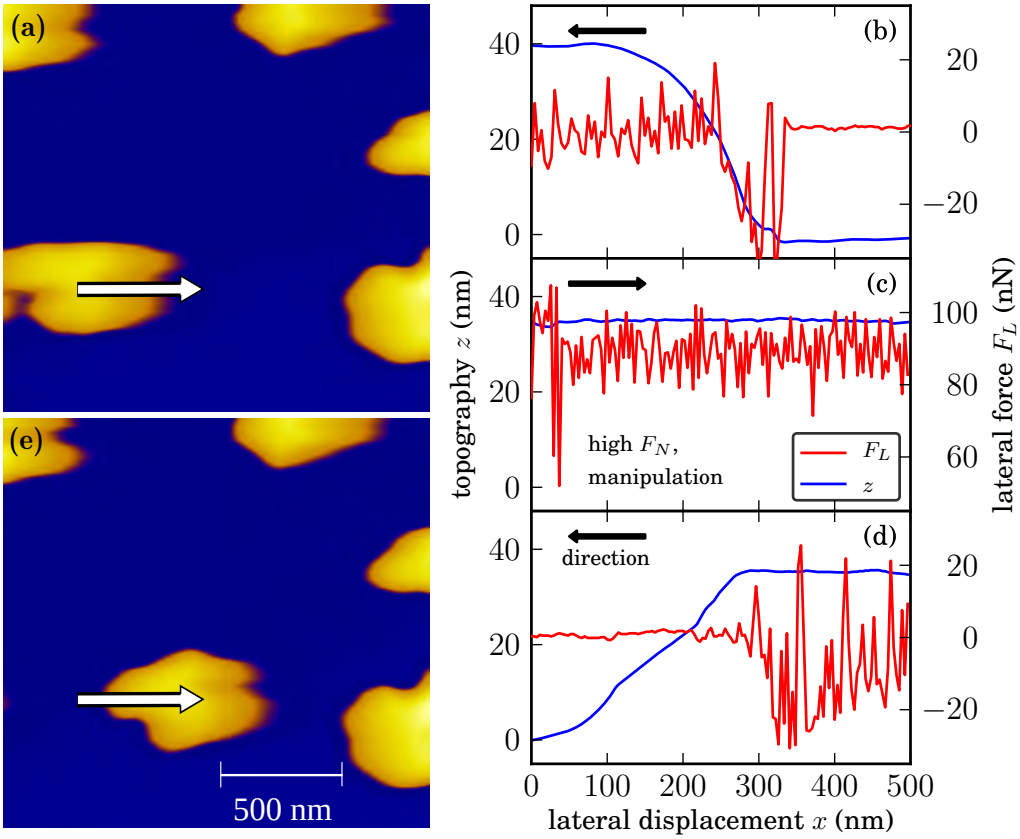

Figure 4.7: Example of a tip-on-top (TOT) NP manipulation in contact mode. The topography scans in (a) and (e) show the particle before and after successful manipulation, respectively, while (b-d) depict topography and lateral force traces recorded along the vector marked with a white arrow in (a) and (e). (b) shows the line trace, in which the tip was moved from the substrate level at $x = 500\,\text{nm}$ onto the particle ($x = 0\,\text{nm}$) without moving the particle. In (c) the normal force was increased and the particle was manipulated in $+x$ direction, discernible by the constant topography signal. For (d) the normal force was again reduced and the tip moved down from the particle.

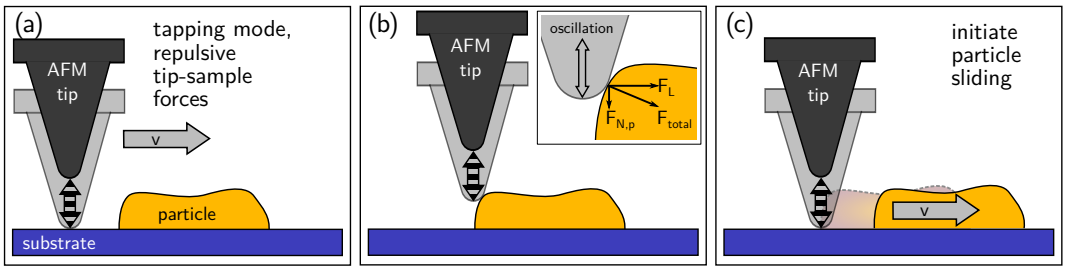

Figure 4.8: Illustration of dynamic surface modification mode. (a) The tip interacts with the substrate surface in tapping mode. (b) When the tip reaches the shoulder of a particle, the tip oscillation results in interaction forces F_{total}, normal to the tip-particle interface. This force has a component parallel to the substrate surface, F_L. (c) If F_L is larger than the static friction force F_S the particle will start to move.

normal force F_N as in (Bhushan, 2004)

$$A^{(\text{tip,particle})} \propto {F_N}^{2/3}. \tag{4.3}$$

Since friction increases with the contact area (see Section 2.4) it follows that $F_S^{(\text{tip,particle})}$ increases with normal force F_N, while $F_S^{(\text{particle,substrate})}$ is constant in F_N. Hence, it becomes possible to tune the fulfillment of Eq. (4.2) by adjusting F_N, thus selectively rendering the particle mobile or immobile relative to the substrate.

Figure 4.7 shows exemplary force traces and topography images of a TOT manipulation. In this particular case, the topography was scanned in contact mode with low normal force F_N. The tip was then placed above the center of the particle. F_N was successively increased, so that Eq. (4.2) was fulfilled. The particle was subsequently dragged in $+x$ direction, after which the normal force was again reduced, and the tip was moved down from the particle in $-x$ direction. Topography images in Fig. 4.7a,e were recorded prior and after this sequence in order to verify the successful manipulation. For the extraction of quantitative friction force data F_F, it is necessary to perform a full friction loop in $+x$ and $-x$ direction (not shown in Fig. 4.7) according to the measurement protocol in Section 3.3.

4.4 Dynamic Surface Modification Method

Another viable method used to manipulate NPs with an AFM is provided by the dynamic surface modification (DSM) mode, which utilizes *tapping mode*

AFM operation. In tapping mode, the cantilever is excited near its resonance frequency, and the oscillation amplitude is used as the feedback signal to control tip-sample separation. This mode differs significantly from NC mode, which uses the frequency shift Δf as the feedback signal, and allows for much smaller tip-surface interaction. In tapping mode, the tip enters the repulsive regime of the tip-sample interaction in every oscillation cycle, and the system is damped by significant energy transfer from the tip into the surface.

In DSM mode, the NP is manipulated by tapping at the edge of the particle, thus generating a force component parallel to the surface (see Fig. 4.8). This mode was introduced by Ritter et al. (2002) and has been used to measure the power dissipation when moving Sb particles on HOPG substrates (Ritter et al., 2005). Rovatti et al. (2010) presented a variation of this technique which uses amplitude modulation NC mode to manipulate Au clusters on HOPG.

The main benefit of using DSM mode for NP manipulation lies in the fact that it is relatively easy to implement compared to more sophisticated approaches such as TOT mode. In addition, it does not require the AFM instrument to have a dedicated lateral deflection measurement channel.

The ballistic nature of the manipulation process limits the utility of the DSM mode for friction measurement experiments, since only the energy initially implanted into the particle can be measured, and not the time-evolving forces. Specifically, the influence of the translation velocity cannot be determined in a straightforward manner, a quantity which in Section 5.2 is found to have a significant influence on nanoscale friction. Additionally, tapping mode is in general not well-suited for UHV conditions, since the high quality factor of the cantilever in vacuum limits the responsiveness of the amplitude signal to changes in the interaction. As a consequence, DSM mode was not used in this work.

4.5 Real-Time NP Manipulation Monitoring using SEM

Nanoparticle manipulation systems equipped with just a single AFM probe are limited to either imaging of a particle, or manipulating it. Performing both at the same time is not feasible with a single probe. Hence, the previously described methods used a sequence of first imaging the particle, followed by a translation of the NP, and concluded by a final imaging step. If a way of monitoring the particle during manipulation is required, further observation

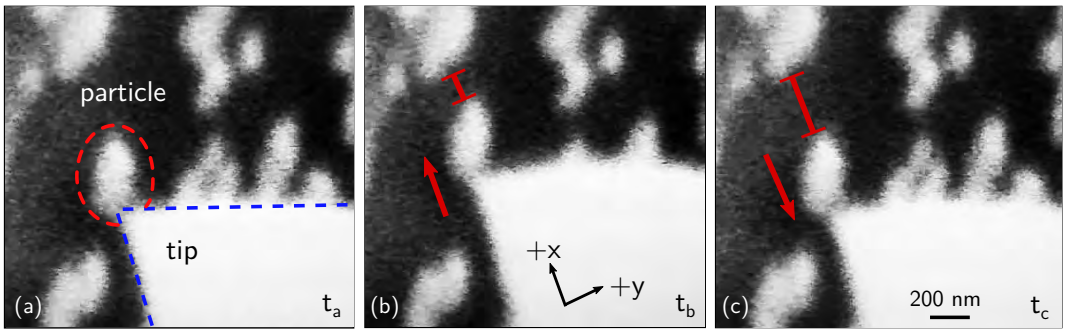

Figure 4.9: Example of a NP manipulation using real-time SEM monitoring in TOS mode. The three images shown are frames of a live video capture which was recorded during the whole experiment, at the times $t_a < t_b < t_c$. Between the recording of (a) and (b) the particle was moved in $+x$ direction, and between (b) and (c) it was translated in $-x$ direction, each time by about 200 nm. The latter manipulation is an example of lateral particle pulling through adhesive tip-particle forces, in contrast to pushing of the particle in the first manipulation.

channels have to be implemented.

One very convenient way of achieving real-time monitoring is given by using a microscope with a combined AFM and scanning electron microscope (SEM) stage. For this work, a combined AFM-SEM was adapted to allow real-time NP manipulation monitoring (see Section 3.5.5). To the authors knowledge, this was the first instance of NP manipulation implemented with a combined AFM-SEM, where the use of the light beam force detection scheme allowed to directly record lateral forces. Previous works by Vlassov et al. (2011) have demonstrated NP manipulation within an AFM-SEM system using a tuning fork sensor. This sensor can only be used in a dynamic mode, similar to DSM, which does not allow for continuous and smooth pushing of NPs at a constant velocity. Furthermore, the Au NPs used in their work were prepared *ex situ*, while all Sb NP sample preparations presented in this work were carried out *in situ* in order to attain very clean interfaces.

In Fig. 4.9 an exemplary manipulation sequence of a single particle is shown. The tip is first placed at the side of a particle, and is then translated to push the particle in the $+x$ direction. Subsequently, the tip is moved back to its original position, while the particle follows the same trajectory due to adhesion between tip and particle, thus implementing a variant of the TOS manipulation mode. The forward-backward translation yields a full friction loop; images represent single frames of a continuously recorded video. Since the resulting friction

signals are elicited by both the friction between nanoparticle and substrate as well as the friction between tip and substrate, reference measurements of the tip-substrate friction might become necessary (cf. Section 5.3).

The pulling of an NP with the tip in this example already demonstrates the advantages of real-time SEM monitoring, as it directly proves the feasibility of adhesion-supported NP pulling experiments. More obvious benefits are the ease of the overall system operation. Large areas on the sample can quickly be surveyed for particle-substrate configurations of interest, e.g. selecting particles by their size and morphology, or by their relative spacial positioning with respect to other particles or substrate defects such as step edges. During a manipulation attempt, immediate feedback regarding the success of the individual manipulation is available. In contrast, the previously described operation of AFM in NC mode can be rather difficult to operate, due to oscillation instabilities and varying levels of tip-surface interaction.

A video of the images acquired by the SEM was recorded during all manipulations at this system. This video, in combination with the acquired force signals, allows to fully reconstruct a manipulation session later during evaluation of the measurement, which simplifies the data analysis considerably.

4.6 Experimental Model System: Sb Particles on HOPG

In order to implement atomically smooth extended single asperity nanocontacts for friction measurements, a sample system consisting of antimony (Sb) particles on highly orientated pyrolytic graphite (HOPG) was adopted for this work. In a number of experiments, different aspects of this model system have previously been investigated (Kaiser et al., 1999a; Stegemann, 2003; Stegemann et al., 2004b; Ritter et al., 2005; Ritter, 2005; Dietzel et al., 2007; Brndiar et al., 2011a; Brndiar et al., 2011b), which allows to compare new measurement results with previous findings.

4.6.1 Highly Orientated Pyrolytic Graphite

Highly orientated pyrolytic graphite (HOPG) is very well suited for nanoscale friction experiments, since it exposes atomically flat and very inert surfaces with terrace diameters in the order of µm, and it can be easily cleaved to attain exceptionally clean surfaces.

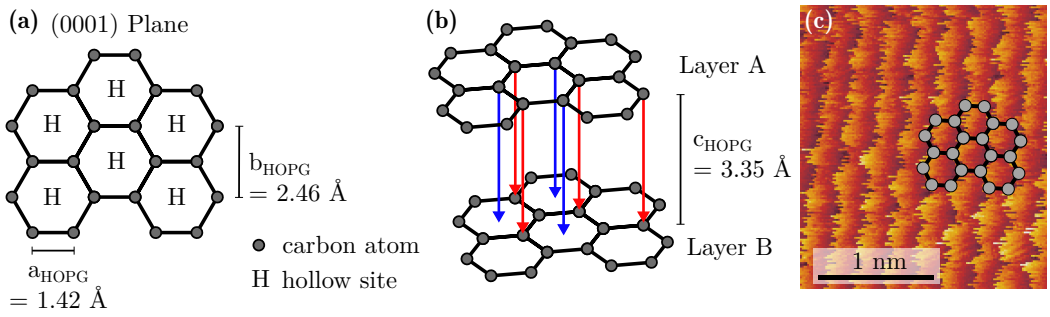

Figure 4.10: Crystal structure of highly orientated pyrolytic graphite (HOPG). (a) View onto the (0001) plane. The carbon atoms form a honeycomb structure with embedded hollow sites. While the section depicted here only contains 6 full carbon rings, sheets can actually span many µm. (b) Natural stacking of two graphene sheets, with an offset of a_{HOPG} and an inter-sheet spacing of c_{HOPG}. Red arrows denote lattice positions where an atom in layer A faces an atom in layer B. Blue arrows show positions where an atom in layer A faces a hollow site in layer B. (c) Typical lateral force map of HOPG recorded with an FFM, showing atomic stick-slip friction (force in arbitrary units). The tip jumps from one hollow site to an adjacent hollow site.

HOPG consists of stacked layers of graphene sheets, in which carbon atoms are linked resembling a honeycomb structure (space group $6_3/mmc$), as shown in Fig. 4.10 (Chung, 2002). The carbon atoms form sp^2 hybridized orbitals with three binding sites orientated in a plane with 120° angles. Their covalent σ-bonds exhibit a separation distance of a_{HOPG}=1.42 Å. The hollow sites of the resulting honeycomb structure are separated by b_{HOPG}=2.46 Å. Individual graphene sheets are then stacked in an alternating ABA pattern, in which layer B has a lateral offset of a_{HOPG} relative to layer A, and is separated from A by a distance of c_{HOPG}=3.35 Å. Bonding between individual sheets is mostly due to van-der-Waals forces. Thus, the bonding within a layer is much stronger than the bonding between two layers. Due to this asymmetry in bonding strength HOPG can be easily cleaved, a process in which complete layers of graphene are removed from the bulk crystal. This property is of tremendous value for friction studies, because it allows to quickly prepare samples with extremely clean, atomically smooth surfaces.

Samples of HOPG consist of many grains of single-crystal graphite. The [0001] direction of all layers are oriented in parallel while the other axes show random distribution (*pyrolytic*). Typical grain sizes in HOPG are 1 µm in diameter. The size of the grains corresponds to the size of the atomically

flat terraces, which are formed after cleaving the sample and are crucial for unhindered movement of the NPs.

For the experiments presented in this work, samples of the highest commercially available quality were used (*Structure Probe Inc., West Chester, PA, USA*, grade ZYA, impurity < 10 ppm), which exhibit typical terrace widths of over 1 µm (cf. Fig. 4.3).

4.6.2 Antimony

Antimony (chemical symbol Sb, derived from the Latin name *stibium*, alchemist symbol ♁ (Dobbs, 1975)) is the element with atomic number 51, located in the 5th period of the periodic table (Mortimer, 2003). The metalloid antimony is allotropic and can exist in two stable structural modifications: grey antimony with rhomboedric lattice structure exhibiting metallic properties and amorphous black antimony (Donohue, 1974), of which the latter can be produced by evaporation onto a cold surface. The hexagonal unit cell of metallic antimony is defined by its lattice parameters of a_{Sb}=4.308 Å for the inter-atomic distance in the (0001) plane and c_{Sb}=3.76 Å for the separation of layers in [0001] direction (Stegemann et al., 2004a). Amorphous antimony has a distinctive short-range order (Richter et al., 1953). It grows in layers with an inter-layer distance slightly different from the crystalline phase of $c_{\mathrm{Sb,a}} = 3.85$ Å and exhibits a density of $\rho_a = 5.8 \times 10^3\,\mathrm{kg/m^3}$ (Aymerich et al., 1975).

4.6.3 Sb Particle Growth on HOPG Substrates

The preparation of Sb particles onto HOPG substrates by thermal evaporation has been discussed in great detail in the literature (Kaiser et al., 2004; Kaiser et al., 1999a; Kaiser et al., 1999b; Stegemann et al., 2004b). When antimony is evaporated, the gas phase at temperatures below T=800 K consists to nearly 100 % of Sb_4 tetrahedral clusters (Mühlbach et al., 1981) with a binding length of 2.687 Å (Kumar, 1993). The ejected Sb_4 clusters perform a soft landing at the HOPG surface (Kaiser et al., 1999a) and migrate with a low diffusion barrier of $E = 60$ meV across the substrate. They aggregate in the so-called Volmer-Weber growth mode, forming three-dimensional nanoparticles which share atomically flat interfaces with the substrate (Stegemann, 2003).

For coverages of below 4 monolayers, the particle growth process results in mostly round particles. Higher coverages produce a different type of particle shape, namely flower-shaped particles with a dendritic structure. By evaluating transmission electron microscopy images of the two particle types it could

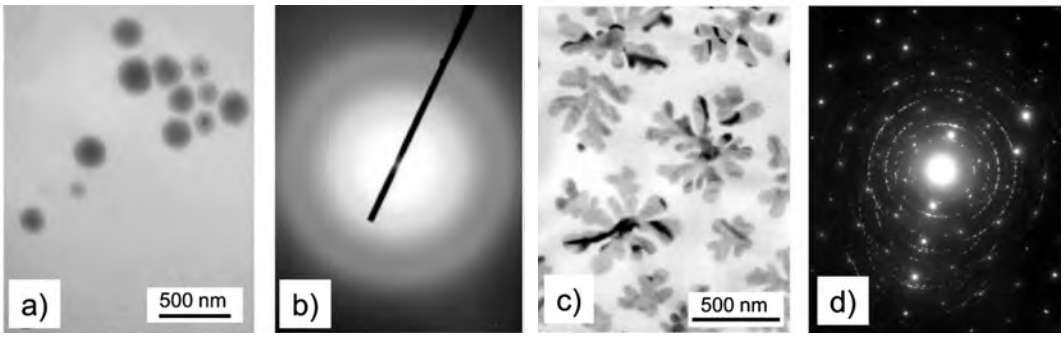

Figure 4.11: Crystallographic structure of Sb particles on HOPG. Small and round Sb nanoparticles were analyzed with a (a) TEM and (b) using selected area electron diffraction. Larger particles, showing a more branched structure, were (c) TEM-imaged and analyzed using (d) selected area electron diffraction. The round particles are amorphous, while parts of the larger particles exhibit crystalline structure. Figure adapted from (Dietzel et al., 2010a).

be demonstrated that round particles predominantly exist in an amorphous structure, while dendritic particles are mostly crystalline, as shown in Fig. 4.11 (Stegemann et al., 2004b; Dietzel et al., 2010a).

4.6.4 Sb/HOPG Sample Preparation Procedure

All samples were prepared using a similar protocol at each AFM system, which allowed to attain reproducible particle sizes and coverages. The particle preparation at the VT-UHV-AFM system (Section 3.5.4) was performed as follows: After the HOPG substrate was loaded into the vacuum system, it was cleaved *in situ* under UHV conditions using adhesive tape. In addition, the sample was baked out for 30 min in order to remove residual adsorbates from the sample holder assembly. Meanwhile, the thermal evaporator, a Knudsen cell loaded with antimony beads of 99.9999 % purity, was heated to 350 °C. Using a mass spectrometer both atomic antimony and Sb_4 clusters were detected in the gas phase. The sample was allowed to cool down to room temperature, and subsequently placed in the emission cone of the evaporator for a duration of 50 s at approximately 15 cm distance from the evaporation aperture.

The sample segment shown in Fig. 4.12b serves as an exemplary result of the described preparation process. A wide variety of different particle sizes and shapes is available for manipulation experiments in this relatively small sample area. A fraction of 16 % of the sample area is covered with 63 antimony particles

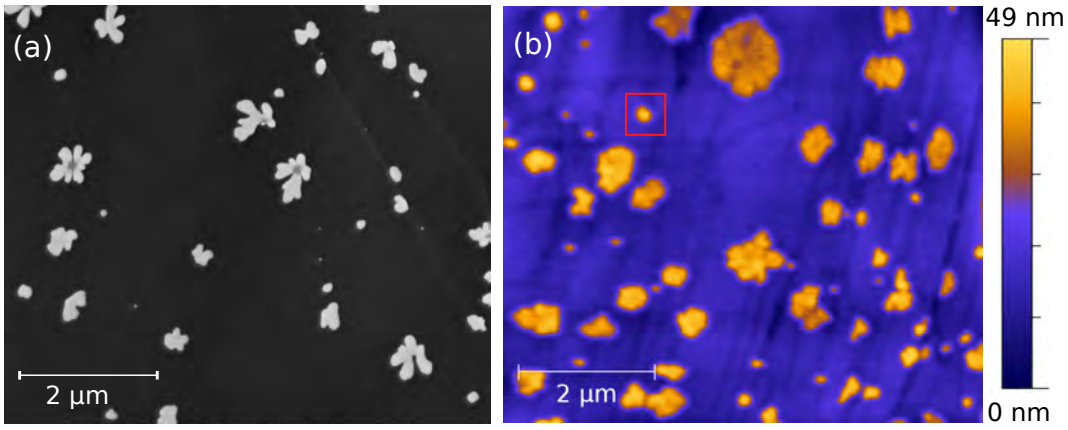

Figure 4.12: Result of the sample preparation of Sb particles grown onto freshly cleaved HOPG. (a) displays an exemplary SEM micrograph of a freshly prepared Sb/HOPG sample. In (b) the AFM topography scan of a different sample section is shown. The red rectangle marks a round particle with a contact area of $A = 59\,000\,\mathrm{nm}^2$, similar to the particles typically used for the manipulation experiments.

with a mean grain radius of 290 nm (maximum: 520 nm, minimum: 44 nm) and a typical maximal height of 20 nm. The particles constituent a cumulative volume of $8 \times 10^{-20}\,\mathrm{m}^3$, decorating a substrate area of $42 \times 10^{-12}\,\mathrm{m}^2$, which corresponds to a coverage of 5.1 ML of metallic Sb and an adsorption rate of $\Gamma = 0.17\,\mathrm{ML/s}$. For the individual sample preparations these values varied slightly due to changes in the evaporator fill level and variations in the chosen evaporation times. Coverages between 5 % and 20 % were found to offer a favourable compromise between island sizes and empty regions needed for particle translations.

The preparation of Sb/HOPG samples at the other two microscope system was carried out in a similar way, with the following distinctions: At the RT-UHV-AFM system and the SEM-AFM system no mass spectrometer was available. But both systems were equipped with quartz crystal micro-balances, which allowed to monitor evaporation rates with high accuracy. Furthermore, at the SEM-AFM system it was not possible to cleave the HOPG substrates *in situ*, and thus cleaving was performed under ambient conditions, immediately before placing the sample into the load lock. Due to the different geometries and resulting differences in adsorption rate, the exposure time had to be adapted in order to attain the desired particle coverage.

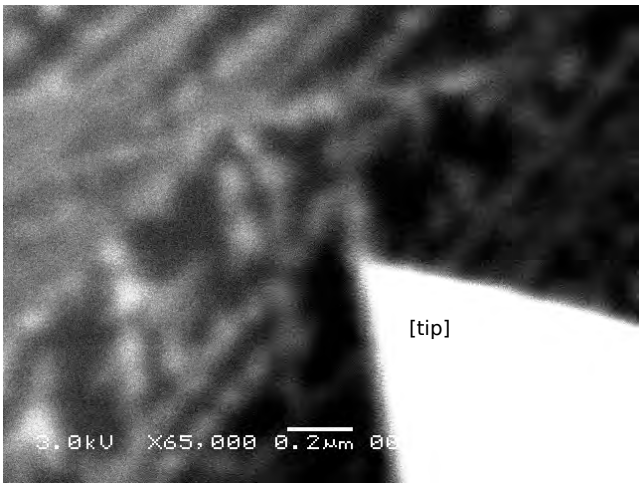

Figure 4.13: SEM micrograph showing Au particles on a HOPG substrate at highest magnification and best resolution attainable with the combined AFM-SEM system. Bright lines indicate the decoration of HOPG step edges with Au particles, but it proved difficult to isolate individual particles. With diameters $d < 100\,\mathrm{nm}$ the particles could not be monitored with high enough precision using the SEM to allow for well-defined manipulation.

4.6.5 Alternative NP Material: Gold

The Sb/HOPG sample system allows to probe friction of amorphous Sb particles on non-matching, crystalline HOPG substrates. In order to compare the results obtained for this system with a sample system of a different crystallographic configuration, samples consisting of gold particles on HOPG substrate have been prepared. In contrast to Sb, gold forms crystalline NPs. The non-matching crystal lattice of Au and HOPG leads to a superlubric sliding behaviour, which differs in its scaling properties from the superlubric sliding of amorphous particles, as reported by Dietzel et al. (2013).

Since the Au particle lattice exposes a 3-fold rotational symmetry, and HOPG has a 6-fold rotational symmetry, orientation-dependent effects on friction are to be expected. Real-time monitoring of Au particles during manipulation could provide valuable insight into the rotational and translational dynamics of this sample system.

To this means it was attempted to prepare Au/HOPG samples at the combined AFM-SEM system. While gold particles could successfully prepared, unfortunately, the resulting gold particles were too small to be reliably imaged with the SEM. An exemplary SEM image of the resulting Au/HOPG sample is

presented in Fig. 4.13.

Attempts to change the preparation procedure to yield larger Au particles were not fruitful, both by using an external thermal evaporator, as well as by utilizing an electron beam evaporator located inside of the preparation chamber. The parameters of the preparation procedure, such as Au ejection rate and target temperature were varied, but the desired increase in particle diameter could not be achieved within the surveyed parameter range. This was presumably due to the limited size of the terraces of the available HOPG substrate, which were most likely not large enough to allow more unhindered and thus more extensive growth per particle, as resulting from the so-called Ehrlich-Schwoebel barriers at the step edges. It has been demonstrated previously by Anton et al. (1998) that the terrace size is a crucial parameter for Au/HOPG particle growth, a parameter which could not be improved within the limited time frame available of this experiment.

Although Au particle manipulations were possible, and a number of friction loops could be recorded, the lack of reliable visual feedback prohibited systematic experimentation using the Au/HOPG samples. Au particle preparations with the RT-UHV-AFM system yielded more well-suited results, with particle diameters larger than 100 nm. The use of NC mode imaging allowed reliable non-realtime particle imaging, which allowed to measure the scaling of friction with contact area of these Au particles (Dietzel et al., 2013).

5 Kinetics of Nanoparticle Friction

Nanoparticles prepared onto atomically smooth surfaces can serve as a unique model system for the study of fundamental kinetics in friction. In this chapter, a number of experiments and simulations regarding NP friction kinetics are presented, which paint a complementary picture of the interface processes in NP friction.

The dependence of nanoscale friction on velocity due to thermal activation (e.g. in the TA-PT model, Section 2.2), resulting in velocity strengthening, has received a lot of attention in the nanotribology community (Gnecco et al., 2000; Sang et al., 2001; Sang et al., 2008; Jansen et al., 2010; Szlufarska et al., 2008). But the effect of contact ageing (cf. Section 2.5), which results in static friction and velocity weakening in kinetic friction, can have an equally significant or even stronger contribution to the overall kinetic friction when compared to thermal activation, as described by Baumberger et al. (2006) for macroscale and mesoscale contacts. Direct observation of nanoscale contact ageing was achieved only very recently by Li et al. (2011). Motivated by these findings, contact ageing in NP friction was investigated in this work, as laid out in the following chapter.

In Section 5.1, the existence of static friction F_S for Sb particles on HOPG substrates is demonstrated, and the distinctly increased value of the static friction F_S, as compared to the kinetic friction F_F, is quantified. Section 5.2 details measurements concerning the complex velocity- and temperature-dependence of the Sb/HOPG system. The findings can be described in terms of a model based on contact-ageing, which is introduced in Section 5.2.3. Stick-slip friction of NPs is presented in Section 5.3, whose observation for the first time allowed to quantitatively measure contact ageing properties of the Sb/HOPG system, and directly assess their significance for NP friction kinetics. In Section 5.4, contact area scaling of the manipulated particles is discussed, and connections are drawn to distinctions in the contact ageing process of different particles.

All measurements presented in this chapter were performed under UHV conditions using Sb particles prepared onto HOPG substrates according to Section 4.6.4.

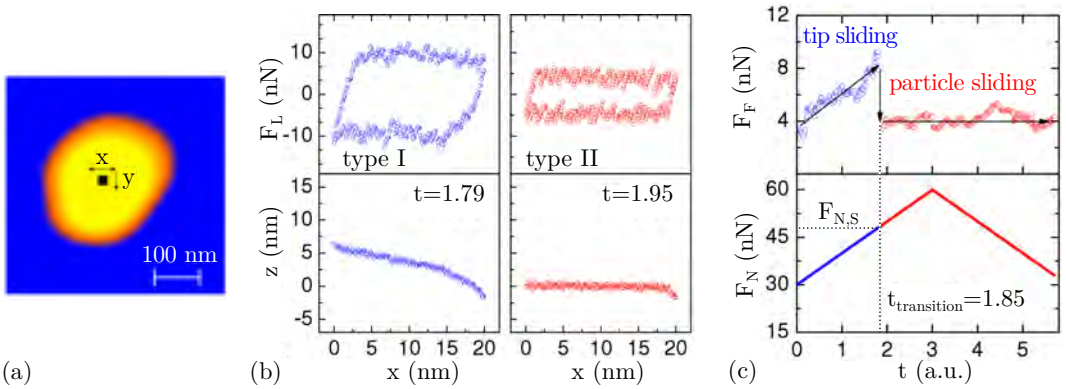

Figure 5.1: Friction measured by placing the AFM tip on top of a NP. (a) depicts the scan region on top of a particle. In (b) two types of lateral force F_L and topography z trace signals are shown. Type I consists of a varying topography signal and large friction loop, associated with the tip moving over the sticking particle. Type II exhibits a flat topography and reduced friction, which corresponds to a movement of the particle in registry with the tip. (c) shows an initial increase of friction with increasing normal force F_N. At $F_N = F_{N,S}$ a distinct drop of friction is observed. When F_N is again reduced, the friction remains constant. Published in (Dietzel et al., 2009).

5.1 Transition from Static to Kinetic Friction

Static friction is commonly observed for the majority of frictional contacts on macroscopic scales. It is, however, not obvious that nanoscale contacts will exhibit a similar behaviour. Here, the first proof of static friction in nanoparticle sliding is presented.

As a means to investigate the static friction of NPs in an easily accessible fashion, the TOT manipulation mode was used in particular way, which did not require high temporal measurement resolution and was feasible with standard AFM controller software: The AFM tip was placed on top of a NP near its center (Fig. 5.1a). At low normal loads, a small part on the particle was scanned. The resulting non-uniform topography signal indicates that the tip was moved relative to the particle, while the particle itself was pinned to the surface (Fig. 5.1b, traces of type I). During the repeated scanning of the particle, the normal force F_N was gradually increased. At a certain normal force threshold a sudden change in the friction and topography traces was observed (Fig. 5.1b, traces of type II): the topography signal became flattened, and the friction was significantly reduced. This observation indicates that at the point where

$F_N \geq F_{N,S}$, Eq. (4.2) became fulfilled. The kinetic friction between tip and particle then exceeded the static friction between particle and substrate and the particle started to move, in compliance with the tip. It follows that the maximum of the measured friction signal corresponds to the static friction between particle and substrate.

After this transition from static to sliding friction the particle was repeatedly translated back and forth, while the normal force was again reduced gradually. It was observed that even if the normal force was reduced below $F_{N,S}$, traces of type II were still observed, indicating a movement of the particle relative to the substrate, and thus resulting in the hysteresis depicted in Fig. 5.1c.

This measurement protocol was repeated four times for a single nanoparticle, and consecutively reproduced for a total of five different particles. All particles exhibited similar characteristic behaviour, as described for the initial manipulation. In particular all particles exposed a very similar ratio of static to sliding friction, with a mean ratio of 0.48 ± 0.07.

Of special interest is the observation that the static friction was re-established each time after the particle was kept motionless for some time in the order of 10 minutes in between consecutive runs of the main measurement protocol. At the turnaround points of the scan, on the other hand, at which the manipulation was halted for approximately 25 ms, the static friction was not regenerated. This observation proves that the build-up of static friction of NPs is a time-dependent process, which may be described in terms of contact ageing.

Furthermore, it can be observed that an increase of the normal force F_N changes the lateral friction signal only if the tip moves relative to the particle, and not while the particle moves relative to the substrate. This can be understood by considering the two interface geometries: While the tip-particle interface resembles an elastic Hertzian contact (cf. Section 2.4), whose contact area changes with the normal force, the particle-substrate interface is flat, resulting an approximately constant contact area for varied normal forces. This observation further confirms the validity of quantitative measurements using the TOT manipulation approach. It can be noted that due to the much larger extent of the particle-substrate contact compared to the tip-particle contact, equal normal forces at these two contacts result in very different pressure distributions in the respective interfaces.

The experiment was performed using the RT-UHV-AFM (cf. Section 3.5.3). Force sensors of the type 'CSC37' (*Mikromasch, NanoAndMore GmbH, Wetzlar, Germany*) were utilized. One silicon holder chip of this sensor type houses an array of three separate cantilevers of differing stiffnesses, with k_z typically ranging from 0.4 N/m to 0.8 N/m. This sensor setup allowed to quickly test

different cantilevers and select a suitable sensor for the manipulation. While softer cantilevers generally should be preferred, since they offer higher resolution in the force measurements, the sensors still need to be stiff enough to enable sufficient normal forces to be exerted in order to move the particles.

As a result, this experiment clearly exposes the existence of static friction for the probed sample system. After particle sliding has been initiated, static friction could be re-established by keeping the particle pinned in stationary contact to the substrate for sufficiently long hold times. While the transition from static to sliding friction ensued in a discontinuous manner, the crossover from sliding to static friction appeared to be a more gradual process, since halting the manipulation for 25 ms did not reestablish static friction, while halting for some minutes did regenerate static friction. The precise nature of this gradual change is investigated through further measurements in Section 5.3.

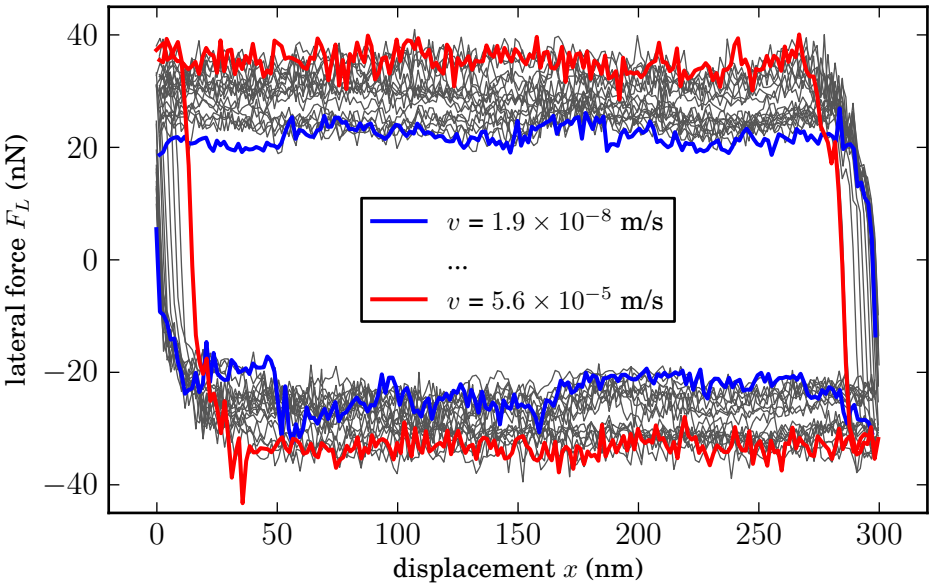

Figure 5.2: Friction loops of particle A1 with varying velocity, recorded at a temperature of T=200 K. The particle was translated along the same path for 20 repetitions, starting with a velocity v of 1.9×10^{-8} m/s (blue) and increasing up to $v = 5.6 \times 10^{-5}$ m/s (red). A significant change of friction with velocity is observed.

5.2 Velocity- and Temperature-Dependence of NP Friction

To gain insights into the complex kinetics involved in nanoscale and NP friction, experiments regarding the dependence of friction of individual particles on velocity and temperature were conducted. Both the TA-PT model and the MK model predict a significant, although dissimilar variation of friction with velocity and temperature. However, *a priori* it is completely ambiguous if any of these models will be suitable to describe the friction of extended nanocontacts such as the Sb NPs used in this study.

5.2.1 Measurement Protocol

The experiment was implemented at the VT-UHV-AFM (see Section 3.5.4) at a base pressure of $p < 4 \times 10^{-10}$ mbar, using Sb/HOPG samples prepared according to Section 4.6.4.

All manipulations for this experiment were carried out in TOT mode, since

in this mode only limited manual repositioning of the tip is necessary. Instead, the tip could remain on top of the nanoparticle for a full velocity sweep, during which friction loops with different velocities were recorded consecutively. Normal forces were typically set to $F_N = 25\,\mathrm{nN}$. To rule out gradual changes of friction with the number of manipulations, such as wear effects, velocity sweeps were performed in two steps. First, the velocity was gradually increased from low to medium velocities ($2 \times 10^{-8}\,\mathrm{m/s}$ to $2 \times 10^{-6}\,\mathrm{m/s}$ in 10 steps). This low-velocity pass was then repeated for a second time. Subsequently, the velocity was swept from medium to high velocities ($2 \times 10^{-6}\,\mathrm{m/s}$ to $6 \times 10^{-5}\,\mathrm{m/s}$ in 10 steps), which again was repeated once. This protocol allowed to always compare two measurements at the same velocity with 9 manipulations in between. By using two velocity ranges, the velocity dependences would reveal wear effects by exhibiting discontinuities between both ranges. No such discontinuities were observed. This two-fold process was implemented in software using the GXSM system to ease the manipulation procedure (cf. Section 3.5.2). Effectively, each sweep could be initiated by simply pressing a button in the controller software, which allowed to quickly record a large number of sweep runs with each individual particle.

Figure 5.2 shows an example of 20 NP friction loops recorded by uninterrupted manipulation of a single particle, for a range of velocities between $1.9 \times 10^{-8}\,\mathrm{m/s}$ and $5.6 \times 10^{-5}\,\mathrm{m/s}$. The particle was repeatedly manipulated along the same trajectory, at a temperature of T=200 K. The significant dependence of friction on velocity is already obvious in Fig. 5.2.

The aforementioned velocity sweeps were recorded at a number of different temperatures. Since the change in temperature resulted in significant drift of the location of the sample relative to the sensor, it was necessary to constantly monitor the sample topography in NC mode and track the current scan position by performing coarse adjustments over distances of several µm. Using this approach it was possible to track the exact same particles over a temperature range from 300 K down to 30 K and back to 300 K. The rate of temperature variation was limited to 50 K/h, with an estimated uncertainty of the steady-state values of ±5 K. As to estimate the time until thermal equilibrium was achieved, the lateral drift between successive topography scans was monitored. Approximately an hour after the thermocouple located near the sample indicated a stabilized temperature, the drift was reduced to levels observed at RT, which were determined to be smaller than 4 Å/s, and the measurements were resumed.

The sequence of temperature steps for the NP friction measurements consisted of an initial reference measurement at room temperature, followed by a cool-down to 50 K. The temperature was then increased in steps of 50 K, while

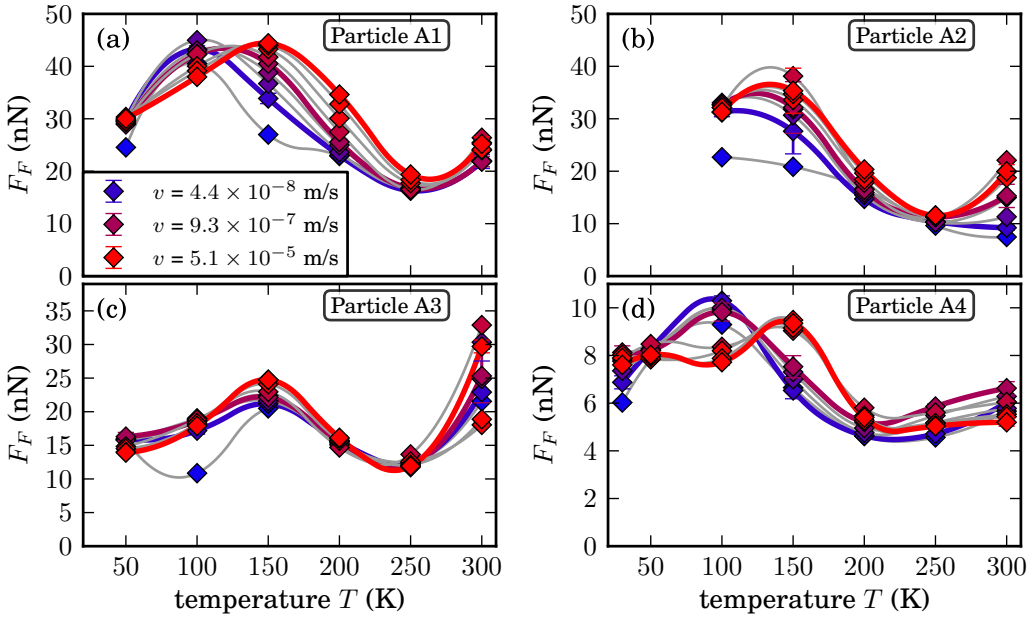

Figure 5.3: Friction force F_F depending on temperature T at different velocities v for particles A1–A4. Markers represent averaged measurement data, while connecting lines are constructed as guides to the eye. All particles exhibit a peak in their friction levels between 100 K and 150 K, as well as a minimum at around 250 K. No data for particle A2 at temperatures below 100 K is available, since in this case liquid nitrogen was used as the coolant. Due to very rapid expenditure of liquid helium at the highest cooling rates, measurements at 30 K were only performed with particle A4. The respective contact areas of particles A1–A4 were determined using topography images to 54 000 nm^2, 101 000 nm^2, 118 000 nm^2, and 19 000 nm^2, with an approximated uncertainty of ±10%.

the final measurement was again performed at room temperature, allowing to gauge the overall change in friction related to wear and to identify general irreversible interface changes.

5.2.2 Results: Complex v- and T-Dependence of NP Friction

The measurements yielded a complex interdependence of friction on velocity and temperature. It thus appears beneficial to survey the data from two different perspectives: First as friction depending on velocity at a number of

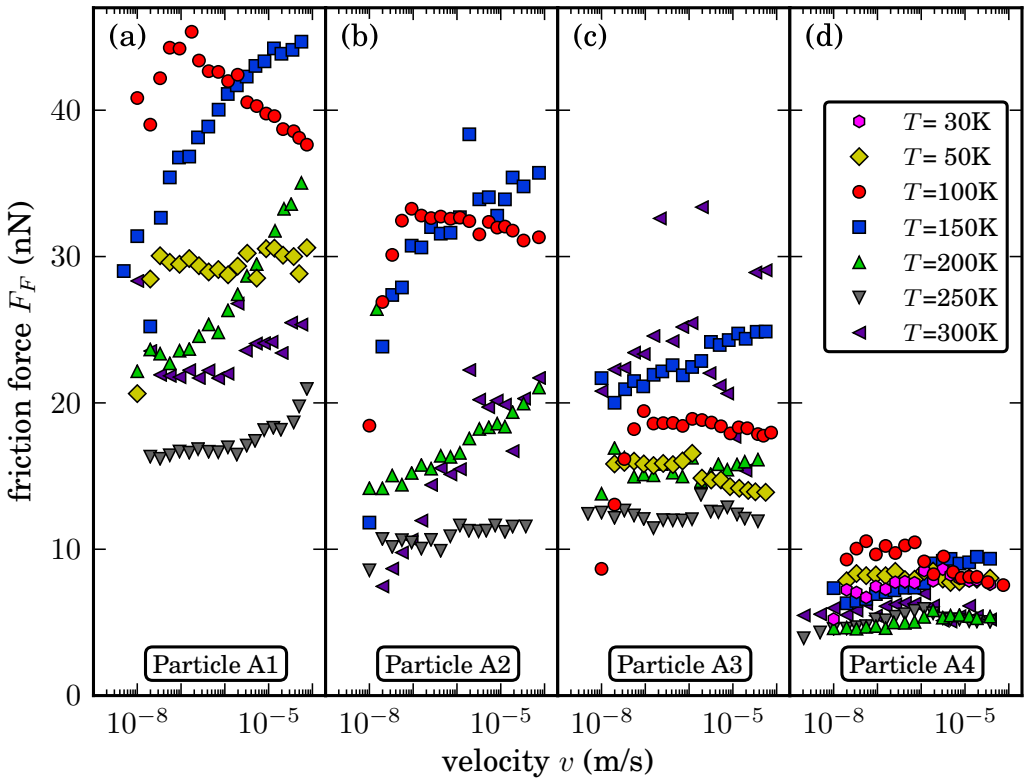

Figure 5.4: Friction force F_F depending on velocity v for particles A1–A4. Each marker represents the averaged value of friction for a particular combination of v and T over at least two friction loops. While the particles exhibit increasing friction with increasing velocity (*velocity strengthening*) for most temperatures, the opposite trend of decreasing friction with velocity (*velocity weakening*) is observed for T=100 K. At T=300 K and 50 K the friction isotherms are almost constant in respect to v.

different but constant temperatures, as well as the other way around, with varying temperatures at different but constant velocities.

Figure 5.3 shows the experimental findings regarding the temperature dependence at different velocities for four particles A1–A4. A strong non-monotonic dependence of friction on temperature is revealed, in which the friction changes by a factor of between 2 and 4. Maxima can be observed in the temperature range between 100 K and 150 K, while a minimum exists at around 250 K. The variation of friction with velocity is largest at 150 K for the majority of particles, while at 300 K the variation is again high.

The results of the velocity-dependent measurement at different temperatures

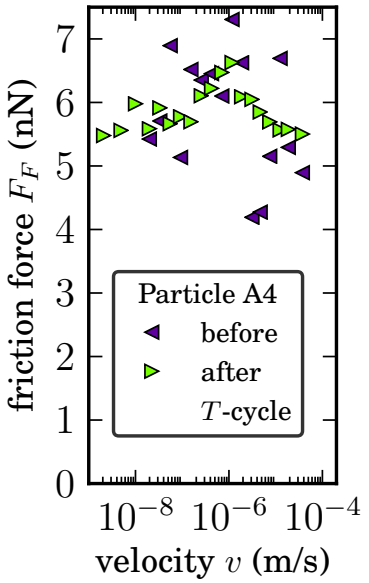

Figure 5.5: Friction force F_F measured for a particle before and after a full temperature-variation cycle. No systematic change in the friction level is observed, even for the shown particle A4, which was the smallest particle manipulated in this measurement.

for particles A1–A4 are plotted in Fig. 5.4. The dependence of the friction force F_F on the logarithm of the velocity $\ln(v)$ reveals constant or increasing friction with increasing velocity for temperatures between 300 K and 150 K, while at T=100 K the friction decreases with increasing v. At 50 K friction is nearly independent of v. Absolute values of friction differ significantly between particles, a consequence of the different contact areas of the four particles, which will be discussed in Section 5.4.

Validation of the Absence of Contact Alteration and Reference Measurements

To verify the validity of the measurement method, reference measurements have been performed. Figure 5.5 exemplifies the friction and velocity dependence at room temperature for an individual particle before and after a complete cycle of temperature variation and velocity sweeps. No significant difference in the particle friction before and after the temperature- and velocity-cycle was found. The other particles showed similarly unaltered friction. Two particles were fused together at $T = 250$ K and could not be separated again for final reference measurements at 300 K.

In addition to the NP friction data, the friction of the direct tip-HOPG contact was recorded. Figure 5.6 depicts the result of the tip-sample friction measurement recorded during the temperature cycle for particle A4. It can be

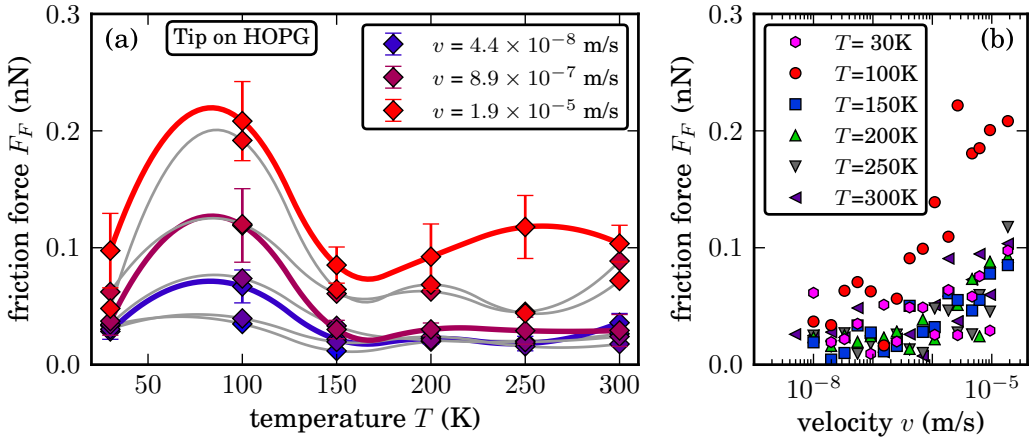

Figure 5.6: Reference measurement of the friction force F_F of the direct tip-substrate contact. The temperature dependence in (a) exhibits a distinct peak at T=100 K. (b) The velocity dependence features exclusively increasing friction with increasing velocity. The absolute values of tip-substrate friction are smaller than the lowest measured particle-substrate friction by a factor of 40.

seen that a peak occurs in the temperature dependence at T=100 K, similar to the temperature characteristic found for NPs. A comparable friction peak in the temperature dependence has been reported by Barel et al. (2010b). Interestingly, the velocity dependence shows only friction isotherms increasing with velocity, which is in direct contrast to the observed velocity weakening of the NPs at T=100 K. The absolute friction values are significantly lower than what is observed for the NP friction measurements by at least a factor of 40. Thus, even if by chance a TOT manipulation degenerated into TOS pushing due to the tip sliding down from the particle, the additional contribution of the tip-HOPG friction can be safely neglected.

Comparison with the MK Model

Previous temperature- and velocity-dependent NPs experiments of silica on silica contacts showing comparable trends in the dependence on velocity and temperature could be successfully fitted by simulations based on the MK model by Barel et al. (2010a). The same attempt was made for the nanoparticle friction data presented here, but the results were unsatisfying, mainly due to the rapid freeze-out of the rebinding at lower temperatures; the MK model predicts an exponential dependence of F_F on $1/T$ in the limits of low T. Furthermore, the

MK model leads to almost vanishing friction in the high temperature limit, which was not observed here. With certain modifications of the MK model (e.g., statistical distribution of bond energies) these discrepancies could probably be reduced. However, while it may well be applicable to the silica-silica contact in the previous experiments (Barel et al., 2010a) and corroborated by simulations (Mo et al., 2009), the underlying concept of multiple, individually acting bonds at the interface, and in particular the existence of a rebinding energy barrier, is difficult to imagine in the presented case of flat, van-der-Waals bound Sb particles on HOPG. Consequently, a more suited model to describe these findings will be developed in the following section.

5.2.3 Contact Ageing Model with Thermal Activation

Since the interpretation of the measurement results found in Section 5.2 using the MK model is unsatisfactory, a different route to model the observed NP friction was taken. It is already established through the findings in Section 5.1 that static friction arises in the Sb/HOPG system, and the occurrence of static friction is usually a result of contact ageing (see Section 2.5). It has been demonstrated previously that contact ageing can have a significant effect on kinetic friction dominated by stick-slip dynamics (Baumberger et al., 2006), including the emergence of velocity weakening. Consequently, it appears appropriate to devise a model based on contact ageing to explain the experimental findings.

Mathematical Model Formulation

In order to mimic the NP manipulation measurements in this new model, which will be referred to as the thermally activated contact ageing (TA-CA) model, a rigid tip of mass M and center-of-mass coordinate X is considered, which interacts with the underlying surface through a single bond with an energy barrier ΔE_{off} and a stiffness κ, whose unbinding is thermally assisted. The tip is connected by a spring with stiffness k to a moving support, similar to the PT model. Effectively, the equation of motion given as (Barel et al., 2010a)

$$M\ddot{X} + \eta\dot{X} - \kappa(X - X_{\mathrm{sl}}(t)) + k(X - vt) = 0 \tag{5.1}$$

is integrated, with the viscous damping constant η and the location of the previous slip event $X_{\mathrm{sl}}(t)$.

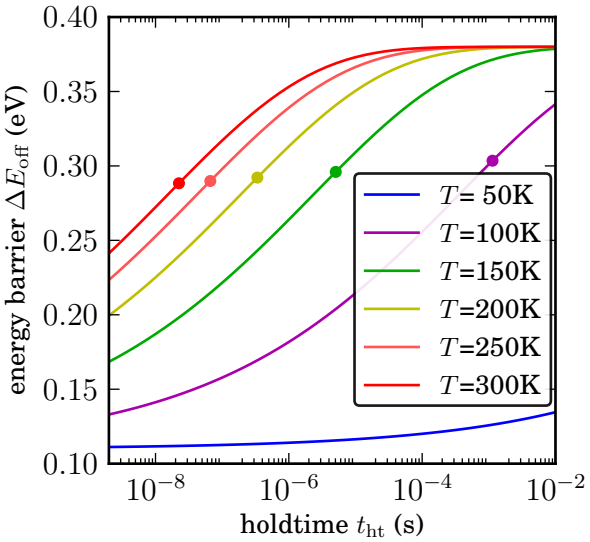

Figure 5.7: Energy barrier ΔE_{off} plotted against the hold time t_{ht} for different temperatures T. The curves shift along the t_{ht}-axis with changing temperature. Circles denote $t_{\mathrm{ht}} = 1/\lambda$. All curves asymptotically approach constant values of $\Delta E^0_{\mathrm{off}}$ and $\Delta E^0_{\mathrm{off}} + \Delta E^1_{\mathrm{off}}$ for low and high t_{ht}, respectively. Simulation parameters are identical to the values listed in Fig. 5.11.

Here, a contact ageing phenomenon was adopted by introducing a time-dependent contact breaking energy barrier ΔE_{off}:

$$\Delta E_{\mathrm{off}}(t) = \Delta E^0_{\mathrm{off}} + \Delta E^1_{\mathrm{off}} \cdot (1 - \exp(-(t\lambda)^{\alpha})) \tag{5.2}$$

with the energy constants $\Delta E^0_{\mathrm{off}}$ and $\Delta E^1_{\mathrm{off}}$, the relaxation rate λ, and the stretch factor α.

The selection of this function is motivated by the observation of a logarithmic increase of the static friction force with time in a number of experiments (Li et al., 2011; Dieterich, 1978) and has been used before in modeling static friction and contact ageing (Gitis et al., 1992; Braun et al., 2002; Persson, 1998). Previous works have indicated an upper limit for the logarithmic increase in static friction (Armstrong-Helouvry et al., 1994; Liu et al., 2012), and thus an upper and a lower boundary for the energy barrier is introduced in this model. Equation (5.2) results in a logarithm-like increase with time (linear in $\ln(t_{\mathrm{ht}})$) around $t_{\mathrm{ht}} = 1/\lambda$ (see Fig. 5.7).

The effective energy barrier of the contact ΔE_{off} grows with time, starting at $\Delta E^0_{\mathrm{off}}$ and increasing up to $\Delta E^0_{\mathrm{off}} + \Delta E^1_{\mathrm{off}}$ at infinite hold times. Figure 5.8 illustrates the effect of contact ageing on the energy landscape in the closely related PT model.

A crucial point in the model here is the introduction of a temperature dependence of the rate λ according to an Arrhenius-type law as in

$$\lambda = \Omega_{\mathrm{Relax}} \cdot \exp(-\Delta E_{\mathrm{Relax}}/\mathrm{k_B}T). \tag{5.3}$$

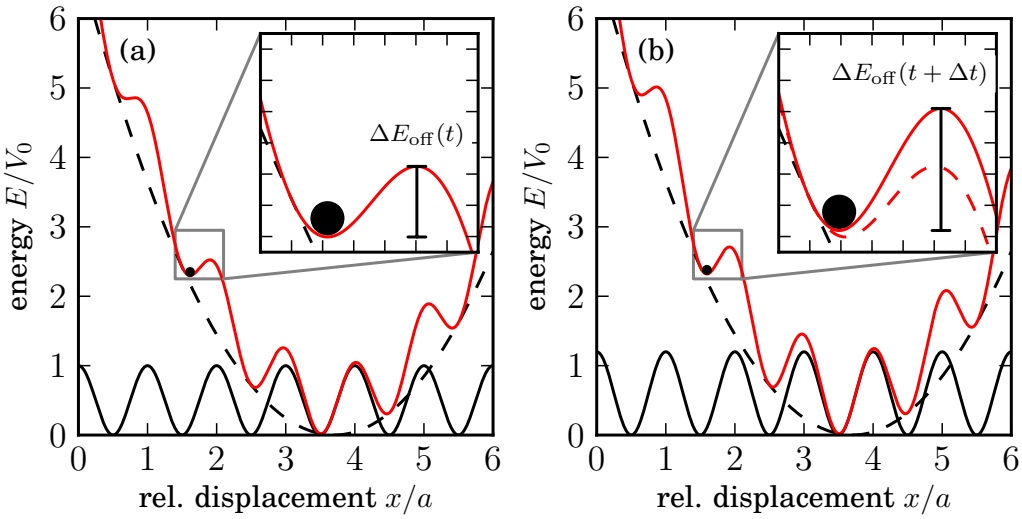

Figure 5.8: Visualization of contact ageing using the PT model. After the tip (black dot) was kept in a local minimum of the combined potential V_{PT} (solid red line) for a time Δt, the energy barrier that the tip needs to overcome in order to jump to the next minimum was increased from (a) $\Delta E_{\mathrm{off}}(t)$ to (b) $\Delta E_{\mathrm{off}}(t+\Delta t)$. Following a jump the energy barrier is reset to $\Delta E_{\mathrm{off}}(t=0)$.

Equation (5.3) models a relaxation process of the interface, which involves a characteristic energy barrier $\Delta E_{\mathrm{Relax}}$ that needs to be overcome in order for the interface to relax into a lower energy minimum, equivalent to an increase in $\Delta E_{\mathrm{off}}(t)$. In contrast to the MK model, where bonds are broken individually, here a rigid particle is assumed, which has to be thermally activated in its entirety. This feature is motivated by the observation of structural lubricity (see Section 5.4), which can only emerge if the interfaces are sufficiently stiff. It appears plausible that the actual physical reality corresponds to a hybridization between these two extremes.

This model construction can further be motivated with the consideration of N abstract bonds initially bound within an energy minimum φ_0 with the energy $\Delta E^0_{\mathrm{off}}/N$. They are allowed to relax into a more strongly bound minimum φ_1 with the energy $\left(\Delta E^0_{\mathrm{off}} + \Delta E^1_{\mathrm{off}}\right)/N$, separated by an energy barrier $\Delta E_{\mathrm{Relax}}$. An example of two such energy states was found by Kim et al. (2011) using MD simulations for SiO_x contacts. N_0 and N_1 denote the number of bonds in state φ_0 and φ_1, respectively, and $N = N_0 + N_1$. Each junctions is initially assumed to be in state φ_0. Then the differential formulation of the problem

becomes

$$\frac{\mathrm{d}N_0}{\mathrm{d}t} = -\lambda N_0, \tag{5.4}$$

analogous to Equation (3) in (Gnecco et al., 2000), but with N junctions instead of one. This leads to the well-known exponential decay of the form

$$N_0(t) = Ne^{-\lambda t} \tag{5.5}$$

$$N_1(t) = N(1 - e^{-\lambda t}) \tag{5.6}$$

It follows that the total energy barrier in this case is given as Eq. (5.2), with the stretch factor $\alpha = 1$. Here, back-jumps and changes in contact stiffness are neglected, as well as coupling between the junctions, which could lead to a sub-linear summation of energy barriers. The stretched exponential function with $\alpha < 1$ then follows, if a distribution of relaxation energy barriers $\Delta E_{\mathrm{Relax}}$ instead of a single value is assumed (see next paragraph). Other interpretations include the use of a state probability $\mathrm{P}(t)$ associated with a single process, instead of a number N of different bonds, similar to the mechanism described by Evstigneev et al. (2008). It has to be noted that the bonds used to illustrate the model concepts in this paragraph are not necessarily identical to actual individual chemical bonds, but can represent different kinds of double-well states with decay-like processes.

The term $\exp\left(-\left(t\lambda\right)^{\alpha}\right)$, with $0 < \alpha \leq 1$, is known as a stretched exponential decay function (Johnston, 2006). Choosing $\alpha < 1$ accounts for a whole distribution of relaxation rate constants λ (and thus of energy barriers $\Delta E_{\mathrm{Relax,i}}$), which improved the fit of the model to the experimental data significantly.

Unbinding in this model is evaluated using the detachment rate

$$k_{\mathrm{off}} = \Omega_{\mathrm{off}} \exp\left(-\frac{\Delta E_{\mathrm{off}}(t)(1 - f/f_C)^{3/2}}{\mathrm{k_B}T}\right) \tag{5.7}$$

where the critical force f_C is given as

$$f_C = \sqrt{2\kappa \cdot \Delta E_{\mathrm{off}}(t)} \tag{5.8}$$

and constitutes the maximum binding force. Ω_{off} characterizes the attempt frequency of detachment. Here, the energy barrier vanishes according to a power law in the force with an exponent of 3/2, as demonstrated by Sang et al. (2001).

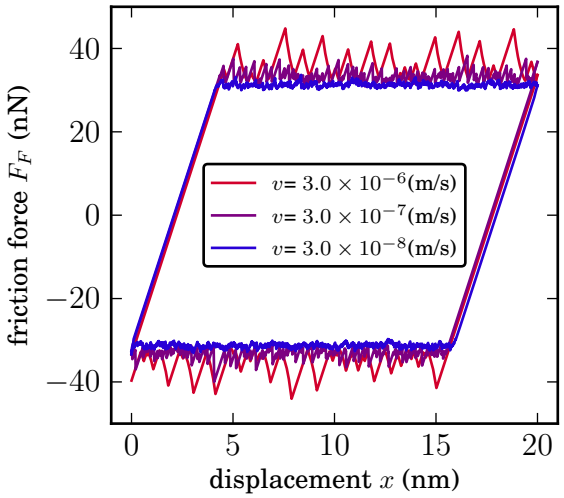

Figure 5.9: Simulated friction loops at different velocities for $T = 200\,\mathrm{K}$. The friction traces exhibit stick-slip-type friction, in this case most pronounced at high velocities.

Monte Carlo Simulations with the TA-CA model

Monte Carlo simulations use random sampling from given probability distributions in order to approximate stochastic problems, for which the analytical treatment is too complex to be carried out. A Monte Carlo-type stochastic property is realized in this simulation by multiplying k_{off} with the time step Δt, giving an estimate of the jump probability per time interval $P(\Delta t) = \Delta t \cdot k_{\mathrm{off}}$ (Barel et al., 2010a). A random variable ξ is now introduced, which is sampled at each simulation step from a uniform distribution ranging from 0 to 1. If the condition $\xi < P(\Delta t)$ is fulfilled at the times t_i, then the bond is detached at each t_i. It gets reattached immediately at the current tip position in a relaxed state, thus setting the state variable $X_{\mathrm{sl}}(t)|_{t=t_i}^{t_{i+1}} = X(t_i)$ and $\Delta E(t_i) = \Delta E(0)$.

The model was implemented as a simulation written in Python. The time step was chosen as $\Delta t = 10^{-8}\,\mathrm{s}$, a compromise between high temporal resolution and computational feasibility. This choice of Δt resulted in a jump probability of $P(\Delta t) < 0.2$ for all steps. Most stick-slip events observed during the simulation occur at time intervals many orders of magnitude larger than Δt.

Simulation Results

With the aim of assessing the validity of the TA-CA model, one of the manipulated particles was selected and it was attempted to fit simulation results obtained from this model to the experimental findings. For reference, the experimental results for the chosen particle A1 are aggregated in Fig. 5.10.

To fit the TA-CA model to the experimental data the parameters $\Delta E_{\mathrm{off}}^{0}$,

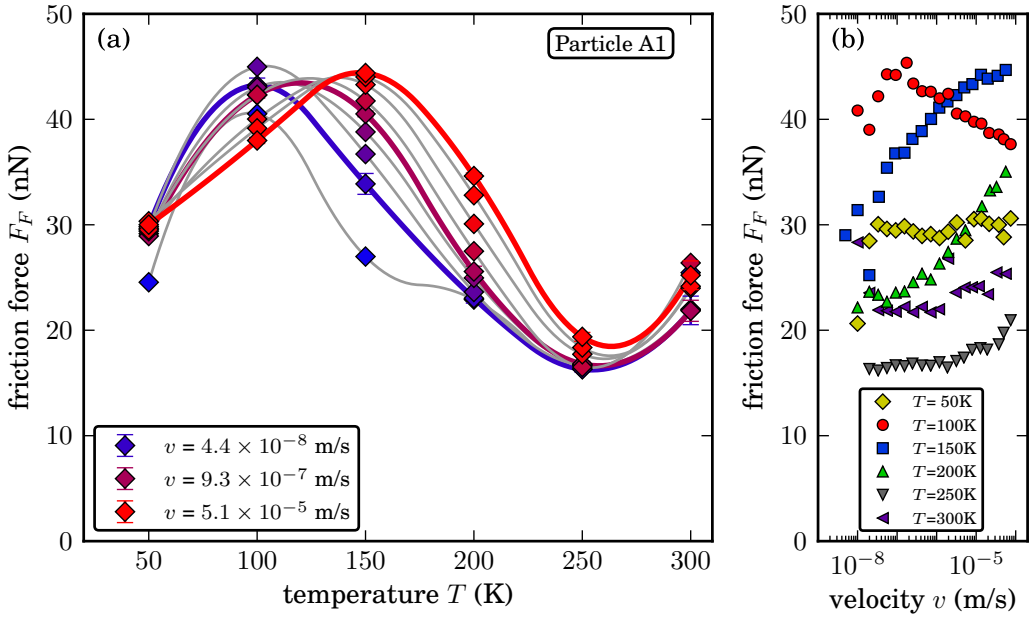

Figure 5.10: Experimental results for measured velocity- and temperature-dependence of friction for particle A1 (previously shown in Figs. 5.3 and 5.4). This experimental data was used as the reference for the simulation.

ΔE^1_{off}, ΔE_{Relax}, α, κ and η were varied. The spring constant k was taken from the cantilever calibration, and the values of tip mass M and attempt frequencies Ω were adopted from (Barel et al., 2010b). Figure 5.7 displays the characteristic time- and temperature-dependence of Eq. (5.2), employing the parameters used to fit the experimental results. In Fig. 5.9, typical friction traces resulting from the simulation are shown. The TA-CA model yields stick-slip type friction over a wide range of temperatures and velocities. These were not evident in the here shown experiments due to low sampling frequencies, but subsequent measurements with higher sampling frequency at room temperature with a different AFM system did indeed display stick-slip type particle movement, as described in Section 5.3.

Using simulated friction loops as obtained from a whole range of velocities and temperatures, the complete velocity- and temperature-dependence could be extracted, as is displayed in Fig. 5.11. These simulation results are in very good agreement with the experimental findings shown in Fig. 5.10 in the temperature range from 50 K to 250 K. Notably, the peaks in the friction-temperature curve at around 100 K to 150 K and the characteristic reversal in the $\ln(v)$-dependence

are well reproduced.

This good agreement in turn allows to correlate different friction regimes with the contact ageing processes. At temperatures below 50 K the time-dependence of the detachment barrier ΔE_{off} is extremely weak (see Fig. 5.7). For typical hold times during the stick phase of up to 2×10^{-4} s at a velocity of $v = 3 \times 10^{-6}$ m/s and up to 4×10^{-3} s at $v = 3 \times 10^{-8}$ m/s the data from Fig. 5.11a predicts an almost constant energy barrier $\Delta E_{\text{off}}(t)$, staying at its lower limit. In effect, the simulation results resemble a thermally activated bond rupturing (TA-PT-model) behaviour (lower grey line) with $\Delta E_{\text{off}}(t) \approx \Delta E^0_{\text{off}}$, and friction decreases with temperature. Since no measurements were performed with temperatures below 50 K, this range of temperatures currently cannot be compared directly to experimental results.

The other limiting case is where $\Delta E_{\text{off}}(t)$ is fixed at the upper limit $\Delta E^0_{\text{off}} + \Delta E^1_{\text{off}}$ (upper grey line). In the simulations at temperatures above 200 K, the sticking phase will see a $\Delta E_{\text{off}}(t)$ which is almost completely saturated at its upper bound. Thus, for $T > 200$ K, the simulation again exhibits TA-PT-like characteristics, which are similar to results with a constant energy barrier.

The rising friction in the temperature regime from 50 K to 150 K ensues from the fact that the energy barrier height that the particle sees, immediately before the slip event takes place, will increase with higher temperature, leading to a strong friction enhancement. The simulation curves produced with time-varying $\Delta E_{\text{off}}(t)$ approach the fixed-energy-barrier curve at high temperatures, because in the stick phase the energy barrier nearly saturates. They do not fully converge, since even at high temperatures the time-dependence of $\Delta E_{\text{off}}(t)$ is of significance due to short bond rupture times in the slip phase of the order of $t = 10^{-7}$ s. Opposite to the friction enhancement trend, thermal activation will lead to friction reduction as in the PT model and overall a broad friction peak is observed in good agreement with the experiments.

Taking the contact ageing effect into account, Figure 5.11b depicts the corresponding simulated velocity dependence of the sliding friction. At most temperatures friction increases with increasing velocity, in agreement with the TA-PT model. However, at the distinct temperature of 100 K, the friction shows a characteristic decrease with increasing velocity. In this case a significant increase of $\Delta E_{\text{off}}(t)$ in the stick phase can take place without going into saturation, and thus overcompensating the thermal activation effect. This feature is in good agreement with the measurement results in Fig. 5.10b.

Despite the good agreement it is found that for higher temperatures above 250 K the experiments again show a slight increase of friction with temperature, while the simulation yields only TA-PT-like frictional decrease. Additionally,

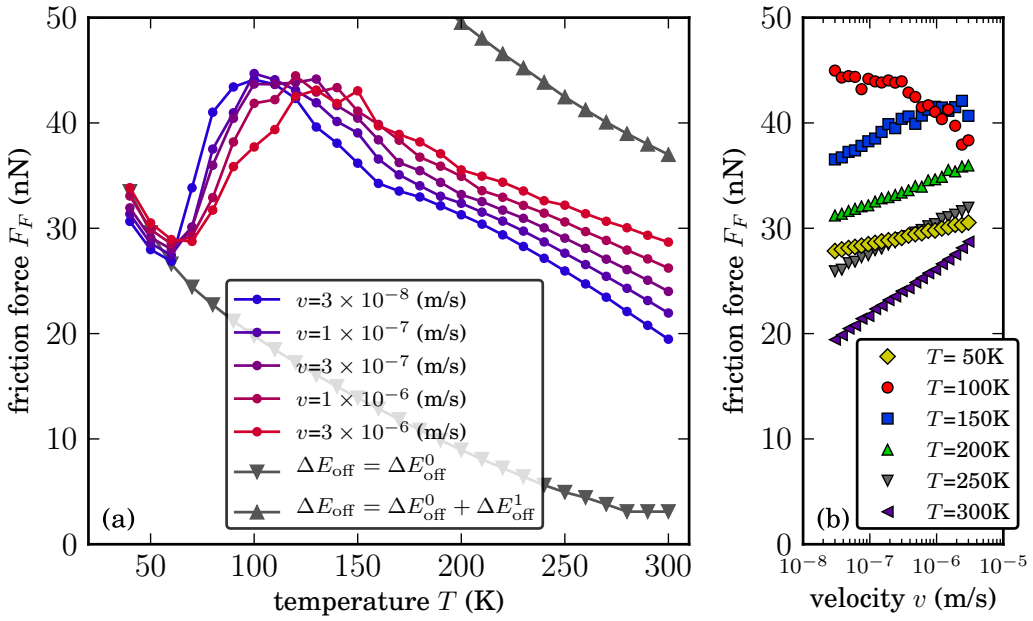

Figure 5.11: Simulation results for simulated velocity- and temperature-dependence of friction in the contact ageing model. The model parameters were fitted to resemble the experimental results shown in Fig. 5.10: $\Omega_{\mathrm{Relax}} = 10^{10}\,\mathrm{Hz}$, $K = 15\,\mathrm{N/m}$, $\kappa = 2 \times 10^5\,\mathrm{N/m}$, $\eta = 5 \times 10^{-5}\,\mathrm{kg/s}$, $\Delta E_{\mathrm{Relax}} = 0.14\,\mathrm{eV}$, $\Delta E^0_{\mathrm{off}} = 0.11\,\mathrm{eV}$, $\Delta E^1_{\mathrm{off}} = 0.27\,\mathrm{eV}$, $\alpha = 0.2$. The presented results were obtained as averages of simulated friction traces over a distance of 50 nm. Additional simulations with constant ΔE_{off}, shown as grey markers in (a), were performed at constant velocities of $3 \times 10^{-6}\,\mathrm{m/s}$.

at higher temperatures, the simulation shows a stronger dependence on $\ln(v)$ than what is observed in the measurements. The introduction of an additional summand $\Delta E^{(2)}_{\mathrm{off}} \cdot (1 - \exp(-(t\lambda^{(2)})^{\alpha^{(2)}}))$ into Eq. (5.2) may be used to replicate these features, representing a third binding state φ_2 with a higher binding energy and increased relaxation barrier $\Delta E^{(2)}_{\mathrm{Relax}}$. To keep the model reasonably simple, it was refrained from including this second relaxation process in the simulation presented here. However, in general, every additional energy barrier can lead to a peak in the friction temperature curve and corresponding behaviour in the friction-velocity curves. Those energy barriers represent different contact ageing and relaxation mechanisms, e.g. ageing from atomic relaxations, defect migration and elastic responses.

The simulation results are in very good agreement with the experimental data, suggesting that the friction of the employed sample system is indeed

governed by thermally activated contact-breaking in combination with a time- and temperature-dependent strengthening of the contact, i.e. contact ageing. The atomistic mechanism that leads to this bond strengthening at the particle-surface interface is not yet fully understood, but may be described by the delayed creation of atomic bonds or gradual growth of junctions as well as conformational relaxation of the particle interface (Liu et al., 2012; Jagla, 2010).

The findings presented in the current Section 5.2 were submitted for publication by Feldmann et al. (2013b).

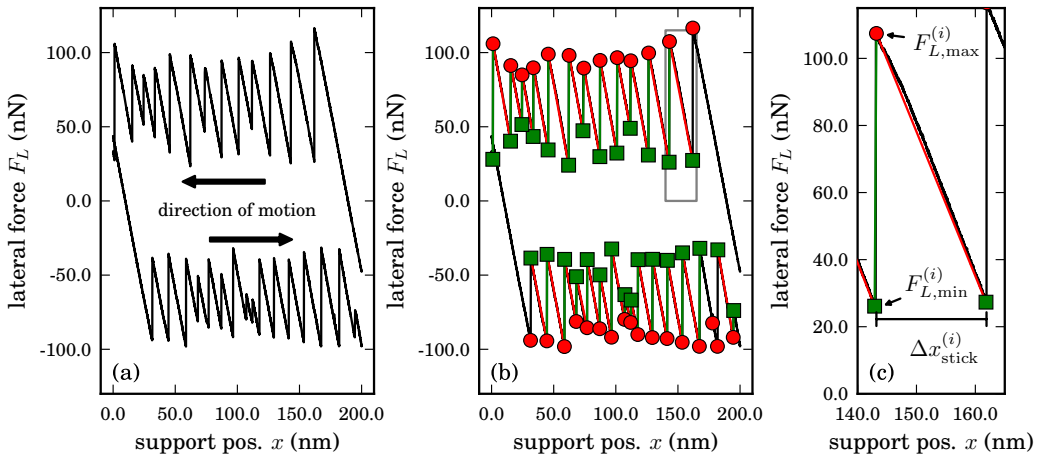

Figure 5.12: Typical stick-slip friction loop of a NP measured with the AFM-SEM instrument. The lateral force signal in (a) exposes characteristic stick-slip motion. Depicted in (b) is the result of the automatic peak and stick-slip detection algorithm. Red circles denote the maxima in $|F_L|$, green squares mark the minima. A sequence of minimum-maximum-minimum peaks is recognized as a single stick-slip sequence (stick phase: red line, slip phase: green line). The initial static friction peak is excluded from subsequent analysis, due to the ill-defined hold time. At the position x=180 nm in the lower trace, two consecutive minima were found, and, consequently, these peaks were not considered as a valid stick-slip event (no red/green markings). In (c), stick-slip event i enlarged, as corresponding to the grey-framed segment in (b). The stick distance $\Delta x^{(i)}_{\text{stick}}$, the maximum lateral force at the end of the stick phase $F^{(i)}_{L,\max}$, and the minimum lateral force after the slip $F^{(i)}_{L,\min}$ are marked.

5.3 Stick-Slip Friction in NP Translation

Stick-slip type movement is of fundamental interest in frictional systems. While the TA-CA model used to explain the findings in the previous chapter is based on stick-slip dynamics, actual stick-slip motion was not resolved in that experiment. By using the data acquisition system implemented at the UHV-AFM-SEM (Section 3.5.5), it was possible for the first time to reliably observe friction traces with stick-slip-type motion. An exemplary friction loop is shown in Fig. 5.12a. This high resolution in time allowed not only to evaluate the mean kinetic friction F_F, but also identify the individual stick and slip events, and to gain a deeper understanding of the contact ageing process governing the friction in this NP system.

All measurements presented in this section were performed in TOS mode

with real-time SEM particle monitoring. Thus, reference measurements were necessary, since the measurement signal reflects the friction induced by both manipulated particle and AFM tip. For the measurements performed for this work, it was found that the tip-substrate friction was smaller than 0.4 nN at all times. This value is more than a factor of 10 lower than the smallest observed friction with attached particles, and thus was neglected in the following analysis (compare also Fig. 5.6 for temperature- and velocity- dependent reference measurements of typical tip-HOPG friction). For the direct tip-substrate contact no static friction peaks were observed, confirming similar findings by Li et al. (2011) on HOPG. This fact indicates that no significant contact ageing has occurred between tip and substrate within the observed experimental parameter range, and that the contact dynamics between tip and sample are fundamentally different from the particle-substrate dynamics.

To analyze a statistically significant number of stick-slip events, a computer routine was devised to automatically detect and quantify the stick-slip event characteristics. For the detection of the maxima and minima a moving-window scheme was implemented, in which the local extremum was identified. The center of the data windows was then shifted to the new extremum. If the center value remained to represent the current local extremum, it was selected as a peak. In the interest to filter out high frequency noise, the width of the window was selected as the number of data points equal to 5 Å or 5 ms, whichever included more points. A number of manual spot tests confirmed the accuracy of the stick-slip detection.

Of the successfully located extrema, sequences consisting of minimum-maximum-minimum of the absolute friction were considered as valid individual stick-slip events. Figure 5.12b shows the extrema and stick-slip events as detected by this algorithm for a single friction loop. It should be noted that this algorithm always discards the first friction maximum. For the automated analysis this is to be desired, since the first friction peak corresponds to the static friction, and is a result of the hold time prior to the recording of the friction loop. In Fig. 5.12c a single detected stick-slip event is plotted. The time elapsed between a lateral force minimum and the successive maximum corresponds to the hold time t_{ht} of the stick-slip event. It is related to the stick length $\Delta x_{\mathrm{stick}}$ and the support velocity v through the equation $t_{\mathrm{ht}} = \Delta x_{\mathrm{stick}}/v$. The value at the lateral force maximum is denoted as $F_{L,\mathrm{max}}$, while the subsequent minimum lateral force value is marked as $F_{L,\mathrm{min}}$.

For measurements at the maximum sampling frequency of $f_{\mathrm{sampling}} = 10\,\mathrm{kHz}$, damped oscillations in the force signal immediately after the slip were found, as shown in Fig. 5.13. This so-called *ringdown* effect carries information regarding

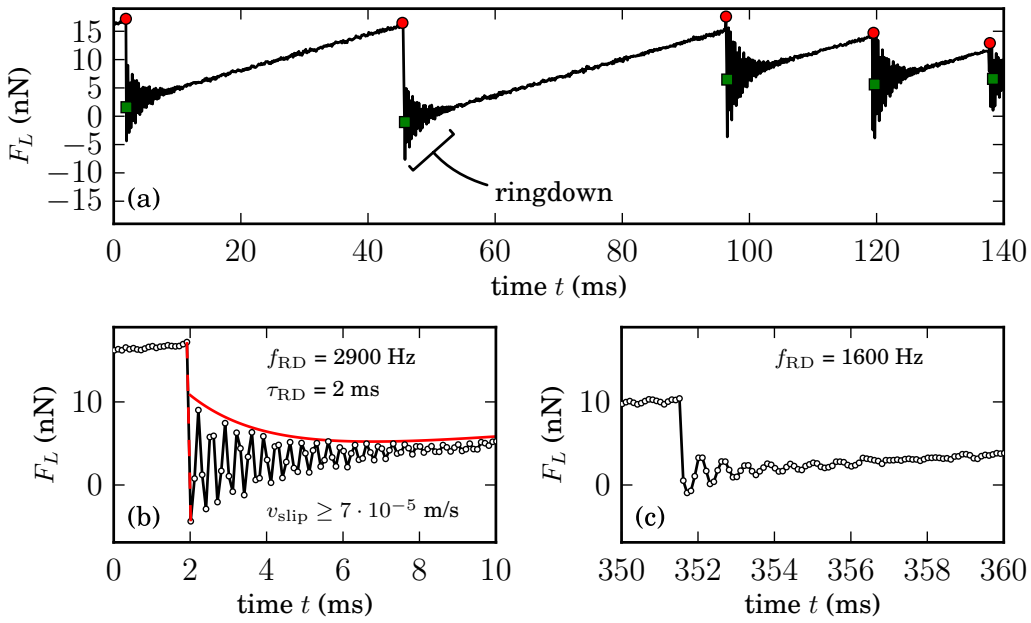

Figure 5.13: Ringdown effect observed in NP stick-slip traces. (a) For traces recorded with high temporal resolution ($f_{\text{sampling}} = 10\,\text{kHz}$), a damped oscillation (*ringdown*) after the individual slip events was observed. Red and green markers show the algorithmically determined maxima and minima, after the ringdown was filtered out. (b) The hull of the oscillation curves exhibits an exponential decay with a typical time constant of $\tau_{\text{RD}} = 2\,\text{ms}$. The measured ringdown frequency f_{RD} is not constant for different slip events, e.g. within a single trace it can vary from $f_{\text{RD}} = 2.9\,\text{kHz}$ down to (c) $f_{\text{RD}} = 1.6\,\text{kHz}$. Furthermore, it can be noted that the ratio of the jump-force amplitude and the initial ringdown amplitude vary significantly. For the stick-slip detection algorithm the ringdown was filtered out by small-window averaging over a small number of oscillation cycles. Note that the slip occurs faster than the sampling time constant $1/f_{\text{sampling}}$=0.1 ms, resulting in a slip velocity of $v_{\text{slip}} \geq 7 \times 10^{-5}\,\text{m/s}$.

the energy dissipation channels (Klein, 2007). Specifically, the ratio between $|F_{L,\max} - F_{L,\min}|$ and initial ringdown amplitude can be related to the ratio of energy dissipated during the slip and the residual transfer of energy at the sticking point. In this measurement, events without measurable dissipation, with partial dissipation, and with nearly full dissipation during the slip phase were registered.

The identity of the physical system performing these damped ringdown oscillations is not evident. It cannot correspond to sliding oscillations of the particle relative to the substrate around the position of rest, $F_L = 0\,\mathrm{nN}$, since the initial part of most oscillation curves is not centered around $F_L = 0\,\mathrm{nN}$. Furthermore, the local mean of the lateral force starts to increase even before the oscillation is completely damped, hinting at the formation of a stable particle-substrate contact before the oscillation is damped out. More plausible candidates are lateral-mode oscillations of the cantilever, although the oscillation mode cannot be conclusively identified. Shear oscillations of the particle itself might contribute to the oscillatory motion.

The variation in frequency, as shown in Fig. 5.13b-c, suggests that the coupling between tip and particle or substrate is of importance for the oscillating system, since this is the only non-invariant parameter between events with differing oscillation frequencies. The typical time constant observed for the exponential decay τ_{RD} is approximately 2 ms, equivalent to a damping of $\eta/M = 1 \times 10^3\,\mathrm{Hz}$.

Furthermore, the slope of the slip curve allows to extract a lower boundary for the mean slip velocity, resulting in $v_{\mathrm{slip}} > 7 \times 10^{-5}\,\mathrm{m/s}$ for the shown friction trace. Since the slip time is shorter than the sampling time, no exact value for v_{slip} can be determined for the NP system in this specific measurement setup.

5.3.1 Direct Observation of NP Contact Ageing

The observation of nanoparticle stick-slip friction allows to investigate of the ageing of NP friction more directly than by measuring the mean friction as demonstrated in Section 5.2. In Section 5.1, the limits of very short hold times ($t_{\mathrm{ht}} < 25\,\mathrm{ms}$ during the tip turnaround) and long hold times ($t_{\mathrm{ht}} > 10\,\mathrm{min}$ between reruns of the measurement procedure) were probed. The intermediate regime can be accessed by recording stick-slip friction traces at different velocities. Figure 5.14 depicts a histogram of the attained hold times over the range of realized support velocities.

The results of contact ageing studies through stick-slip analysis for four individual particles B1–B4 are depicted in Fig. 5.15. While the individual values of the lateral force maxima $F_{L,\max}$ scatter considerably, the high number

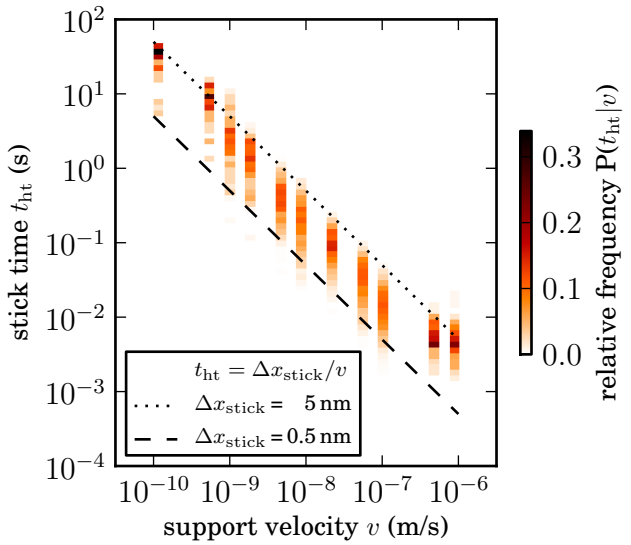

Figure 5.14: Relative frequency of the attained NP stick time t_{ht} depending on the support velocity v. The graph shows that through variation of the support velocity a large range of stick times can be probed. Stick time and support velocity are in first approximation inversely proportional, as denoted by the dashed and dotted lines, corresponding to stick lengths of 0.5 nm and 5 nm, respectively. Thus, velocity-variation of stick-slip friction measurements is a feasible means to conduct contact ageing studies. The chosen velocity values spanning from 10^{-10} m/s to 10^{-6} m/s result in a continuous coverage of the hold time range from 10^{-3} s to over 10^{1} s. At v=10^{-6} m/s the corresponding values of t_{ht} begin to approach τ_{RD}, which limits valid stick-slip detection, and results in a slight skew in the presented data towards longer hold times.

of data points allows for averaging with reasonably small statistical errors.

An unambiguous increase of $F_{L,max}$ is evident for all four NPs, thus confirming the existence of contact ageing in this sample system. The measured data coincides to a high degree with the fit of a logarithmic function given as

$$F_{L,max} = a + b \cdot \ln(t_{ht}/c + 1). \tag{5.9}$$

This kind of logarithmic ageing function has been reported previously by a number of authors for macroscopic and mesoscopic friction, as described in Section 2.5. It is most often attributed to an increase of the real contact area with time.

The parameter a in Eq. (5.9) denotes the instantaneous friction, while parameter b describes the relative peak increase with hold time, and parameter

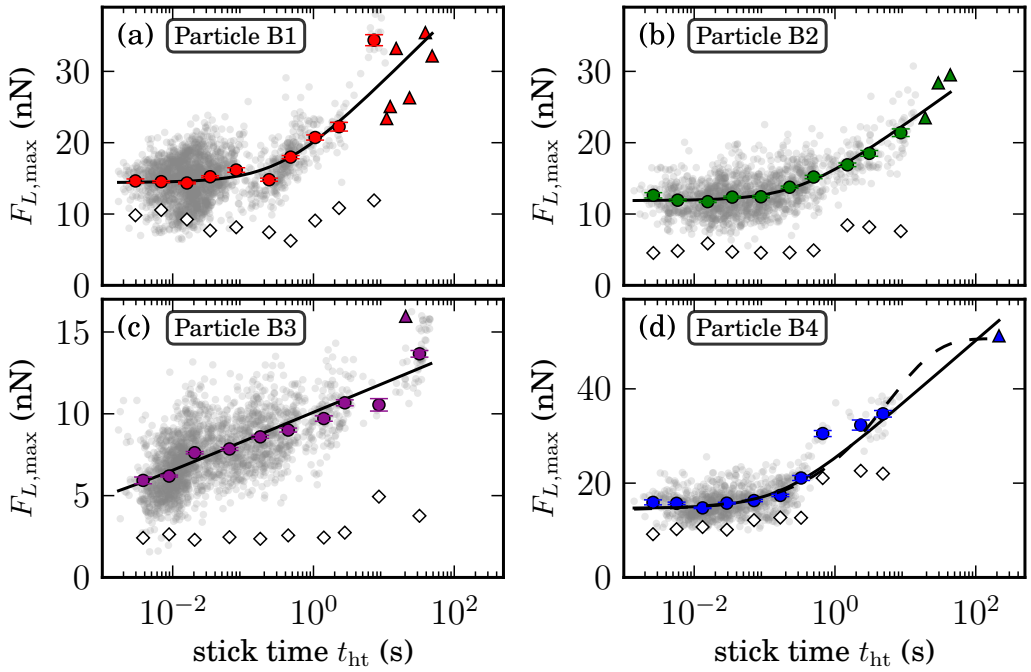

Figure 5.15: Contact ageing of four different NPs, extracted from stick-slip friction data. The lateral force maxima $F_{L,\max}$ are plotted against the associated hold times t_{ht}. Grey dots represent individual stick-slip events, while the colored circles represent averaged $F_{L,\max}$ values for 10 time intervals, complemented by standard error bars. White diamond markers show the corresponding mean post-slip minima $F_{L,\min}$. Triangles denote static friction peaks, recorded after the particle was kept stationary for a longer time and analyzed manually. A logarithmic ageing law according to Eq. (5.9) was fitted to the data (solid black lines). For particle B4, an additional fit was made with a decay-like ageing law similar to Eq. (5.2) (dashed black line). The total number of stick-slip events registered for particles B1–B4 were 2070, 1466, 2112, and 918, respectively.

c is a measure of the hold time at which the increase begins. More precisely, $b \cdot \ln(10)/a$ is a measure for the friction increase, relative to the instantaneous friction a, per decade of the hold time. The parameter c denotes the time, at which the friction is increased by $b \cdot \ln(2)$. Table 5.1 summarizes the parameters found for fitting Eq. (5.9) to the experimental data. It has to be noted that thermal activation contributes to the overall process due to the measurements being performed at room temperature, which will in general reduce the observed ageing effect.

A fit with an exponential decay-like function proportional to $(1-\exp(-t_{\mathrm{ht}}/c))$ (see Fig. 5.15d, dashed line), as it was used for the energy barrier in Eq. (5.2), appears to fit the data just as plausible as a fit attained with Eq. (5.9). Since no clearly identifiable upper boundary for the friction at long hold times was found, a fit using the former function type would be underdetermined, and was thus discarded.

Table 5.1: Parameters obtained by fitting Eq. (5.9) to the data shown in Fig. 5.15.

	a (nN)	b (nN)	c (s)	b/a
Particle B1	14.48 ± 0.08	4.1 ± 0.2	0.35 ± 0.05	0.29 ± 0.02
Particle B2	11.88 ± 0.09	3.1 ± 0.2	0.31 ± 0.05	0.26 ± 0.02
Particle B3	$4 \pm 2^{*}$	0.77 ± 0.03	$(4 \pm 10)\times 10^{-4*}$	$0.2 \pm 0.1^{*}$
Particle B4	14.7 ± 0.1	5.6 ± 0.2	0.17 ± 0.02	0.38 ± 0.02

* For particle B3, parameters a and c cannot be reliably determined, since no plateau is observed in Fig. 5.15c.

A definitive attribution of which physical process is responsible for the observed contact ageing phenomenon is difficult. As described in Section 2.5, plausible candidates for its origin are the plastic flow of the particle material, resulting in an increase of the atomic contact area with time, or delayed formation of interface bonds, or phase changes of a boundary lubrication layer. Brndiar et al. (2011b) have performed density functional theory calculations of Sb/HOPG systems, where the influence of adatoms onto the energy landscape is considered. They concluded that adatoms can be responsible for making the otherwise incommensurate interfaces quasi-commensurate, resulting in linear scaling of friction with contact area. Since this type of scaling appears to correspond to the particles used for the experiment presented here (see Section 5.4), this boundary lubrication layer is expected to play a mayor role in the interface dynamics.

For plastic flow at room temperature in metals, Persson (1998, p. 373) predicts typical time constants c to be of the order 10^{-10} s, which is extremely short compared to the findings in this work. Hence, other effects must dominate the contact ageing in the NP system.

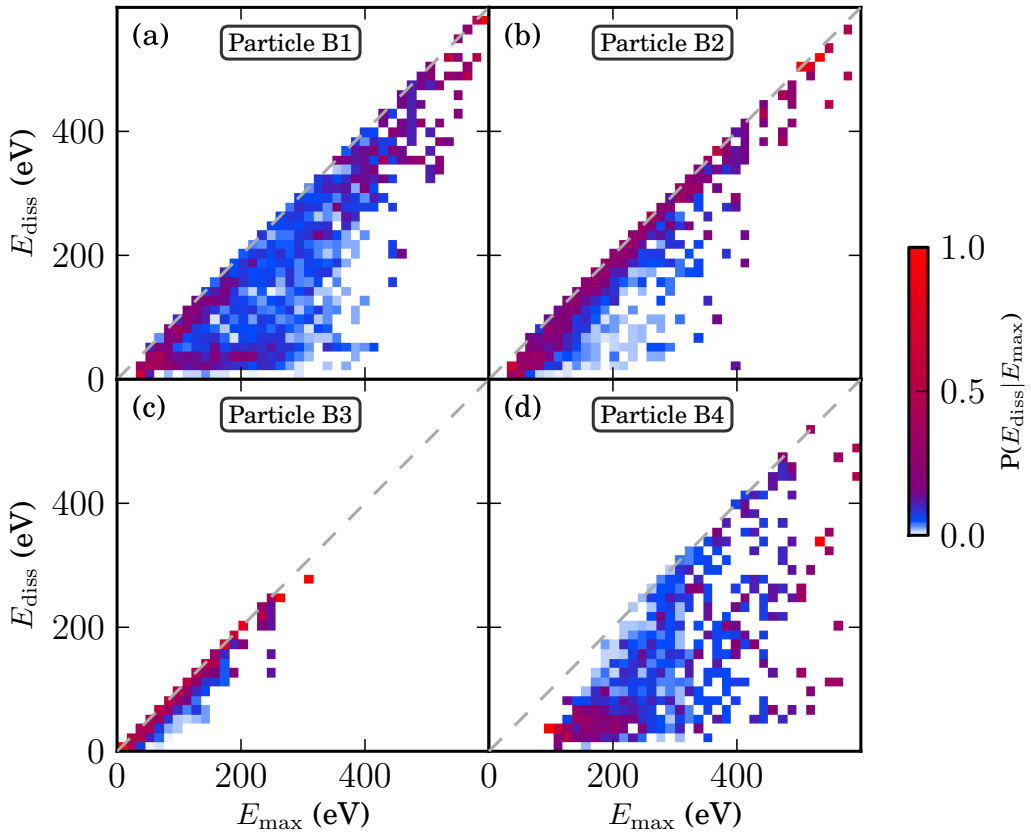

Figure 5.16: Energy dissipated per slip event. The 2D histograms shows the relative frequency P of a slip event exhibiting energy dissipation of E_{diss} after the energy E_{max} was deposited in the cantilever spring during the stick phase. Results for particles B1 - B4 are shown. The dashed grey line represents full energy dissipation per slip. Particle B3 shows a very strong tendency to dissipate all stored energy, whereas the other particles dissipate a smaller portion of the energy per individual slip.

Energy Dissipation

Energy dissipation is of crucial importance in frictional systems. In Fig. 5.16, energy dissipation probabilities are presented. The probability to dissipate a certain amount of energy during the slip event E_{diss}, as measured by the minimum lateral force after the slip, depends on the energy stored in the cantilever at the lateral force maximum E_{max}. In these diagrams, a disparity between particle B3 and the other particles can be observed, which may be

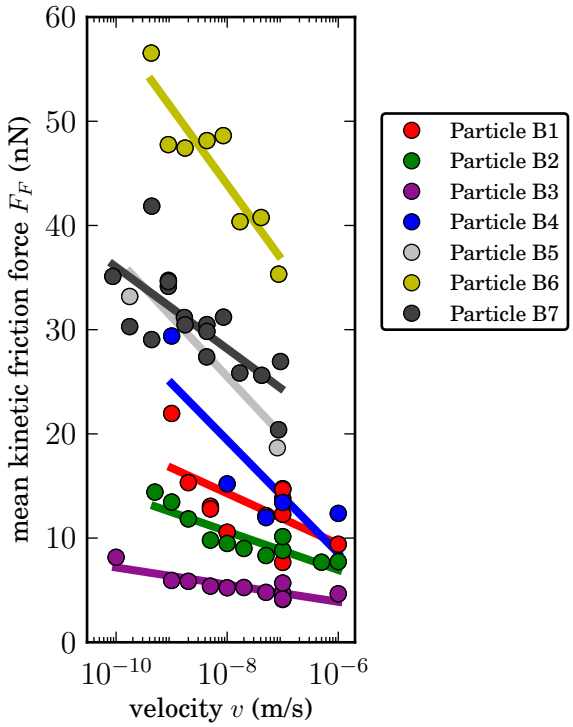

Figure 5.17: Kinetic friction F_F plotted against velocity v for seven particles B1–B7 at room temperature. Markers represent averaged mean kinetic friction values at different temperatures, while lines correspond to fits linear in $\ln(v)$. For particles B1, B2 and B4, friction appears to decrease more strongly with increasing velocity for small velocities than for high velocities, which can be explained by the friction plateau for low hold times found in Fig. 5.15.

related to the distinct contact ageing found in Fig. 5.15. While for particle B3 the stored energy is dissipated almost completely in most events, the other particles show a much stronger variation of the dissipated energy. For particle B2, maxima in the probability distribution correspond to almost full dissipation, but features considerable deviation towards lower dissipation. For particle B1 and B4, the dissipation probability is distributed almost evenly over the full range of complete to negligible dissipation. This might indicate that particle B3 dissipates energy by a mechanism fundamentally different as compared to particle B1 or B4. One plausible candidate for this distinction is the presence or absence of interface contamination.

Velocity Dependence of Mean Friction

In order to relate the results of the measurement presented here to the findings of Section 5.2, the mean friction at different velocities for a number of particles is plotted in Fig. 5.17. All manipulated particles exhibit velocity weakening, to varying degrees of intensity. As laid out in Section 5.2, this result is to be expected for dominant contact ageing and again validates the model

assumptions used in Section 5.2.3. In Section 5.2, no distinct dependence of the mean friction on velocity at room temperature was observed. Furthermore, friction traces before and after a number of manipulations were compared to exclude wear effects. Within the uncertainty of the measurement no systematic change was found after 20 consecutive manipulations, which is consistent with the absence of wear observed in Sections 5.1 and 5.2.

Since the stick-slip friction measurements presented in this section were performed at room temperature, it has to be noted that a considerable amount of thermal activation and thus premature slip can be expected, causing jumps before the local energy minimum in which the particle resides actually vanishes. Thus, the observed contact ageing is actually convoluted with the effect of thermal activation, which has to be kept in mind when interpreting the results. Nonetheless, contact ageing is the dominating effect within the probed time scales at room temperature, since otherwise thermal activation would cause a deviation towards decreasing friction at longer hold times, which was not observed.

Stick-Slip Jump Distances and Force Amplitudes

Typical atomic scale friction measurements on crystals often yield periodic stick-slip friction with slip lengths corresponding to lattice parameters (as in Fig. 4.10c; cf. (Schirmeisen et al., 2005)). For the NP-based system, however, no such slip lengths dominated by the substrate lattice were observed. In particular, the lattice periodicity of HOPG with b_{HOPG}=2.46 Å (see Section 4.6.1) did not emerge from the data, as demonstrated in Fig. 5.18a. This finding hints at the existence of stable interface configurations with considerably shorter wavelength as compared to the wavelength of individual surfaces, since no discretization peaks can be observed in Fig. 5.18a. Structural lubricity (Section 2.4) or adsorbates in the interface can be responsible for this phenomenon.

The observed maximum likelihood stick length of $\Delta x_{\mathrm{stick}} \approx 1.5\,\mathrm{nm}$ corresponds to six times the separation b_{HOPG} of the hollow sites in HOPG. Within the framework of the PT model, this may be explained by postulating surface potential corrugations, which are strong compared to the cantilever potential. In combination with sufficiently slow energy dissipation this would lead to slips over multiple energy minima at once.

Interestingly, the distribution of pre-slip forces $F_{L,\mathrm{max}}$ varies decisively between different particles (see Fig. 5.18b), while the distributions of the stick lengths $\Delta x_{\mathrm{stick}}$ mostly overlap. A reasonable explanation for the uniform distribution of $\Delta x_{\mathrm{stick}}$ might be given by the fact that the energy dissipation is

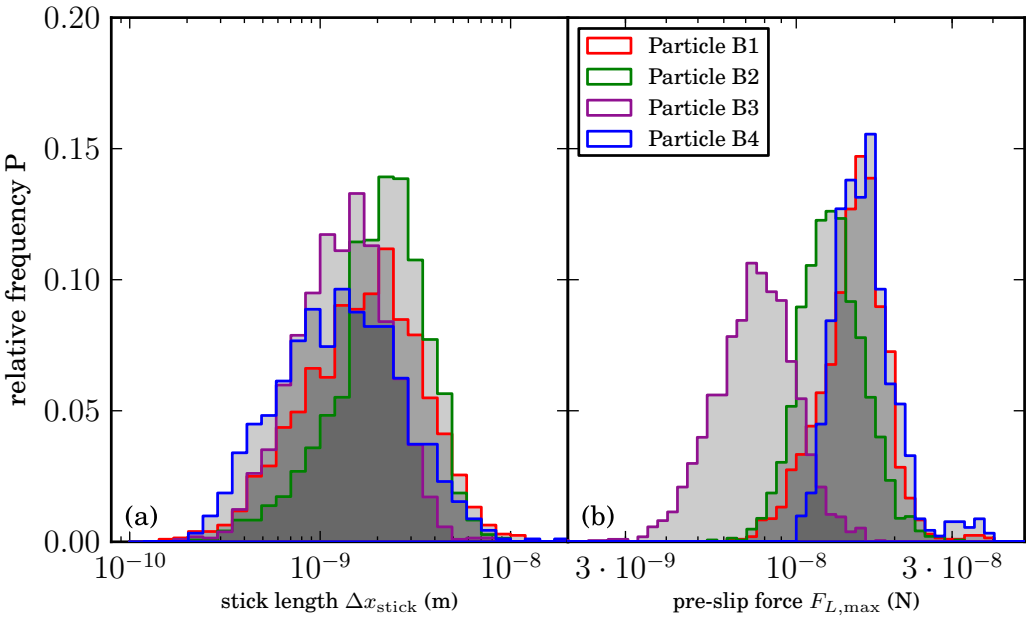

Figure 5.18: Relative frequencies P of stick- and slip-characteristics. (a) Histogram of the stick lengths $\Delta x_{\mathrm{stick}}$ for different particles B1–B4. Mean and variance are similar for all four particles. (b) Histogram of the pre-slip maximum forces $F_{L,\mathrm{max}}$ for particles B1–B4, showing significant variations in the mean force.

dominated by dissipation channels through the sensors. For all four measurements the same cantilever was used. To clarify this matter, further experiments with different sensors are necessary.

Figure 5.19 compares histograms of the lateral force maxima $F_{L,\mathrm{max}}$ prior to the slip phase and the post-slip lateral force minima $F_{L,\mathrm{min}}$ for five different brackets of velocities. Both quantities are normally distributed in first approximation. The means of both Gaussians shift to higher values of F_L for decreasing velocities. While this is to be expected for $F_{L,\mathrm{max}}$ due to contact ageing, the reason for the shift of $F_{L,\mathrm{min}}$ is not immediately clear. As mentioned in the discussion of Fig. 5.16, the available dissipation channels might restrict the amount of dissipated energy, thus disallowing complete cantilever relaxation. Similar results were found for particles B2-B4.

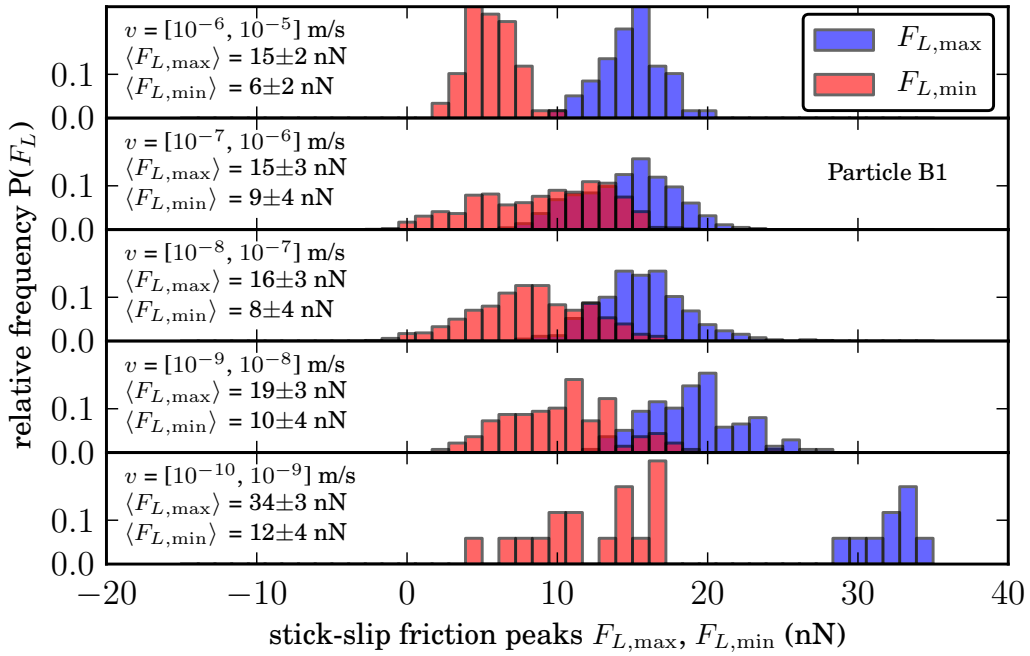

Figure 5.19: Histogram of the relative frequencies P of pre-slip lateral force $F_{L,\max}$ and post-slip lateral force $F_{L,\min}$ for the particle B1 in different velocity ranges. In the lowest velocity range only very few events were registered. The displayed numerical values for F_L are given as the mean and the standard deviation of the individual distributions. In the interval with the smallest velocities, the small number of observed events results in a discontinuous histogram representation.

Growth of Additional Clusters

The preparation procedure for the Sb nanoparticles inside the AFM-SEM system yielded samples with NPs of mean size as well as sample coverage well within the desired parameter ranges. But when the resulting sample was inspected in more detail, using a stiff non-contact AFM cantilever in frequency modulation mode, smaller clusters in-between the Sb particles were observed (Fig. 5.20). These clusters were not found after sample preparations at the other utilized AFM systems. The origin of the growth of these clusters could not be fully clarified. The most plausible explanation is that they consist of antimony, like the larger particles, but are a result of a different growth mode. Kaiser et al. (2002) have reported two different growth modes within the same sample preparation of Sb on HOPG, which differ in their respective heights.

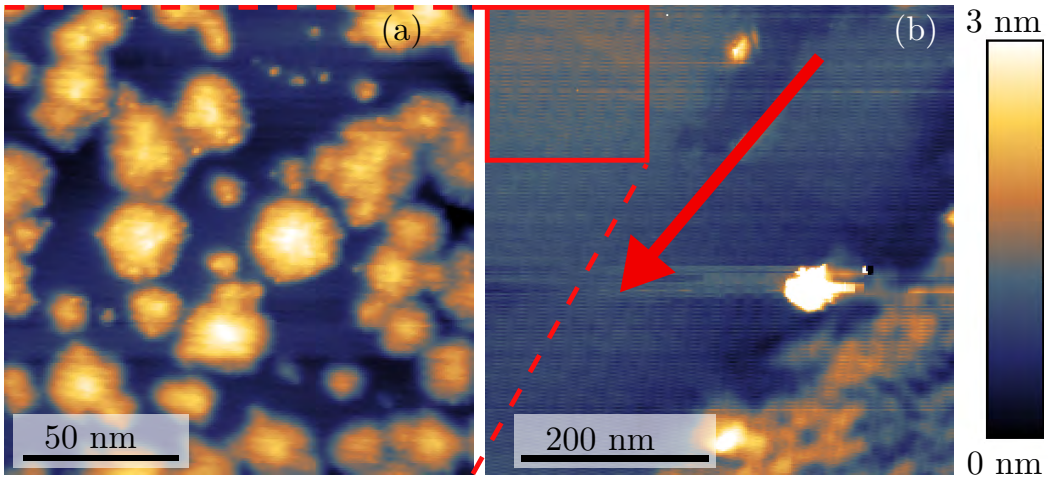

Figure 5.20: Smaller clusters between the Sb particles, imaged in NC mode. (a) Additional clusters were observed on the substrate immediately after Sb evaporation, located between the larger Sb NPs that were used for the manipulation experiments. The typical height of 2 nm is a factor of 10 smaller than typical values for the larger NPs. The area shown in (b) includes the same region as shown in (a), after a large NP has been pushed across the surface, along the path marked by the red arrow. The adsorbates appear to have been pushed away almost completely. The remaining adsorbates at the lower right did not lie within the particle pathway.

Another conceivable explanation is the contamination of the evaporator with a second substance, but this seems unlikely, considering the thorough cleaning of the crucible prior to loading with high purity antimony.

Whatever the origin of the formation of these clusters was, they were easily moved out of the way when a large particle was translated across their initial location, as demonstrated in Fig. 5.20b. Thus, their influence on repeated manipulations, which were performed along the same pathway, can be considered minuscule. But it is conceivable that in this preparation adatoms were present in the Sb particle-substrate interface. The clusters could not be observed with neither the SEM nor in contact mode with the AFM.

Concluding Remarks regarding NP Contact Ageing Measurement

This section gave an overview regarding the investigation of contact ageing in NP-based sample systems using stick-slip characteristics. A logarithmic increase of maximum friction $F_{L,\max}$ with hold time t_{ht} could be demonstrated for four different particles, as well as a velocity weakening. Particle B3 showed

qualitative differences in its contact age dependence, in particular the absence of a plateau for small hold times. The stick lengths do not seem to reflect the substrate periodicity. Additional adsorbate islands were found on the substrate, which could be removed by a single NP manipulation event. A condensed report regarding the findings in this section is currently in preparation (Feldmann et al., 2013a).

5.4 Contact Area Scaling of NP Friction

In the previous sections, the focus was set on investigating the characteristic changes in friction for the individual NPs, as parameters such as velocity, temperature and hold time were varied. But the differences in friction between different particles have not been discussed thoroughly. The central quantity, which discriminates between the individual particles, is the size of their contact area, which will be addressed in the following section.

As discussed in Section 2.4, the contact area scaling exposes information about the structure of the interfaces. For matching lattice geometries or for uncoupled individual junctions the friction is linear in the contact area. Non-matching lattice configurations with non-zero coupling between junctions lead to power law scaling with sub-linear contact area dependence of friction. In a first step, this section aims at classifying the type of scaling observed for the particles in Sections 5.2 and 5.3. Secondly, the scaling classification will be compared to the ageing and thermal activation characteristics found in those previous sections.

Previous Work

Nanoparticle manipulation is exceptionally well-suited for the investigation of contact area scaling in nanoscale friction, since by manipulating NPs of different sizes a large range of contact sizes is can be easily probed. Initial experiments with an Sb/HOPG sample system, performed by Dietzel et al. (2008), have revealed different scaling law branches with both linear and seemingly no dependence of friction on contact area. Even particles prepared in the same preparation run were found to exhibit either linear scaling or seemingly vanishing friction, which can be explained by the presence or absence of adatoms in the interface (cf. Section 2.4).

Additional experiments performed by Dietzel et al. (2010a) were able to confirm the distinct scaling branches, as depicted in Fig. 5.21. A third friction branch was observed for air-exposed particles, resulting in linear friction scaling, but with a slope ten times more steep as compared to particles in the linear scaling branch kept under UHV conditions. Again, particles showing extremely low friction were found.

The experiments presented in (Dietzel et al., 2008; Dietzel et al., 2010a) have been performed using the RT-UHV-AFM (see Section 3.5.3), which at the time had a rather limited lateral force resolution. In the interest to increase the resolution, the system was equipped with a superluminescent diode, which was

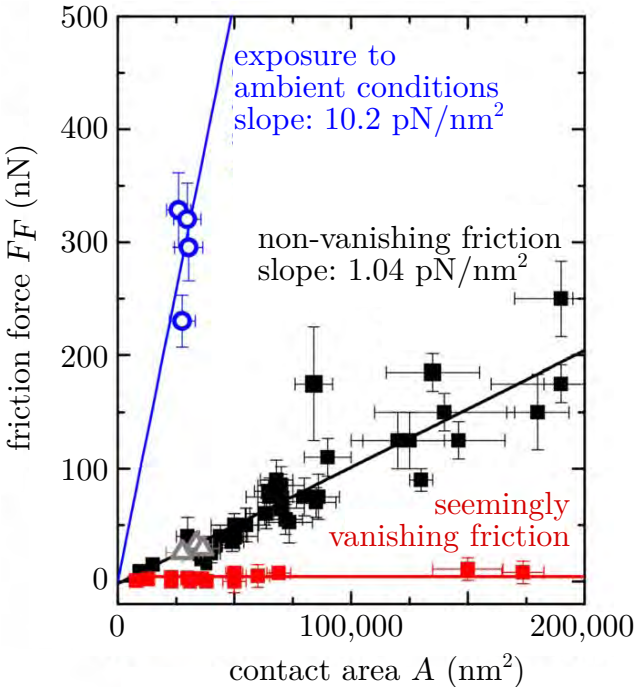

Figure 5.21: Distinct scaling branches of Sb/HOPG friction depending on contact area. Three different scaling branches can be distinguished: particles display a comparatively high friction after exposure to air (blue). Intermediate values of friction with a linear dependence on contact area (black) as well as ultra-low friction (red) were found for particles kept under UHV conditions. Figure adapted from (Dietzel et al., 2010a).

used as the light source for the optical lever force detection. Such diodes deliver high power, but, unlike laser diodes, the emitted light has a low coherence length, thus reducing interference effects at the PSD and increasing the resolution of the measured forces (compare e.g. (Rode et al., 2011)).

In a follow-up study by Dietzel et al. (2013) after the aforementioned instrumental enhancement, the authors were able to quantify the friction of 32 particles found in the ultra-low friction branch. For antimony particles on HOPG, a power law was observed, as it was expected from simulation results (see Section 2.4). The resulting exponent of $\gamma = 0.53 \pm 0.05$ matches the predicted value of 0.5 extremely well.

One attempt of explaining the origin of the three distinct scaling branches for the Sb/HOPG system is discussed in (Brndiar et al., 2011b; Brndiar et al., 2011a). While the sub-linear scaling is believed to result from the sliding of clean and incommensurate contacts (structural lubricity, cf. Section 2.4), the authors find considerably increased energy barriers when a contamination of the interface with water or propane molecules is assumed. The contaminant concentrations, which would be necessary to explain the friction found in the linear branch, are estimated to be approximately one contaminant molecule per $\sim 200\,\mathrm{nm}^2$ if constructive force summation is applied. This appears to be

compatible with ultra high vacuum conditions (Brndiar et al., 2011b). If this assessment is correct, intermediate values for lower contaminant concentrations should be expected. Another proposed origin is a molecular roughness of the interface, in which individual Sb_4 tetrahedra are sticking out of the particle, at a concentration of one molecule per $18\,\mathrm{nm}^2$.

In addition to the experiments performed with round antimony particles, crystalline, triangular gold particles were manipulated. The Au/HOPG sample system gave rise to a power law for the area scaling of friction, but in this case with an exponent of $\gamma = 0.33 \pm 0.15$. This value matches the expected value of $\gamma = 0.25$, which follows from the consideration that for non-matching crystalline lattices only the number of rim atoms is significant for the overall friction (Dietzel et al., 2013).

Area Scaling of NPs from Contact Ageing Experiments

For the classification of the particles used in the manipulation experiments presented in Sections 5.2 and 5.3 with regard to their contact area dependence, the measured friction at constant velocity $v = 100\,\mathrm{nm/s}$ and constant temperature $T = 300\,\mathrm{K}$ was considered. Friction and contact area for the manipulated particles are presented in Fig. 5.22, along with the sub-linear and the lower linear scaling laws found in (Dietzel et al., 2010a; Dietzel et al., 2013).

The plot reveals that the measured data coincides very well with the previously found scaling laws. In particular, the particles investigated for Section 5.2 conform well to the sub-linear scaling branch, suggesting that the interfaces were indeed uncontaminated.

A different picture emerges for the particles studied in Section 5.3. While particles B2 and B3 clearly match the superlubric scaling branch, the other particles show significantly higher friction as would be expected for superlubricity. A possible explanation is the contamination of the interface of these particles with adatoms, thus leading to a linear scaling of friction with contact area. The inter-particle contamination shown in Section 5.3.1 strongly supports this interpretation.

Interestingly, this observation might be connected with the distinct contact ageing observed for particle B3, compared to the other particles (see Fig. 5.15), and to the difference in the energy dissipation shown in Fig. 5.16. Additional experiments are needed to render this bi-fold classification definite.

Whether a particle exhibits superlubric sliding or not furthermore appears to influence the velocity dependence of friction. While the non-superlubric particles B5-B7 exhibit very strong velocity weakening (Fig. 5.17), the super-

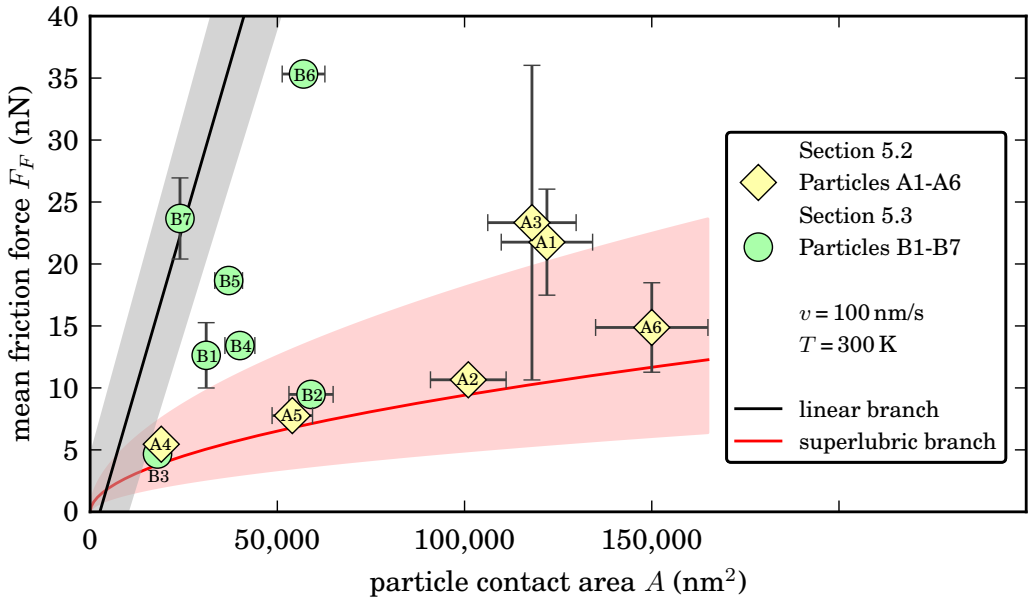

Figure 5.22: Contact area dependence of friction for all manipulated particles in Section 5.2 and Section 5.3 with $v = 100\,\mathrm{nm/s}$ and $T = 300\,\mathrm{K}$. The black and red lines correspond to the intermediate linear branch shown in Fig. 5.21 (black marker) and the ultra-low friction branch (red marker) as quantified in (Dietzel et al., 2013), respectively. The filled areas reflect the uncertainties found in (Dietzel et al., 2010a; Dietzel et al., 2013), while the error bars represent an estimated relative measurement error of the contact size of 10 %, as well as one standard deviation of the friction force signals.

lubric particles A1–A4 expose almost no velocity dependence at $T = 300\,\mathrm{K}$. Since both contact ageing and thermal activation are crucial for the overall velocity dependence, it follows that for non-superlubric particles contact ageing dominates the effects of premature unbinding due to thermal activation, while for superlubric particles these effects for the most part cancel each other out.

6 Ageing in AFM Tip-Sample Contacts

While the experiments using the Sb/HOPG sample system in Chapter 5 exposed friction and contact ageing in van-der-Waals-bonded interfaces, other forms of inter-atomic bonds in the interface can lead to different forms of contact ageing. In this chapter, contact ageing properties of interfaces with covalent and with metallic bonding at varying temperatures will be discussed.

The investigation of ageing in nanoscale contacts is not limited to nanoparticle manipulation. Although the contact area is not as well defined as with NPs, direct AFM tip-substrate measurements are in general more straight-forward to implement, and can as well provide fundamental insight into the dynamics of frictional contact. In addition, the force required to move large NPs bonded with strong chemical bonds can easily exceed the yield strength of the NPs, rendering friction measurements unfeasible in this case.

In the following, two different kinds of contact ageing in two material combinations under UHV conditions are presented. As an example for a sample system with covalent bonds in the interface, Section 6.1 demonstrates temperature-dependent contact ageing effects between an oxidized silicon wafer and an AFM tip made from the same material. A fundamentally different form of contact ageing can be observed for soft, self-healing metals. In Section 6.2, ageing of gold surfaces sliding against a silicon tip is evaluated, where the shearing of a gold neck dominates the interface dynamics. Furthermore, both material combination are relevant for the construction of micro electro-mechanical system (MEMS) (Maboudian et al., 2004; Rezvanian et al., 2007). Due to the large surface-to-volume ratio, the effects of friction and wear are critical factors in the design of MEMS.

6.1 Ageing in Stationary Contacts of SiO_2 Surfaces

The existence of nanoscale contact ageing could recently be demonstrated by Li et al. (2011), for contacts consisting of SiO_2 AFM tips on SiO_2 substrates under ambient conditions at room temperature and at varying levels of humidity. Significant fractions of the contact ageing effect they report have to be attributed to capillary water condensation, whereas the extent of contribution of capillary condensation to the overall contact ageing is not evident. Measurements under more well-defined conditions are required to quantify the contribution of the inter-body bonds to the dry friction. Initial, indirect evidence for contact ageing under UHV was presented by Barel et al. (2010a), where the authors used the MK model to explain velocity weakening in silica-silica friction. However, the existence of nanoscale contact ageing under vacuum conditions could only recently be demonstrated directly, through observations of a hold time-dependent increase in friction, within the context of this work (cf. Section 5.3.1). In this section, similar hold time-dependent friction measurements are presented for the first time for SiO_2 contacts under UHV conditions. These measurements were conducted at different temperatures as to gain insights into the thermal activation in this particular case of covalently bonded interfaces.

6.1.1 Experimental Procedure: Slide-Hold-Slide Method

Contact ageing experiments have been performed with SiO_2 tips on SiO_2 in UHV at temperatures between 30 K and 293 K. The general measurement protocol was similar to the one described by Li et al. (2011): The tip was first brought into contact with the sample (normal load $F_N = 140\,\mathrm{nN}$). Subsequently, the tip was displaced (*slide*) in $+x$ direction (velocity $v{=}1.0 \times 10^{-5}\,\mathrm{m/s}$; distance $\Delta x = 100\,\mathrm{nm}$). After this step, the relative movement was halted for a specific amount of time, the hold time t_{ht} (*hold*), after which the tip translation was resumed (*slide*). This procedure was repeated in $-x$ direction, as to obtain full friction loops. This type of experiment is known as a *slide-hold-slide* (SHS) or *stop-and-go* experiment (Li et al., 2011; Baumberger et al., 2006).

Compared to the statistical approach chosen in Section 5.3, where stick-slip traces at different velocities were evaluated to extract hold time and force peaks, the SHS method is applicable even for systems where no stick-slip is observed, and it allows to directly choose the desired hold time. In order to generate a statistically relevant number of events, many measurement cycles have to be

conducted, since each SHS friction loop only yields two lateral force maxima.

Experimental Parameters

These experiments were carried out using the VT-UHV-AFM (Section 3.5.4). SHS cycles were performed at different temperatures T (in order of realization: 293 K, 100 K, 293 K, 30 K, 50 K, 40 K, 80 K, 200 K, 293 K). For each temperature, SHS cycles with hold times t_{ht} between 1×10^{-3} s and 1×10^{1} s were recorded. To limit the influence of wear effects, multiple cycles were recorded successively. All kinetic friction measurements were performed at a velocity of v=10 µm/s and a normal force of F_N=1.4×10^{-7} N, which is very similar to the adhesion between tip and substrate of 1.3×10^{-7} N, as measured at the beginning of the experiment. The force calibration was conducted according to Section 3.4.3.

The sample consisted of Si(111) with an intact native oxide layer. It was loaded into the vacuum chamber and heated to 190 °C for 90 min to remove adsorbates. A surface roughness of 0.18 nm RMS for a $100 \times 100\,\mathrm{nm}^2$ sample spot was measured. Due to technical reasons, the experiment had to be performed at a base pressure of $p = 5.0 \times 10^{-9}$ mbar, which is slightly higher than for the experiments shown previously. After a new sensor was inserted into the system, an initial run-in of the tip consisting of ≈ 1000 friction loops of 200 nm length was performed. This run-in is necessary to attain stable tip configurations, which otherwise is prone to wear.

6.1.2 Stationary Contact Ageing Results

Figure 6.1 shows an example of a typical SHS friction loop obtained from a single cycle. While the mean friction during both slide phases within one direction are mostly constant, the stopping in the hold phase for a duration of t_{ht} yields a static friction peak F_S at the beginning of the second slide phase. The friction recorded during the hold phase was monitored for additional, uncontrolled slip events to rule out significant drift effects during the hold phase, which would alter the actual hold time. No stick-slip was found in this particular kinetic friction trace, but could be registered for increased absolute kinetic friction at low temperatures.

A significant increase in the lateral force signal F_L as well as stick-slip friction showing increasing mean values with time were observed at cryogenic temperatures, which is depicted in Fig. 6.2. Such tilted stick-slip curves are commonly found in wear and plastic deformation experiments (Gnecco et

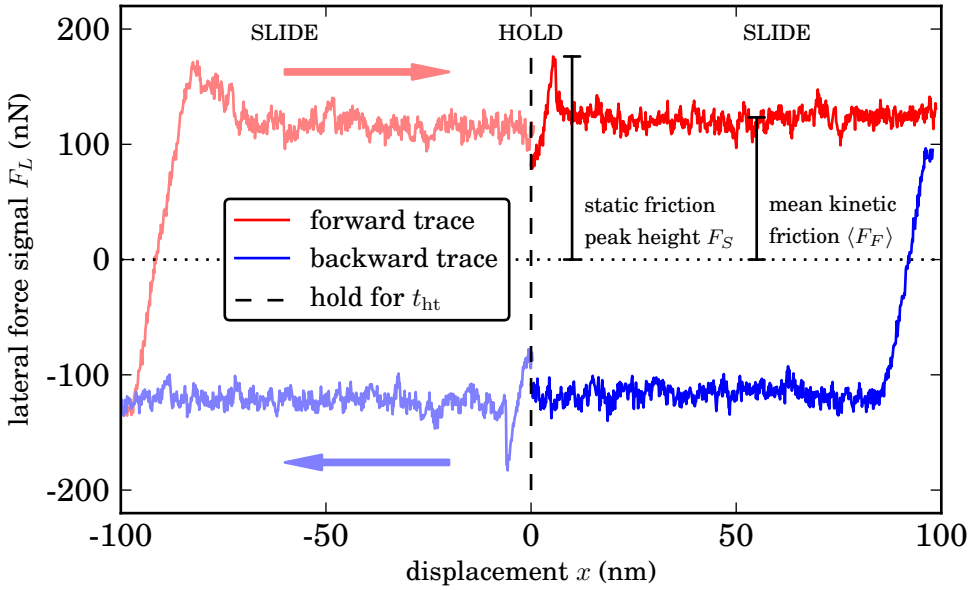

Figure 6.1: Typical friction loop for an SHS cycle at $T = 293\,\mathrm{K}$. The contact was kept stationary at position $x = 0\,\mathrm{nm}$ during a hold time of $t_{\mathrm{ht}} = 3.0\,\mathrm{s}$, resulting in a static friction peak F_S at the beginning of the following trace. After the static friction is overcome, an almost constant signal level F_F is observed, corresponding to the kinetic friction. The recording of a forward and a backward trace allows to calculate the reference level as the mean of both traces excluding the initial static friction ramps.

al., 2002; Gosvami et al., 2011). All traces similarly showing non-constant kinetic friction levels were excluded from quantitative analysis, which effectively ruled out all measurements at $50\,\mathrm{K} < T < 293\,\mathrm{K}$. Further discussions of this observation are given below.

Discussion: Ageing Results

The measured dependency of the static friction force F_S on hold time t_{ht} is shown in Fig. 6.3. The result can be very well approximated by a logarithmic fit of the form

$$F_S = a + b \cdot \ln(t_{\mathrm{ht}}/c + 1). \tag{6.1}$$

which has already been employed to fit the data presented in Section 5.3.1 and can be motivated by considering gradually increasing contact areas (cf.

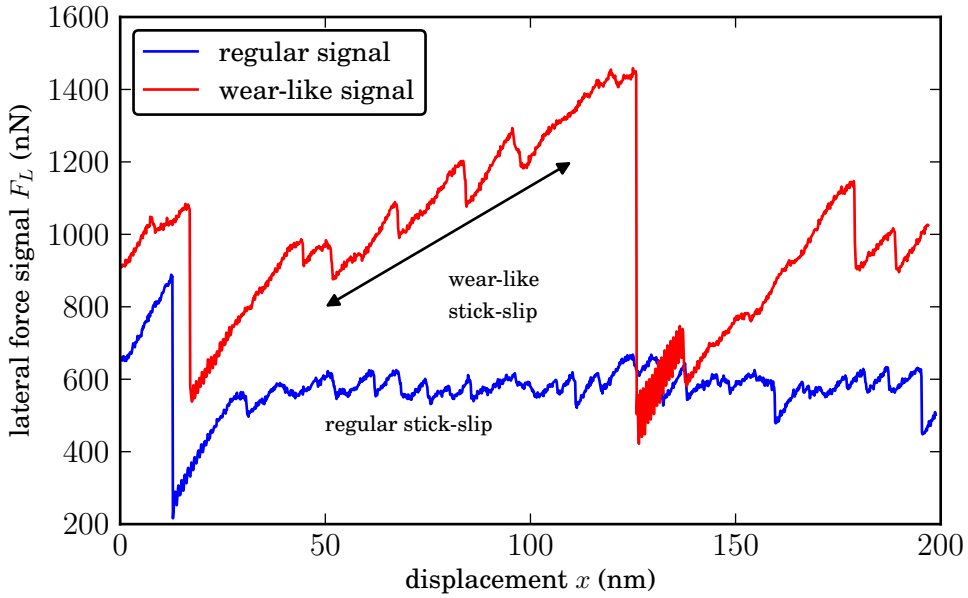

Figure 6.2: Comparison of regular friction signal and wear-like friction signal at $T = 80\,\mathrm{K}$. The normal signal features a static friction peak as well as stick-slip friction during the kinetic friction phase. The wear-like friction signal shows significantly increased friction. In the kinetic friction phase, stick-slip friction with the signal mean increasing with displacement is registered, which is typical for wear. The wear-like signal was recorded 17 min after the regular signal at the same sample position and same normal force. Changing the sample position or pulling the tip away from the sample did not reliably regenerate the friction signal at 80 K.

Eq. (2.16)). The parameter a corresponds to the friction at $t_{\mathrm{ht}} = 0\,\mathrm{s}$, while b describes the steepness of the logarithmic increase, and c quantifies the time scale of the onset of aging. A normalized measure for the temporal increase of friction, independent of absolute friction levels, can be given as b/a. The values of the fit coefficients are given in Table 6.1.

Equation (6.1) also fits the data reported by Li et al. (2011) (in air at 60 % humidity and room temperature) very well. The parameters a and c cannot be extracted from their presented data with reasonably good certainty, since no plateau at low hold times was observed within the measurement range. But it appears appropriate to assume the parameter a to lie in a range between the kinetic friction force and the lowest measured static friction peak, resulting in fit parameters of $c = (0.3 \pm 0.6)\,\mathrm{s}$ and $b/a = 0.7 \pm 0.1$. While

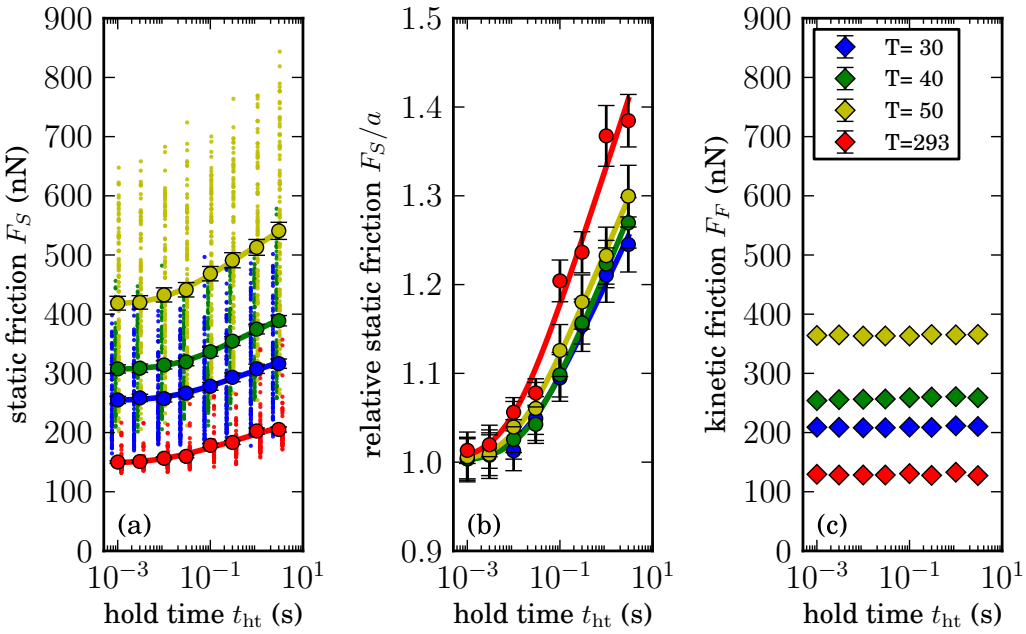

Figure 6.3: Increase of static friction peak height F_S with hold time t_{ht}. (a) shows the distribution of absolute peak heights (small dot markers; minor offset in t_{ht} added for clarity) as well as averaged absolute peak heights (circle markers) at each hold time. In (b) averaged peak heights with standard errors are shown, normalized by the value of F_S in the limit of $t_{ht} \to 0$, corresponding to parameter a in Eq. (6.1). At all temperatures a logarithmic increase of the static friction with the hold time can be identified. Corresponding fits with Eq. (6.1) are plotted as solid lines. (c) The associated kinetic friction F_F does not depend on hold time, supporting the validity of the recorded data. A total of 2862 individual static friction peaks were evaluated.

the relative increment of friction b/a is two orders of magnitude larger than what is reported in Table 6.1, the uncertainty of the time constant c prohibits meaningful comparison. Also, note that the mean kinetic friction of $\approx 80\,\mathrm{nN}$ reported by Li et al. (2011) is of the same order as the data found in Fig. 6.3.

This finding suggests that the main contribution to contact ageing reported in (Li et al., 2011) is indeed caused by capillary condensation, resulting in a water meniscus and associated capillary forces, while for the measurements under vacuum conditions presented here no such condensation could have taken place. It follows that even in the absence of capillary forces logarithmic frictional contact ageing is observed in point-like silica contacts, which, to the authors knowledge, has not been demonstrated before.

Table 6.1: Fit parameters obtained by matching Eq. (6.1) to the experimental contact ageing data presented in Fig. 6.3

T (K)	a (nN)	b (nN)	c (s)	b/a
30	254 ± 2	12 ± 1	$(1.5 \pm 0.6)\times10^{-2}$	$(4.8 \pm 0.4)\times10^{-2}$
40	306 ± 1	16.8 ± 0.8	$(2.0 \pm 0.5)\times10^{-2}$	$(5.5 \pm 0.3)\times10^{-2}$
50	416 ± 2	22 ± 1	$(1.1 \pm 0.3)\times10^{-2}$	$(5.3 \pm 0.3)\times10^{-2}$
293	148 ± 4	10 ± 1	$(8 \pm 7)\times10^{-3}$	$(7 \pm 1)\times10^{-2}$

While the absolute static friction peak heights and the mean friction force vary significantly with temperature (Fig. 6.3a,c), the ageing curves normalized by a at different temperatures appear as very similar (Fig. 6.3b). For thermally activated plastic flow, and in assuming a increase of contact area as the origin of the frictional increase, a dependence of $b/a \propto \mathrm{k_B}T/\Delta E_{\mathrm{plastic}}$ would be expected (Persson, 1998, p. 343). Such a proportionality in T is not observed in this experiment, although a weak increase with T can be detected. It thus seems unlikely that interface creep is the origin of the observed aging process in silica contacts. A continuous relaxation of the force signal towards lower lateral forces was in some instances detected during the hold phases, which signifies lateral creep of the interfaces.

When compared to the values determined in Section 5.3.1, it is found that both parameters c and b/a are two orders of magnitude lower for SiO_2-SiO_2 ageing than what is observed for the Sb/HOPG sample system in Section 5.3.1. Consequently, in the silica contact, the ageing processes appear to set in earlier, but also to progress slower after the onset.

MD simulation results presented by Liu et al. (2012) show a logarithmic increase of the bond concentration of a silica contact, which coincides very well with the general logarithmic increase reported here. In particular, the observed timescales c are in good agreement with the reported onset of aging effects, which in most cases they found to be of the order 10^{-2} s. Comparing the parameters a and b is not as straightforward, since in their simulation the bond concentration can approach zero even for moderately short hold times. This seems to not correspond well to the actual physical system, since it would imply zero friction for $t \to 0$, when only covalent interaction is considered. A more quantitative comparison would be possible if the upper saturation limit could be detected in the experiment, which the MD simulation predicts to be at hold times larger than 10^4 s. This would require to maintain a constant tip-sample contact for hours, which is rather difficult due to drift effects. But by using

nanoparticles this approach appears viable: NPs can be kept in stationary contact with the substrate while the tip is retracted from the particles, and can be located again even after days of resting.

Discussion: Origin of Wear-Like Friction Traces

The observation of wear-like friction traces that were excluded from the previous analysis, as shown in Fig. 6.2, indicate the occurrence of surface modifications. This becomes even more apparent when the evolution in mean kinetic friction F_F is considered: F_F first gradually increased from 80 nN to 121 nN at $T = 293\,\mathrm{K}$ before the cooling cycle, and then dropped to 23.7 nN after the measurement cycle. While the initial trend could be expected due to blunting of the tip and, consequently, an increase in contact area, the subsequent decrease of friction is more obscure. A plausible explanation for this observation is that, due to the wear during the high-friction state at low temperatures, the native oxide layer of the tip is worn away, exposing the underlying silicon and thus changing the frictional properties of the system permanently. Run-in experiments reported by Chen et al. (2013) with SiO_2 micro-spheres attached to an AFM tip worn against a silicon wafer covered with a native oxide layer (typical thickness of 2 nm in air) showed a drastic decrease of friction with wear distance. They also report distorted friction loops, similar to the wear-like friction traces found in this experiment, which are attributed to wearing of the SiO_2 layer of the substrate. Li et al. (2011) also reported significant run-in effects for AFM tip-sample contacts consisting of SiO_2. In this experiment, however, wear-like traces in general corresponded to increased friction levels.

The contact could not be reset to low friction by performing a tip pull-off, as it was the case for the gold sample system described in Section 6.2. Relocating the tip to a different sample location also brought no rejuvenation of the contact. Consequently, the contact change cannot result from a local wear scar on the substrate. But regular friction traces could be measured again, after the wear-like friction traces were first observed at 100 K, by heating the sample to room temperature. This finding implies that adsorbates were responsible for significant fractions of the detected change in friction. The reduction of the normal force did not have a significant effect on the lateral force, which hints at strong blunting of the tip.

An additional source of uncertainty is introduced by the temperature of the contact. The exact value cannot be quantified due to the limitation of the construction of the VT-AFM system, which allows only cooling of the sample, while the sensor remains at room temperature (Section 3.5.4).

The mean kinetic friction F_F exhibits a peak at T=50 K (cf. Fig. 6.3c), similar to what was reported by Barel et al. (2010b). Since the dataset for T=50 K was recorded in between those for T=30 K and T=40 K, this peak cannot simply result from increasing contact contamination, and thus underlines the validity of the measured data.

To conclude, the results at low temperatures have to be interpreted with care due to the discarded wear-like traces. At room temperature, however, no wear-like friction traces were observed. Thus, the corresponding ageing results at $T = 293$ K can be considered as very cogent.

Proposed Improvements of the Experimental Procedure

To further pinpoint the properties of the observed ageing process, additional measurements under more defined conditions would be helpful. First, the base pressure of the UHV chamber has to be significantly improved in order to rule out the possibility of adsorbate condensation at low temperatures. Furthermore, the temperature at the interface should be determined more precisely. This can be achieved by cooling the whole AFM head assembly instead of just cooling the sample, or by using nanoparticles with enhanced thermal coupling to the substrate.

Since wear effects appear as significant in this experiment, steps have to be taken to reduce or control them. For this experiment, moderate normal loads were chosen in order increase the chance of observing contact ageing, which resulted in lateral force values of the same order as found in (Li et al., 2011). A reduction of normal load could be a first step in trying to reduce wear.

In addition, materials of more invariable composition and higher wear resistance could be employed for further experiments. For the silicon substrate this can be achieved either by removing the native oxide through sputtering, or by increasing the oxide thickness by tempering, resulting in more homogeneous Si or SiO_2 surfaces (Lee, 2006) and invariant surface chemistry. Similarly, the tip can be sputtered to remove the outer layer of SiO_2. Alternatively, entirely different tip materials with higher wear resistance like diamond-like carbon could be employed.

6.2 Ageing in Sliding Contacts of Au Surfaces

In the preceding parts of this work the term 'contact ageing' has been used to denote time-dependent changes of interaction strength in stationary contacts. But under certain conditions even sheared contacts of solids can undergo time-dependent changes. In particular, in the work of Gosvami et al. (2011) it was observed that soft metals like gold can form mobile capillary metal necks within asperity contacts. This leads to ageing effects in the sheared junctions, which substantially influence the friction and adhesion of the interface, in combination with a strong, nonlinear temperature dependence.

For this experiment, Au(111) surfaces were prepared by thermal evaporation of Au films with a thickness of $\sim 300\,\mathrm{nm}$ onto mica substrates, and consecutively annealed with a butane flame under ambient conditions (Gosvami et al., 2010). The VT-UHV-AFM system was used for the AFM measurements, operating at a base pressure of $p < 2 \times 10^{-10}\,\mathrm{mbar}$. After loading the samples into the system, they were heated to temperatures of above 200 °C for 1 h to remove residual traces of water. All experiments were carried out at constant normal loads of $F_N < 5.0\,\mathrm{nN}$. The typical herringbone surface reconstruction of Au(111) was successfully resolved. Friction measurements were performed at temperatures between 30 K and 300 K, spanning a velocity range of between 20 nm/s and 3000 nm/s.

6.2.1 Contact Ageing Results during Translatory Movement

For measurements at temperatures of $T \geq 170\,\mathrm{K}$, friction traces were observed, which exhibited atomic stick-slip features, but were otherwise not varying significantly with time. Velocity-dependent measurements exhibited velocity strengthening behaviour, as it is expected within the TA-PT model.

At $T < 170\,\mathrm{K}$, however, the results changed drastically. Specifically, the friction traces became time-dependent, with the friction force increasing over time as shown in Fig. 6.4. Friction could be reset to low values by pulling the tip out of contact for a short time. The corresponding adhesion was high when high friction values were measured previously, and low adhesion arose for low values of friction.

This observation can be explained by slow growth of a gold junction between tip and substrate. This interpretation is supported by the shape of the friction traces before and after pulling the tip out of contact, as shown in Fig. 6.5a,b. The traces recorded before pull-off show considerable distortion, commonly found in wear experiments caused by plastic deformations of the contact. Traces

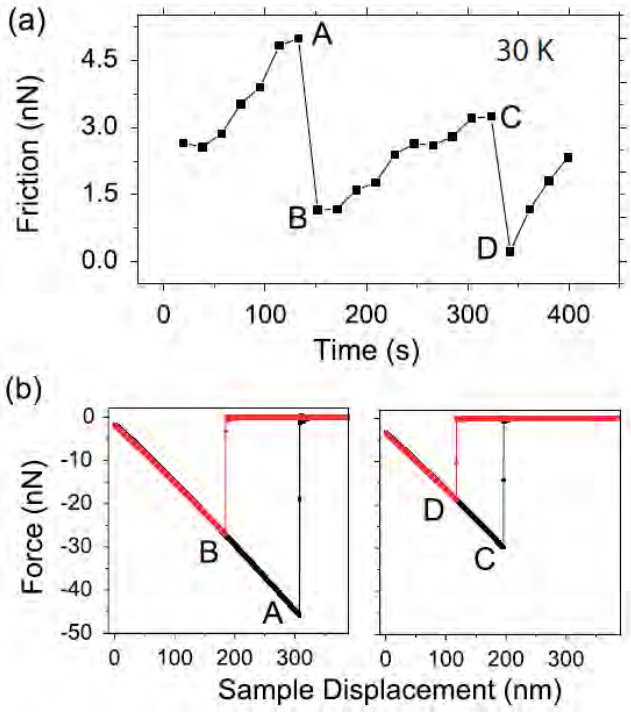

Figure 6.4: Time dependence of friction on Au at low temperatures. (a) shows the time evolution of a typical friction trace at T=30 K. The tip was pulled out of contact at the four positions A-D, which resulted in a resetting of friction to low values. In (b) the corresponding force-distance curves are shown. Immediately after high friction values were registered (A, C), the adhesion was significantly larger than after low friction measurements (B, D). Adapted from Gosvami et al. (2011).

acquired immediately after pull-off appear mostly undistorted, similar to the results obtained at all times for temperatures above 170 K.

In order to interpret these results, MD simulations have been conducted. Modeling the interaction between a SiO_2 tip and Au, as used in the experiment, would be rather difficult due to complex interaction potentials. Instead, the interaction between an Au(111) surface and an Au(111) tip as well as between a Ni(111) tip and an Au(111) surface were modeled. These two material combinations represent a gold neck and a 'clean' tip-sample contact, respectively. Details of the simulation procedure can be found in (Gosvami et al., 2011).

The resulting friction traces are in very good qualitative agreement with the measurements, as shown in Fig. 6.5c-d. Snapshots of the atomic structure found in the simulation, as depicted in Fig. 6.5e-f, illuminate the origin of the

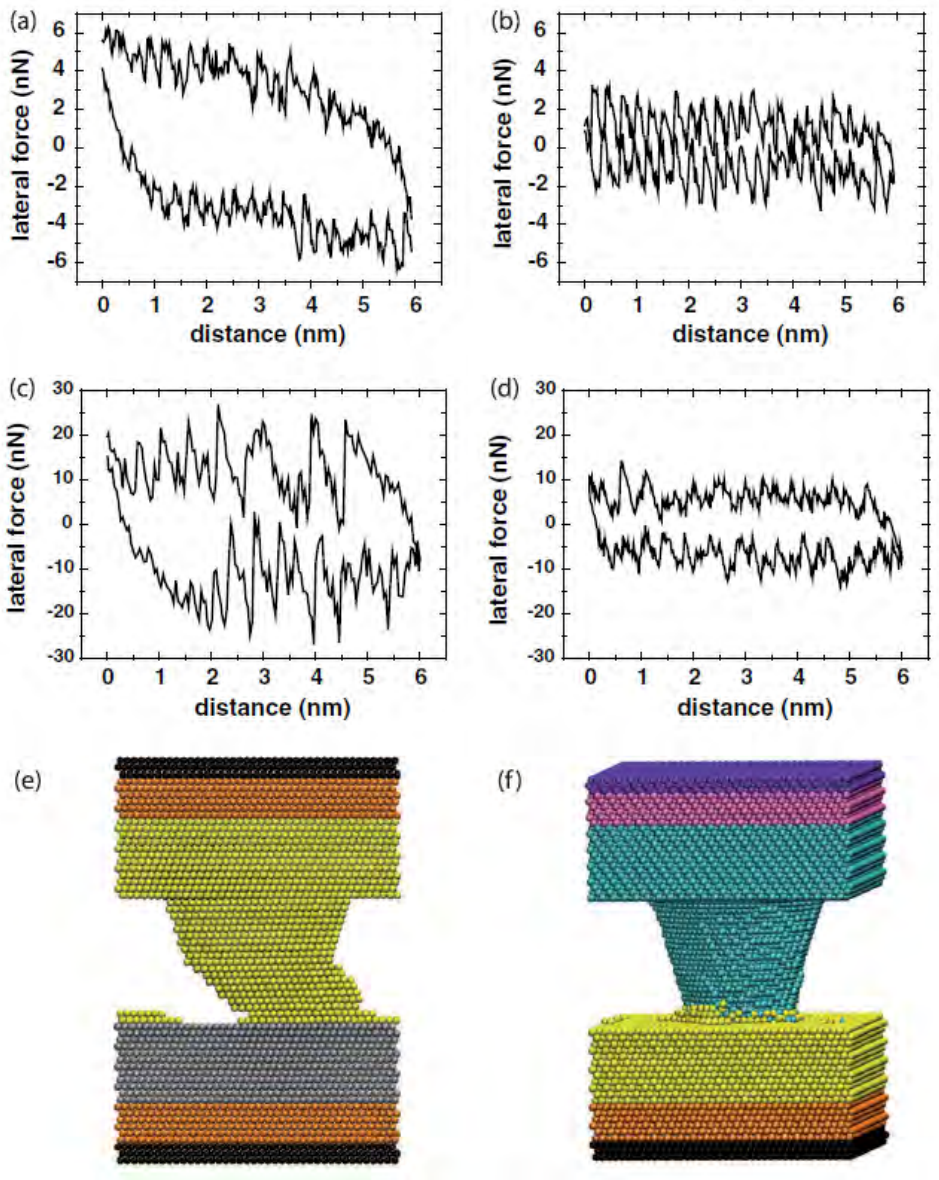

Figure 6.5: Tip on Au friction. Friction loop (a) was recorded before the tip was pulled off from the surface in Fig. 6.4, and (b) was recorded afterwards. MD simulation results are depicted for (c) sliding an Au(111) tip over an Au(111) surface, and (d) sliding a Ni(111) tip over Au(111). The corresponding simulated atomic geometry snapshots exhibit (e) plastic deformation for the Au on Au contact, and (f) limited pick-up of Au atoms at the Ni tip. Adapted from Gosvami et al. (2011).

bend friction traces: the gold neck is plastically deformed during commensurate sliding. When a Ni tip is used instead, similar characteristic behaviour is not observed due to the stronger bond of the Ni atoms. This simulation exposes stick-slip movement with atomic lattice periodicity, despite non-matching atomic lattices of Ni and Au. It was found that a layer of Au is formed at the Ni tip, thus resulting in commensurate sliding of the Au layer on the Au substrate. Thus, for both high and low temperatures, the actual shear displacement occurs between Au layers, where metallic bonds govern the shearing process.

While the friction of the investigated model system is dominated by the Au neck formation at $T < 170\,\mathrm{K}$, measurements at higher temperatures do not show this characteristic ageing effect. A plausible explanation for this finding is the faster contact regeneration due to fast diffusion of Au atoms at elevated temperatures. Continuous imaging of nanoscale scratches on Au(111) exposes, that these scratches disappear over time (Gosvami et al., 2011). This finding suggests that the Au surface can effectively be healed by atomic diffusion at high temperatures. Thus, the gold neck appears to be in a dynamic equilibrium, where wear damage of the neck is quickly regenerated and, consequently, no ageing effects are observed.

The evidence for such plastic deformation and quick relaxation processes at gold surfaces are of high interest also for Au NP friction. Au NPs translated over HOPG substrates exhibit sub-linear contact area scaling of friction at room temperature due to structural lubricity (Dietzel et al., 2013). It would be highly illuminating to study the dependence of contact area scaling on temperature, since relaxation effects, and thus contact ageing, could be able to suppress structural lubricity (cf. Section 2.4).

7 Summary and Outlook

The focus of this work was set on establishing nanoparticle (NP) manipulation techniques for the investigation of frictional properties of NPs, and on applying these methods to unveil thermal activation characteristics and contact ageing phenomena in antimony NPs on graphite substrates under vacuum conditions. Furthermore, the contact ageing properties of two instances of point-like nanoscale contacts with covalent and metallic bonding were examined.

An introduction to the field of nanotribology is given in Chapter 2. This chapter provides a (very) short historical background of friction measurements. Interface models and concepts which are prerequisite in order to gaining insight into fundamental processes in nanoscale friction are laid out. The atomic force microscope, which is an invaluable tool for nanoscale friction experiments, is described in detail in Chapter 3. Different modes of operation and force calibration methods are presented. Furthermore, the actual microscopy systems used in this work are introduced. A number of methodological techniques for NP manipulation were implemented and refined for this work, which are detailed in Chapter 4. In particular, the so-called *tip-on-top* and *tip-on-side* modes of manipulation, with topography imaging in non-contact mode and particle translation in contact mode, as well as real-time monitored manipulations using a combined AFM-SEM, were made available for highly controlled NP friction experimentation. The concrete experimental model system that was used in this work is discussed at the end of this chapter: Sb particles prepared onto HOPG substrates.

Systematic studies of NP friction are presented in Chapter 5. The dependence of NP friction on temperature and velocity was investigated, and a complex time-temperature interdependence could be demonstrated. A model based on the concept of *contact ageing* was devised, which takes into account the increase of friction with the duration of stationary contact between NP and substrate. While no direct proof of the existence of contact ageing in this system was initially available, a significant distinction between static and kinetic friction could be observed in a series of dedicated experiments. Accompanying computer simulations based on the contact aging model were successfully fitted to the experimental data, exposing contact ageing and thermal activation as central

factors governing friction in this model system.

Additional manipulation experiments with enhanced temporal resolution unveiled stick-slip-type dynamics in the NP interface. Systematic variation of the sliding velocity allowed to regulate the hold times during the stick phases. This enabled the direct observation of the time-dependent increase in static friction due to contact ageing. Computer-aided statistical evaluations of the stick-slip friction traces revealed a logarithmic ageing law, which is consistent with observations of macroscale and mesoscale contact ageing. The identification of the underlying interface dynamics, which are responsible for this contact ageing phenomenon in atomically flat interfaces, remains challenging. Measurements regarding the contact area dependence of particle friction yielded different branches of distinct scaling laws. The origin of this distinction is described by the concept of structural lubricity.

Complementary measurements of friction between direct tip-substrate contacts were carried out to investigate contact ageing properties of SiO_2 and Au(111) substrates in contact with SiO_2 tips, which is shown in Chapter 6. The SiO_2 contacts, which are dominated by covalent siloxane bonds, conformed to a logarithmic contact ageing law depending on the stationary hold time of the tip, qualitatively similar to the contact ageing observed for NPs. For gold, however, another type of contact ageing was found. In this case, the *sliding* contact showed time-dependent evolution of friction at low temperatures, similar to wear processes. This effect could be attributed to the plastic deformation of gold junctions between tip and substrate. At high temperatures no time-dependence was detected as a consequence of rapid regeneration of the gold neck by thermally assisted migration of Au atoms.

In conclusion, the results presented in this work underline the fundamental importance of contact ageing phenomena in nanotribology, as exemplified for the three investigated sample systems, and help to establish the technique of friction measurement through nanoparticle manipulation as a versatile tool for future nanotribological studies.

Outlook

While the existence of ageing in nanoscale contacts and its impact on stick-slip dynamics could successfully be demonstrated, the actual interface dynamics leading to contact ageing are not thoroughly understood. Further experiments with materials of varying yield strengths and elastic stiffnesses could shed light at the role of plastic and elastic deformation, while the use of material combinations with well-studied bonding mechanisms could provide insight into

delayed chemical bonding at interfaces. For example, experiments regarding the interdependence of contact ageing, contact area scaling and temperature dependence in Au particles on HOPG substrates promise insights into the relaxation dynamics at the Au-HOPG interface. Surveying contacts at different contact pressures and contact areas as well as varying levels of adsorbate contamination promises further opportunities for the characterization of ageing dynamics, since the findings in this work already hint at a disparity between superlubric and non-superlubric contact ageing. The long-term saturation of contact ageing in nanoscale contacts is another issue of considerable interest.

List of Figures

List of Tables

Bibliography

Albrecht, T. R., P. Grütter, D. Horne, and D. Rugar (1991): *Frequency modulation detection using high-Q cantilevers for enhanced force microscope sensitivity.* Journal of Applied Physics, **69**:2, 668 doi: 10.1063/1.347347 (cited on page 32)

Amontons, G. (1699) Mem. Acad. R. Sci. 206 (cited on page 6)

Anton, R. and I. Schneidereit (1998): *In situ TEM investigations of dendritic growth of Au particles on HOPG.* Physical Review B, **58**:20, 874–881 doi: 10.1103/PhysRevB.58.13874 (cited on page 66)

Armstrong-Helouvry, B., P. Dupont, and C. Canudas De Wit (1994): *A survey of models, analysis tools and compensation methods for the control of machines with friction.* Automatica, **30**:7, 1083–1138 doi: 10.1016/0005-1098(94)90209-7 (cited on page 78)

Aymerich, F. M. and A. Delunas (1975): *On the explosive semiconductor-semimetal transition of antimony.* Physica Status Solidi (a), **31**:1, 165–170 doi: 10.1002/pssa.2210310118 (cited on page 62)

Barel, I., M. Urbakh, L. Jansen, and A. Schirmeisen (2010a): *Multibond Dynamics of Nanoscale Friction : The Role of Temperature.* Physical Review Letters, **104**:6, 066104 doi: 10.1103/PhysRevLett.104.066104 (cited on pages 12–14, 76, 77, 81, 106)

Barel, I., M. Urbakh, L. Jansen, and A. Schirmeisen (2010b): *Temperature Dependence of Friction at the Nanoscale : When the Unexpected Turns Normal.* Tribology Letters, **39**: 311–319 doi: 10.1007/s11249-010-9675-4 (cited on pages 12, 76, 82, 113)

Barel, I., M. Urbakh, L. Jansen, and A. Schirmeisen (2011): *Unexpected temperature and velocity dependencies of atomic-scale stick-slip friction.*

Physical Review B, **84**:11, 115417 DOI: 10.1103/PhysRevB.84.115417 (cited on page 2)

Barel, I., A. E. Filippov, and M. Urbakh (2012): *Formation and rupture of capillary bridges in atomic scale friction.* The Journal of Chemical Physics, **137**:16, 164706 DOI: 10.1063/1.4762863 (cited on pages 15, 20, 21)

Baumberger, T., P. Berthoud, and C. Caroli (1999): *Physical analysis of the state- and rate-dependent friction law. II. Dynamic friction.* Physical Review B, **60**:6, 3928–3939 DOI: 10.1103/PhysRevB.60.3928 (cited on page 18)

Baumberger, T. and C. Caroli (2006): *Solid friction from stick-slip down to pinning and aging.* Advances in Physics, **55**:3-4, 279–348 DOI: 10.1080/00018730600732186 (cited on pages 15, 18, 67, 77, 106)

Berthoud, P., T. Baumberger, and N. Supe (1999): *Physical analysis of the state- and rate-dependent friction law :* Physical Review B, **59**:22, 313–327 (cited on page 19)

Bhushan, B. (2004): *Springer Handbook of Nanotechnology.* ed. by B. Bhushan 1st Springer-Verlag Berlin ISBN: 3-540-01218-4 (cited on pages 27, 29, 32, 35, 55, 57)

Binnig, G. and H. Rohrer (1982): *Scanning tunneling microscopy Scanning tunneling microscopy.* Helvetica Physica Acta, **55**:6, 726–735 DOI: 10.5169/seals-115309 (cited on page 25)

Binnig, G., C. F. Quate, and C. Gerber (1986): *Atomic Force Microscope.* Physical Review Letters, **56**:9, 930–933 DOI: 10.1103/PhysRevLett.56.930 (cited on pages 25, 32)

Bowden, F. P. and L. Leben (1938): *Nature of Sliding and the Analysis of Friction.* Nature, **141**: 691–692 (cited on page 10)

Bowden, F. P. and D. Tabor (1950): *The Friction and Lubrication of Solids.* New York, NY: Oxford University Press Inc. ISBN: 0198507771 (cited on page 15)

Braun, O. M. and J. Röder (2002): *Transition from Stick-Slip to Smooth Sliding: An Earthquakelike Model.* Physical Review Letters, **88**:9, 096102 doi: 10.1103/PhysRevLett.88.096102 (cited on page 78)

Brndiar, J., R. Turanský, and I. Štich (2011a): *Simulation of frictional behavior of Sb nanoparticles on HOPG: Frictional duality and biduality.* Physical Review B, **84**:8, 085449 doi: 10.1103/PhysRevB.84.085449 (cited on pages 60, 101)

Brndiar, J., R. Turanský, D. Dietzel, A. Schirmeisen, and I. Štich (2011b): *Understanding frictional duality and bi-duality: Sb-nanoparticles on HOPG.* Nanotechnology, **22**: 085704 doi: 10.1088/0957-4484/22/8/085704 (cited on pages 60, 92, 101, 102)

Carpick, R. W. (1997): *Scratching the Surface : Fundamental Investigations of Tribology with Atomic Force Microscopy.* Materials Chemistry, **2665**:510 doi: 10.1021/cr960068q (cited on page 22)

Center for Nanotechnology, CeNTech GmbH, Münster, Germany, url: http://centech.de (visited on 08/05/2013) (cited on page 41)

Chambers, A. (2005): *Modern Vacuum Physics.* Boca Raton, Florida, USA: CRC Press LLC (cited on page 40)

Chen, L., S. H. Kim, X. Wang, and L. Qian (2013): *Running-in process of Si-SiO x /SiO2 pair at nanoscale—Sharp drops in friction and wear rate during initial cycles.* Friction, **1**:1, 81–91 doi: 10.1007/s40544-013-0007-1 (cited on page 112)

Chung, D. D. L. (2002): *Review Graphite.* Journal of Materials Science, **37**: 1475–1489 doi: 10.1023/A:1014915307738 (cited on page 61)

Dieterich, J. H. (1978): *Time-dependent friction and the mechanics of stick-slip.* Pure and Applied Geophysics, **116**: 790–806 doi: 10.1007/BF00876539 (cited on pages 18, 78)

Dietzel, D., T. Mönninghoff, L. Jansen, H. Fuchs, C. Ritter, U. D. Schwarz, and A. Schirmeisen (2007): *Interfacial friction obtained by lateral manipulation of nanoparticles using atomic force microscopy techniques.*

Journal of Applied Physics, **102**:8, 084306 DOI: 10.1063/1.2798628 (cited on pages 23, 50, 54, 60)

Dietzel, D., C. Ritter, T. Mönninghoff, H. Fuchs, A. Schirmeisen, and U. D. Schwarz (2008): *Frictional Duality Observed during Nanoparticle Sliding*. Physical Review Letters, **101**:12, 125505 DOI: 10.1103/PhysRevLett.101.125505 (cited on page 100)

Dietzel, D., M. Feldmann, H. Fuchs, U. D. Schwarz, and A. Schirmeisen (2009): *Transition from static to kinetic friction of metallic nanoparticles*. Applied Physics Letters, **95**:5, 053104 DOI: 10.1063/1.3193551 (cited on pages 16, 55, 68)

Dietzel, D., T. Mönninghoff, C. Herding, M. Feldmann, H. Fuchs, B. Stegemann, C. Ritter, U. D. Schwarz, and A. Schirmeisen (2010a): *Frictional duality of metallic nanoparticles: Influence of particle morphology, orientation, and air exposure*. Physical Review B, Copyright (2010) by the American Physical Society, **82**:3, 035401 DOI: 10.1103/PhysRevB.82.035401 (cited on pages 63, 100–103)

Dietzel, D., M. Feldmann, C. Herding, U. D. Schwarz, and A. Schirmeisen (2010b): *Quantifying Pathways and Friction of Nanoparticles During Controlled Manipulation by Contact-Mode Atomic Force Microscopy*. Tribology Letters, **39**: 273–281 DOI: 10.1007/s11249-010-9643-z (cited on page 52)

Dietzel, D., M. Feldmann, U. D. Schwarz, H. Fuchs, and A. Schirmeisen (2013): *Scaling of Structural Lubricity*. submitted to PRL in July 2013, (cited on pages 65, 66, 101–103, 117)

Dobbs, B. J. T. (1975): *The Foundations of Newton's Alchemy*. Cambridge: Cambridge University Press (cited on page 62)

Donohue, J. (1974): *The Structure of the Elements*. New York, NY: Wiley-Interscience (cited on page 62)

Dowson, D. (1997): *History of Tribology*. 2nd Editio Professional Engineering Publishing ISBN: 1-86058-070-X (cited on pages 1, 2, 5, 6)

Evstigneev, M., A. Schirmeisen, L. Jansen, H. Fuchs, and P. Reimann (2008): *Contact ageing in atomic friction.* Journal of Physics: Condensed Matter, **20**:35, 354001 doi: 10.1088/0953-8984/20/35/354001 (cited on pages 21, 80)

Feldmann, M., A. Tekiel, J. Topple, D. Dietzel, P. Grütter, and A. Schirmeisen (2013a): *Contact Ageing in Nanoparticle Stick-Slip Friction.* In preparation, (cited on page 99)

Feldmann, M., D. Dietzel, H. Fuchs, and A. Schirmeisen (2013b): *Influence of Contact Ageing on Nanoparticle Friction Kinetics.* Submitted to PRL, June 2013, 1–5 (cited on page 85)

Feynman, R. P. (1971): *The Feynman Lectures on Physics, Vol. I.* 12–5 (cited on page xi)

Field, J. (2008): *David Tabor. 23 October 1913 – 26 November 2005.* Biographical Memoirs of Fellows of the Royal Society, **54**:October 1913, 425–459 doi: 10.1098/rsbm.2007.0031 (cited on pages 5, 6)

Filippov, A. E., J. Klafter, and M. Urbakh (2004): *Friction through Dynamical Formation and Rupture of Molecular Bonds.* Physical Review Letters, **92**:13, 135503 doi: 10.1103/PhysRevLett.92.135503 (cited on pages 12, 13)

Free Software Foundation, Inc.: *GNU General Public License Version 3* url: http://www.gnu.org/copyleft/gpl.html (visited on 08/05/2013) (cited on page 40)

Giessibl, F. J. (2001): *A direct method to calculate tip–sample forces from frequency shifts in frequency-modulation atomic force microscopy.* Applied Physics Letters, **78**:1, 123 doi: 10.1063/1.1335546 (cited on page 32)

Gitis, N. V. and L. Volpe (1992): *Nature of static friction time dependence.* J. Phys. D: Appl. Phys, **25**: 605–612 doi: 10.1088/0022-3727/25/4/006 (cited on page 78)

Gnecco, E., R. Bennewitz, T. Gyalog, C. Loppacher, M. Bammerlin, E. Meyer, and H. J. Güntherodt (2000): *Velocity Dependence of*

Atomic Friction. Physical Review Letters, **84**:6, 1172–1175 DOI: 10.1103/PhysRevLett.84.1172 (cited on pages 10, 11, 67, 80)

Gnecco, E., R. Bennewitz, T. Gyalog, and E. Meyer (2001): *Friction experiments on the nanometre scale*. Journal of Physics: Condensed Matter, **13**: 619–639 DOI: 10.1088/0953-8984/13/31/202 (cited on page 9)

Gnecco, E., R. Bennewitz, and E. Meyer (2002): *Abrasive Wear on the Atomic Scale*. Physical Review Letters, **88**:21, 215501 DOI: 10.1103/PhysRevLett.88.215501 (cited on page 107)

Gosvami, N. N., T. Filleter, P. Egberts, and R. Bennewitz (2010): *Microscopic Friction Studies on Metal Surfaces*. Tribology Letters, **39**:1, 19–24 DOI: 10.1007/s11249-009-9508-5 (cited on page 114)

Gosvami, N. N., M. Feldmann, J. Peguiron, M. Moseler, A. Schirmeisen, and R. Bennewitz (2011): *Ageing of a microscopic sliding gold contact at low temperatures*. Physical Review Letters, Copyright (2011) by the American Physical Society, **107**:14, 144303 DOI: 10.1103/PhysRevLett.107.144303 (cited on pages 108, 114–117)

Gotsmann, B. and M. a. Lantz (2013): *Quantized thermal transport across contacts of rough surfaces*. Nature materials, **12**:1, 59–65 DOI: 10.1038/nmat3460 (cited on pages 15, 16, 19, 23)

Granick, S. (1991): *Motions and Relaxations of Confined Liquids*. Science, **253**: 1374–1379 DOI: 10.1126/science.253.5026.1374 (cited on page 20)

Greenwood, J. and J. Williamson (1966): *Contact of Nominally Flat Surfaces*. Proceedings of the Royal Society of London A, **295**: 300 (cited on page 15)

He, G, M. H. Müser, and M. Robbins (1999): *Adsorbed layers and the origin of static friction*. Science (New York, N.Y.) **284**:5420, 1650–2 DOI: 10.1126/science.284.5420.1650 (cited on page 17)

Hopcroft, M. A., W. D. Nix, and T. W. Kenny (2010): *What is the Young's Modulus of Silicon?* Journal of Microelectromechanical Systems, **19**:2, 229–238 DOI: 10.1109/JMEMS.2009.2039697 (cited on page 36)

Hunter, J. D. (2007): *Matplotlib: A 2D graphics environment.* Computing In Science & Engineering, **9**:3, 90–95 (cited on page 150)

Israelachvili, J. and D. Tabor (1973): *Shear Properties of Molecular Films.* Wear, **24**:3, 386–390 doi: 10.1016/0043-1648(73)90167-1 (cited on pages 7, 22)

Jagla, E. A. (2010): *Towards a modeling of the time dependence of contact area between solid bodies.* Journal of Statistical Mechanics, **06**: P06006 doi: 10.1088/1742-5468/2010/06/P06006 (cited on pages 19, 21, 85)

Jansen, L. (2009): *Influence of Temperature on the Tribological Properties of Nano-Scale Contacts (Dissertation).* University of Münster (cited on page 12)

Jansen, L., H. Hölscher, H. Fuchs, and A. Schirmeisen (2010): *Temperature Dependence of Atomic-Scale Stick-Slip Friction.* Physical Review Letters, **104**:25, 256101 doi: 10.1103/PhysRevLett.104.256101 (cited on page 67)

JEOL Ltd., Akishima, Japan url: http://www.jeol.co.jp/en/ (visited on 08/05/2013) (cited on page 45)

Johnston, D. C. (2006): *Stretched exponential relaxation arising from a continuous sum of exponential decays.* Physical Review B, **74**:18, 184430 doi: 10.1103/PhysRevB.74.184430 (cited on page 80)

Kaiser, B., T. M. Bernhardt, B. Stegemann, J. Opitz, and K. Rademann (1999a): *Bimodal Distribution in the Fragmentation Behavior of Small Antimony Clusters Sb x + (x=3–12) Scattered from a Highly Oriented Pyrolitic Graphite Surface.* Physical Review Letters, **83**:15, 2918–2921 doi: 10.1103/PhysRevLett.83.2918 (cited on pages 60, 62)

Kaiser, B., T. M. Bernhardt, B. Stegemann, J. Opitz, and K. Rademann (1999b): *Interaction of mass selected antimony clusters with HOPG.* Nuclear Instruments and Methods in Physics Research Section B: **157**:1-4, 155–161 doi: 10.1016/S0168-583X(99)00411-5 (cited on page 62)

Kaiser, B., B. Stegemann, H. Kaukel, and K. Rademann (2002): *Instabilities and pattern formation during the self-organized growth of nanoparticles*

on graphite. Surface Science Letters, **496**: L18–L22 DOI: 10.1016/S0039-6028(01)01491-1 (cited on page 97)

Kaiser, B. and B. Stegemann (2004): *Cluster assembled nanostructures: designing interface properties*. ChemPhysChem, **5**:1, 37–42 DOI: 10.1002/cphc.200300946 (cited on page 62)

Kim, W. K. and M. L. Falk (2009): *Atomic-scale simulations on the sliding of incommensurate surfaces: The breakdown of superlubricity*. Physical Review B, **80**:23, 235428 DOI: 10.1103/PhysRevB.80.235428 (cited on page 17)

Kim, W. K. and M. L. Falk (2011): *Role of intermediate states in low-velocity friction between amorphous surfaces*. Physical Review B, **84**:16, 165422 DOI: 10.1103/PhysRevB.84.165422 (cited on page 79)

Klein, J. (2007): *Frictional Dissipation in Stick-Slip Sliding*. Physical Review Letters, **98**:5, 056101 DOI: 10.1103/PhysRevLett.98.056101 (cited on page 89)

Kumar, V. (1993): *Electronic and atomic structures of SB4 and SB8 clusters*. Physical Review B, **48**:11, 8470–8474 DOI: 10.1103/PhysRevB.48.8470 (cited on page 62)

Langewisch, G., J. Falter, H. Fuchs, and A. Schirmeisen (2013): *Forces During the Controlled Displacement of Organic Molecules*. Physical Review Letters, **110**:3, 036101 DOI: 10.1103/PhysRevLett.110.036101 (cited on page 7)

Lee, S. (2006): *Encyclopedia of chemical processing*. Taylor & Francis, New York, USA ISBN: 0-8247-5563-4 (cited on page 113)

Li, Q., T. E. Tullis, D. Goldsby, and R. W. Carpick (2011): *Frictional ageing from interfacial bonding and the origins of rate and state friction*. Nature, **480**: 233–236 DOI: 10.1038/nature10589 (cited on pages 2, 19, 67, 78, 87, 106, 109, 110, 112, 113)

Liu, Y. and I. Szlufarska (2012): *Chemical Origins of Frictional Aging*. Physical Review Letters, **109**:18, 186102 DOI: 10.1103/PhysRevLett.109.186102 (cited on pages 15, 19, 78, 85, 111)

Lüth, H. (2010): *Solid Surfaces, Interfaces and Thin Films, 5th Ed.* Berlin, Heidelberg: Springer-Verlag ISBN: 978-3-642-13591-0 (cited on pages 44, 45)

Lüthi, R., E. Meyer, H. Haefke, L. Howald, W. Gutmannsbauer, and H.-J. Güntherodt (1994): *Sled-Type Motion on the Nanometer Scale: Determination of Dissipation and Cohesive Energies of C60.* Science, **266**: 1979–1981 DOI: 10.1126/science.266.5193.1979 (cited on page 23)

Maboudian, R. and C. Carraro (2004): *Surface chemistry and tribology of MEMS.* Annual review of physical chemistry, **55**:3, 35–54 DOI: 10.1146/annurev.physchem.55.091602.094445 (cited on page 105)

Marti, O., J. Colchero, and J. Mlynek (1990): *Combined scanning force and friction microscopy of mica.* Nanotechnology, **1**:2, 141–144 DOI: 10.1088/0957-4484/1/2/003 (cited on page 25)

Mate, C. M., G. M. Mcclelland, R. Erlandsson, and S. Chiang (1987): *Atomic-Scale Friction of a Tungsten Tip on a Graphite Surface.* Physical Review Letters, **59**:17, 1942–1946 DOI: 10.1103/PhysRevLett.59.1942 (cited on pages 1, 7, 10, 21, 25, 32)

Mikromasch, NanoAndMore GmbH, Wetzlar, Germany URL: http://www.spmtips.com (visited on 08/05/2013) (cited on pages 37, 69)

Mo, Y., K. T. Turner, and I. Szlufarska (2009): *Friction laws at the nanoscale.* Nature, **457**: 1116–1119 DOI: 10.1038/nature07748 (cited on pages 6, 7, 15, 16, 77)

Mo, Y. and I. Szlufarska (2010): *Roughness picture of friction in dry nanoscale contacts.* Physical Review B, **81**:3, 035405 DOI: 10.1103/PhysRevB.81.035405 (cited on pages 15, 19)

Mortimer, C. (2003): *Chemie.* ed. by C. Mortimer Thieme, Stuttgart, Germany ISBN: 3134843080 (cited on page 62)

Mühlbach, J., P. Pfau, E. Recknagel, and K. Sattler (1981): *Cluster Emission From The Surfaces of Bi, Sb and Se.* Surface Science, **106**: 18–26 DOI: 10.1016/0039-6028(81)90176-X (cited on page 62)

Munz, M. (2010): *Force calibration in lateral force microscopy: a review of the experimental methods.* Journal of Physics D: Applied Physics, **43**:6, 063001 doi: 10.1088/0022-3727/43/6/063001 (cited on page 38)

Müser, M. H., L. Wenning, and M. O. Robbins (2001): *Simple Microscopic Theory of Amontons's Laws for Static Friction.* Physical Review Letters, **86**:7, 1295–1298 doi: 10.1103/PhysRevLett.86.1295 (cited on page 16)

NanoWorld AG, Neuchâtel, Switzerland url: http://www.nanosensors.com/PPP-LFMR.htm (visited on 08/05/2013) (cited on pages 35, 36)

National Instruments Corp., Austin, TX, USA url: http://ni.com (visited on 08/05/2013) (cited on page 46)

Newberry, P. E. and G. W. Fraser (1894): *El-Bersheh I: The Tomb of Tehuti-Hetep.* ed. by F. L. Griffith London: Egypt Exploration Fund (cited on page 5)

Nečas, D. and P. Klapetek (2012): *Gwyddion: an open-source software for SPM data analysis.* Central European Journal of Physics, **10**: (1), 181–188 doi: 10.2478/s11534-011-0096-2 (cited on page 150)

Nonnenmacher, M., J. Greschner, O. Wolter, and R. Kassing (1991): *Scanning force microscopy with micromachined silicon sensors.* J. Vacuum Sci. Technol. B, **9**: 1358–1362 doi: 10.1116/1.585196 (cited on page 35)

Ogletree, D. F., R. W. Carpick, and M. Salmeron (1996): *Calibration of frictional forces in atomic force microscopy.* Review of Scientific Instruments, **67**:9, 3298 doi: 10.1063/1.1147411 (cited on page 37)

Oliphant, T. E. (2007): *Python for Scientific Computing.* Computing in Science & Engineering, **9**:3, 10–20 (cited on page 150)

Omicron NanoTechnology GmbH, Taunusstein, Germany url: http://www.omicron.de/ (visited on 08/05/2013) (cited on pages 41, 44)

Pérez, F. and B. E. Granger (2007): *IPython: a System for Interactive Scientific Computing.* Comput. Sci. Eng. **9**:3, 21–29 (cited on page 150)

Persson, B. N. J. (1993a): *Theory and Simulation of Sliding Friction.* Physical Review Letters, **71**:8, 1212–1215 doi: 10.1103/PhysRevLett.71.1212 (cited on page 20)

Persson, B. N. J. (1993b): *Theory of friction and boundary lubrication.* Physical Review B, **48**:24, 18140–18158 doi: 10.1103/PhysRevB.48.18140 (cited on page 20)

Persson, B. N. J. (1995): *Theory of friction: Stress domains, relaxation, and creep.* Physical Review B, **51**:19, 13568–13585 doi: 10.1103/PhysRevB.51.13568 (cited on pages 12, 20)

Persson, B. N. J. (1998): *Sliding Friction, Physical Principles and Applications.* Berlin, Heidelberg: Springer-Verlag isbn: 3-540-63296-4 (cited on pages 5, 6, 10, 17, 18, 20, 21, 23, 78, 92, 111)

Persson, B. N. J. and S. Gorb (2003): *The effect of surface roughness on the adhesion of elastic plates with application to biological systems.* The Journal of Chemical Physics, **119**:21, 11437 doi: 10.1063/1.1621854 (cited on page 7)

Pollak, E. and P. Talkner (2005): *Reaction rate theory: what it was, where is it today, and where is it going?* Chaos (Woodbury, N.Y.) **15**:2, 26116 doi: 10.1063/1.1858782 (cited on page 11)

Popov, V. L. (2010): *Contact Mechanics and Friction.* Springer, Heidelberg isbn: 978-3-642-10802-0 (cited on pages 15, 16)

Popov, V. L. and J. A. T. Gray (2012): *Prandtl-Tomlinson model : History and applications in friction , plasticity , and nanotechnologies.* Zeitschrift für Angewandte Mathematik und Mechanik, **708**:9, 683–708 doi: 10.1002/zamm.201200097 (cited on page 8)

Prandtl, L. (1928): *Ein Gedankenmodell zur kinetischen Theorie der festen Körper.* Zeitschrift für Angewandte Mathematik und Mechanik, **8**:2, 6–106 (cited on page 8)

Rezvanian, O, M. a. Zikry, C Brown, and J Krim (2007): *Surface roughness, asperity contact and gold RF MEMS switch behavior.* Journal of Mi-

cromechanics and Microengineering, **17**:10, 2006–2015 DOI: 10.1088/0960-1317/17/10/012 (cited on page 105)

Rice, J. R. and A. L. Ruina (1983): *Stability of Steady Frictional Slipping.* Journal of Applied Mechanics, **50**: 343 DOI: 10.1115/1.3167042 (cited on page 18)

Richter, H. and G. Breitling (1953): *Struktur des amorphen Antimons.* Naturwissenschaften, **13**: 361–362 (cited on page 62)

Ritter, C. (2005): *Energiedissipation während der Translation von Antimonnanopartikeln auf Oberflächen: Einfluss der Struktur auf die Reibungseigenschaften (Dissertation).* Humboldt-Universität zu Berlin (cited on page 60)

Ritter, C., M. Heyde, U. D. Schwarz, and K. Rademann (2002): *Controlled Translational Manipulation of Small Latex Spheres by Dynamic Force Microscopy.* Langmuir, **18**:15, 7798–7803 DOI: 10.1021/la011318n (cited on page 58)

Ritter, C., M. Heyde, B. Stegemann, K. Rademann, and U. D. Schwarz (2005): *Contact-area dependence of frictional forces: Moving adsorbed antimony nanoparticles.* Physical Review B, **71**:8, 85405 DOI: 10.1103/PhysRevB.71.085405 (cited on pages 16, 23, 58, 60)

Ritter, C., M. Z. Baykara, B. Stegemann, M. Heyde, K. Rademann, J. Schroers, and U. D. Schwarz (2013): *Nonuniform friction-area dependency for antimony oxide surfaces sliding on graphite.* Physical Review B, **88**:4, 045422 DOI: 10.1103/PhysRevB.88.045422 (cited on page 23)

Rode, S., R. Stark, J. Lübbe, L. Tröger, J. Schütte, K. Umeda, K. Kobayashi, H. Yamada, and A. Kühnle (2011): *Modification of a commercial atomic force microscopy for low-noise, high-resolution frequency-modulation imaging in liquid environment.* The Review of scientific instruments, **82**:7, 073703 DOI: 10.1063/1.3606399 (cited on page 101)

Roth, R., T. Glatzel, P. Steiner, E. Gnecco, A. Baratoff, and E. Meyer (2010): *Multiple Slips in Atomic-Scale Friction: An Indicator for*

the Lateral Contact Damping. Tribology Letters, **39**:1, 63–69 DOI: 10.1007/s11249-009-9567-7 (cited on page 10)

Rovatti, M., G. Paolicelli, A. Vanossi, and S. Valeri (2010): *Sliding onset of nanoclusters: a new AFM-based approach*. Meccanica, **46**:3, 597–607 DOI: 10.1007/s11012-010-9366-0 (cited on pages 23, 58)

Ruina, A. L. (1983): *Slip Instability and State Variable Friction Laws*. Journal of Geophysical Research, **88**:B12, 10359–10370 DOI: 10.1029/JB088iB12p10359 (cited on page 18)

Sang, Y., M. Dubé, and M. Grant (2001): *Thermal Effects on Atomic Friction*. Physical Review Letters, **87**:17, 174301 DOI: 10.1103/PhysRevLett.87.174301 (cited on pages 10, 11, 13, 67, 80)

Sang, Y., M. Dubé, and M. Grant (2008): *Dependence of friction on roughness, velocity, and temperature*. Physical Review E, **77**:3, 036123 DOI: 10.1103/PhysRevE.77.036123 (cited on page 67)

Schirmeisen, A., L. Jansen, and H. Fuchs (2005): *Tip-jump statistics of stick-slip friction*. Physical Review B, **71**:24, 245403 DOI: 10.1103/PhysRevB.71.245403 (cited on pages 37, 95)

Schirmeisen, A., L. Jansen, H. Hölscher, and H. Fuchs (2006): *Temperature dependence of point contact friction on silicon*. Applied Physics Letters, **88**:12, 123108 DOI: 10.1063/1.2187575 (cited on pages 2, 12)

Schirmeisen, A. and U. D. Schwarz (2009): *Measuring the friction of nanoparticles: a new route towards a better understanding of nanoscale friction.* ChemPhysChem, **10**:14, 2373–82 DOI: 10.1002/cphc.200900378 (cited on page 23)

Scholz, C. H. (1998): *Earthquakes and friction laws*. Nature, **391**: 37–42 DOI: 10.1038/34097 (cited on pages 10, 18)

Schwarz, U. D., O. Zworner, P. Koster, and R. Wiesendanger (1997): *Quantitative analysis of the frictional properties of solid materials at low loads. I. Carbon compounds*. Physical Review B, **56**:11, 6987–6996 DOI: 10.1103/PhysRevB.56.6987 (cited on page 22)

Sheehan, P. and C. Lieber (1996): *Nanotribology and Nanofabrication of MoO3 Structures by Atomic Force Microscopy.* Science (New York, N.Y.) **272**:5265, 1158–61 (cited on page 23)

Shinjo, K. and M. Hirano (1993): *Dynamics of friction: superlubric state.* Surface Science, **283**: 473–478 doi: 10.1016/0039-6028(93)91022-H (cited on page 16)

Socoliuc, A., R. Bennewitz, E. Gnecco, and E. Meyer (2004): *Transition from Stick-Slip to Continuous Sliding in Atomic Friction: Entering a New Regime of Ultralow Friction.* Physical Review Letters, **92**:13, 134301 doi: 10.1103/PhysRevLett.92.134301 (cited on page 9)

Stegemann, B. (2003): *Wechselwirkungen monodisperser Antimon-Cluster mit Oberflächen: Diffusion, Wachstum und Strukturbildung im Nanometerbereich (Dissertation).* Shaker Verlag, Aachen isbn: 3-8322-1603-0 (cited on pages 60, 62)

Stegemann, B., C. Ritter, B. Kaiser, and K. Rademann (2004a): *Characterization of the (0001) cleavage surface of antimony single crystals using scanning probe microscopy: Atomic structure, vacancies, cleavage steps, and twinned interlayers.* Physical Review B, **69**:15, 155432 doi: 10.1103/PhysRevB.69.155432 (cited on page 62)

Stegemann, B., C. Ritter, B. Kaiser, and K. Rademann (2004b): *Crystallization of Antimony Nanoparticles : Pattern Formation and Fractal Growth.* Journal of Physical Chemistry B, **108**: 14292–14297 doi: 10.1021/jp049697r (cited on pages 60, 62, 63)

Structure Probe Inc., West Chester, PA, USA url: http://www.2spi.com/catalog/new/hopgsub.php (visited on 08/05/2013) (cited on page 62)

Sul, O., S. Jang, and E.-H. Yang (2009): *Step-edge calibration of torsional sensitivity for lateral force microscopy.* Measurement Science and Technology, **20**:11, 115104 doi: 10.1088/0957-0233/20/11/115104 (cited on page 38)

Szlufarska, I., M. Chandross, and R. W. Carpick (2008): *Recent advances in single-asperity nanotribology.* Journal of Physics D: Applied Physics, **41**: 123001 doi: 10.1088/0022-3727/41/12/123001 (cited on pages 21, 67)

Tekiel, A., J. Topple, Y. Miyahara, and P. Grütter (2012): *Layer-by-layer growth of sodium chloride overlayers on an Fe(001)-p(1x1)O surface.* Nanotechnology, **23**:50, 505602 doi: 10.1088/0957-4484/23/50/505602 (cited on page 46)

Ternes, M., C. P. Lutz, C. F. Hirjibehedin, F. J. Giessibl, and A. J. Heinrich (2008): *The force needed to move an atom on a surface.* Science, **319**:5866, 1066–9 doi: 10.1126/science.1150288 (cited on page 7)

Tomlinson, G. A. (1929): *Molecular Theory of Friction.* A . Phil. Mag. **7**:46, 905–939 (cited on page 8)

Varenberg, M., I. Etsion, and G. Halperin (2003): *An improved wedge calibration method for lateral force in atomic force microscopy.* Review of Scientific Instruments, **74**:7, 3362–3367 doi: 10.1063/1.1584082 (cited on pages 37, 38)

Vlassov, S., B. Polyakov, L. M. Dorogin, A. Lõhmus, A. E. Romanov, I. Kink, E. Gnecco, and R. Lõhmus (2011): *Real-time manipulation of gold nanoparticles inside a scanning electron microscope.* Solid State Communications, **151**:9, 688–692 doi: 10.1016/j.ssc.2011.02.020 (cited on pages 51, 59)

Weiner, D. (2007): *Dynamische Kraftmikroskopie und -spektroskopie an Atomen und Molekülen (Dissertation).* University of Münster (cited on page 41)

Wortman, J. J. and R. A. Evans (1965): *Young's Modulus, Shear Modulus, and Poisson's Ratio in Silicon and Germanium.* Journal of Applied Physics, **36**:1, 153 doi: 10.1063/1.1713863 (cited on page 36)

Yang, Z., H. P. Zhang, and M Marder (2008): *Dynamics of static friction between steel and silicon.* Proceedings of the National Academy of Sciences of the United States of America, **105**:36, 13264–8 doi: 10.1073/pnas.0806174105 (cited on page 18)

Zahl, P., T. Wagner, R. Möller, and A. Klust (2010): *Open source scanning probe microscopy control software package GXSM.* Journal of

Vacuum Science & Technology B, **28**:3, C4E39 DOI: 10.1116/1.3374719 (cited on pages 40, 150)

Publications and Conference Contributions

Articles

- Dietzel, D., **Feldmann, M.**, Fuchs, H., Schwarz, U. D., Schirmeisen, A. (2009),
  Transition from static to kinetic friction of metallic nanoparticles.
  Applied Physics Letters, 95(5), 053104. DOI:10.1063/1.3193551
  Cf. Section 5.1

- Dietzel, D., Mönninghoff, T., Herding, C., **Feldmann, M.**, Fuchs, H., Stegemann, B., Ritter, C., Schwarz, U. D., Schirmeisen, A. (2010),
  Frictional duality of metallic nanoparticles: Influence of particle morphology, orientation, and air exposure.
  Physical Review B, 82, 035401. DOI:10.1103/PhysRevB.82.035401
  Cf. Section 5.4

- Dietzel, D., **Feldmann, M.**, Herding, C., Schwarz, U. D., Schirmeisen, A. (2010),
  Quantifying Pathways and Friction of Nanoparticles During Controlled Manipulation by Contact-Mode Atomic Force Microscopy.
  Tribology Letters, 39, 273–281. DOI:10.1007/s11249-010-9643-z
  Cf. Sections 4.2 and 4.3

- Gosvami, N. N., **Feldmann, M.**, Peguiron, J., Moseler, M., Schirmeisen, A., Bennewitz, R. (2011),
  Ageing of a Microscopic Sliding Gold Contact at Low Temperatures.
  Physical Review Letters, 107(14), 144303. DOI:10.1103/PhysRevLett.107.144303
  Cf. Section 6.2

- **Feldmann, M.**, Dietzel, D., Fuchs, H., Schirmeisen, A. (2013),
  Influence of Contact Ageing on Nanoparticle Friction Kinetics.

submitted to Physical Review Letters, June 2013.
Cf. Section 5.2

- Dietzel, D., **Feldmann, M.**, Schwarz, U. D., Fuchs, H., Schirmeisen, A. (2013),
Scaling of Structural Lubricity.
submitted to Physical Review Letters, July 2013.
Cf. Section 5.4

- **Feldmann, M.**, Tekiel, A., Topple, J., Dietzel, D., Grütter, P., Schirmeisen, A. (2013),
Contact Ageing in Nanoparticle Stick-Slip Friction
In preparation.
Cf. Section 5.3

Conference Contributions/Presentations

- DPG Frühjahrstagung (2009),
Feldmann, M., Dietzel, D., Schirmeisen, A.,
Controlled nanoparticle manipulation along defined vector pathways,
Sektion Kondensierte Materie, Dresden, Germany (poster)

- Joint ICTP/FANAS Conference on Trends in Nanotribology (2009),
Feldmann, M., Dietzel, D., Fuchs, H., Schwarz, U. D., Schirmeisen, A.,
Transition from Static to Kinetic Friction of Nanoparticles,
Triest, Italy, awarded with 'ICTP/FANAS Young Researcher Award' (poster)

- American Physical Society March Meeting (2010),
Feldmann, M., Dietzel, D., Mönninghoff, T., Schwarz, U. D., Schirmeisen, A.,
Scaling Laws in Superlubric Sliding of Metallic Nanoparticles,
Portland, Oregon, USA (oral)

- DPG Frühjahrstagung (2010),
Feldmann, M., Dietzel, D., Schirmeisen, A.,
Velocity Dependence of the Kinetic Friction of Nanoparticles,
Sektion Kondensierte Materie, Regensburg, Germany (poster)

- 1st European Nanomanipulation Workshop (2010),
Feldmann, M., Dietzel, D., Schirmeisen, A.,

Instrumentation for highly controlled nanoparticle manipulation and its application towards nanotribology, Cascais, Portugal (poster)

- ESF-FANAS Meeting (2010),
  Feldmann, M., Dietzel, D., Schirmeisen, A.,
  Dependence of the Kinetic Friction of Nanoparticles on Translation Velocity, Saarbrücken, Germany (poster)

- ECOSS27 (2010),
  Feldmann, M., Dietzel, D., Mönninghoff, T., Schirmeisen, A.,
  Scaling Laws in Superlubric Sliding of Metallic Nanoparticles,
  Groningen, Netherlands (oral)

- DPG Frühjahrstagung (2011),
  Feldmann, M., Dietzel, D., Schwarz, U. D., Schirmeisen, A.,
  Transition from Static to Kinetic Friction of Nanoparticles,
  Sektion Kondensierte Materie, Dresden, Germany (poster)

- International Tribology Forum, Hoi An Discussions (2011),
  Feldmann, M., Dietzel, D., Schirmeisen, A.,
  Nanoparticle friction: The influence of contact area, velocity and temperature, Hoi An, Vietnam (poster)

- 2nd European Nanomanipulation Workshop (2011),
  Feldmann, M., Dietzel, D., Schirmeisen, A.,
  Nanoparticle Manipulation Using the 'Tip-on-Top' AFM Technique and its Benefits for Nanotribological Investigations, Tartu, Estonia (poster)

- DPG Frühjahrstagung (2012),
  Feldmann, M., Tekiel, A., Topple, J., Dietzel, D., Grütter, P., Schirmeisen, A.,
  Nanoparticle Manipulation With Combined AFM/SEM,
  Sektion Kondensierte Materie, Berlin, Germany (poster)

- Advanced Atomic Force Microscopy Techniques (2012),
  Feldmann, M., Tekiel, A., Topple, J., Dietzel, D., Grütter, P., Schirmeisen, A.,
  Nanoparticle Manipulation With Combined AFM/SEM,
  Karlsruhe, Germany (poster)

- DPG Frühjahrstagung (2013),
  Feldmann, M., Dietzel, D., Schirmeisen, A.,
  The Interdependence of Timescale and Temperature for Nanoparticle Friction, Sektion Kondensierte Materie, Regensburg, Germany (oral)

- 4th European Nanomanipulation Workshop (2013),
  Feldmann, M., Dietzel, D., Schirmeisen, A.,
  The Interdependence of Timescale and Temperature for Nanoparticle Friction, Krakow, Poland (oral)

Acknowledgements

I have received invaluable support while conducting my studies and during the finalization of this manuscript from academic advisors, coworkers, friends, and my family. I owe special thanks to:

· Prof. Dr. André Schirmeisen, my supervisor, without whom this work could not have been realized. His continued interest in nanotribological issues and his enthusiasm were highly contagious and motivating factors. I have benefited substantially from his experience in the field of scanning probe microscopy, and not least he provided access to the financial foundation for my studies,

· Prof. Dr. Michael Dürr, for kindly agreeing to act as additional reviewer of this thesis, as well as Prof. Dr. Christian Heiliger and Prof. Dr. Peter J. Klar for participating in the assessment commission for this work,

· Prof. Dr. Harald Fuchs, for allowing me to use his laboratory facilities in Münster, and for providing an inspiring work environment at CeNTech,

· Prof. Dr. Peter Grütter, for giving me the opportunity to work at his lab in Montreal, Canada over the course of three months,

· Dr. Dirk Dietzel, for truly invaluable support and insight into a broad range of topics, and for reviewing parts of this manuscript. Don't fume, just wonder . . . ,

· Dr. Jens Falter, for his attention to the common thread, and for his continued and inexhaustible support, be it in the lab or as my housemate, and in particular during the final stages of the preparation of this thesis,

· Johannes Sondhauß, for strenuous support in the lab and the office, as well as extra-curricular distractions on the road bike,

· Dr. Gernot Langewisch, for his profound professional input and his eye for detail,

· Dr. Lars Jansen, for introducing me to the quirks of the VT-AFM system,

· Felix Mertens, for insightful discussions, and for the excellent working conditions at our office,

· Gosvami Nitya Nand, PhD, for a very fruitful collaboration,

· Dr. Thomas Göddenhenrich, for insightful discussions and general support,

· Arne Scheffer, for clearing quite a few obstacles in order to employ me during significant periods of my studies,

· Antoni Tekiel and Jessica Topple, for sharing 'their' AFM system in Montreal with me, and for their tireless support during my stay in Montreal,

· Vincent Poitras, for being a great housemate and for sharing with me a Québécois' perspective,

· Alexandra Gabriel, for always kindly taking the time to quickly resolve any kind of administrative issue,

· Bernd Schmidt, for reviewing a section of this manuscript,

· Sören Zint, for well-received advice and general support,

· many current and former members of the Schirmeisen group at JLU Giessen and of the Fuchs group at WWU Münster and other coworkers for kind cooperation and support: Marvin Stiefermann, Alexander Weiß, Oscar Diaz Arado, Kathrin Hardes, Dr. Harry Mönig, Dr. Daniel Braun, Dr. Ulrich Fischer, and Reinhold Arends,

· the authors of the following free and open source software packages, which were incorporated into the workflow of performing the experiments, evaluating the data, and producing this manuscript:
  · GXSM: used for SPM scan control (Zahl et al., 2010),
  · Python, NumPy, matplotlib, Pandas, IPython: employed for data evaluation, and as a programming framework for the implementation of the Monte Carlo simulations (Oliphant, 2007; Hunter, 2007; Pérez et al., 2007),
  · vim: an indispensable text editor,
  · Gwyddion: 2D/3D SPM scan data evaluation (Nečas et al., 2012),
  · Gimp, Inkscape: used for images and illustrations,
  · Linux kernel, Ubuntu OS: my operating system of choice,
  · LaTeX, pdfTex, KOMA-Script: used for typesetting of this manuscript,

· all of my friends, who relentlessly supported me while I was working on this thesis, even during those periods in which it consumed most of my time, especially Caro, Stelle, Chris, Dom, Jan, Anna, Claudia, Katrin, and Marisa,

· last not least my parents, my brother, and my grandmother, Maria, Klemens, Thomas, and Klara. Without their support and inspiration I would probably have neither started nor finished this work.

I hereby thank all of you most heartily!

Erklärung

Ich erkläre: Ich habe die vorgelegte Dissertation selbständig und ohne unerlaubte fremde Hilfe und nur mit den Hilfen angefertigt, die ich in der Dissertation angegeben habe. Alle Textstellen, die wörtlich oder sinngemäß aus veröffentlichten Schriften entnommen sind, und alle Angaben, die auf mündlichen Auskünften beruhen, sind als solche kenntlich gemacht. Bei den von mir durchgeführten und in der Dissertation erwähnten Untersuchungen habe ich die Grundsätze guter wissenschaftlicher Praxis, wie sie in der 'Satzung der Justus-Liebig-Universität Gießen zur Sicherung guter wissenschaftlicher Praxis' niedergelegt sind, eingehalten.

Gießen,

(Michael Feldmann)